DEPARTEMENT OF CHEMISTRY

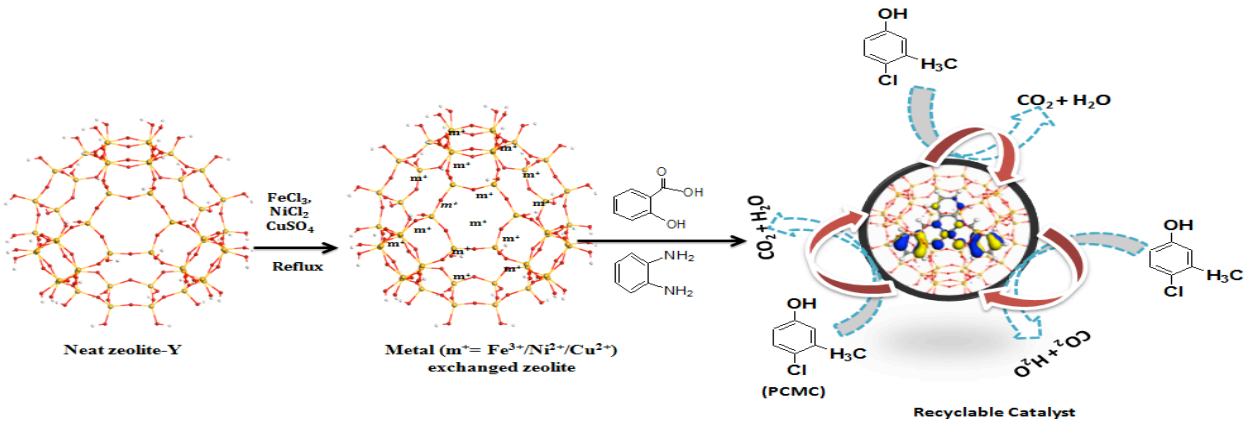

Synthesis and Characterization of Zeolite Y Encapsulated Metal Complexes and Surfactant Modified Zeolite Y for Removal of Pollutants

Solomon Legese Hailu

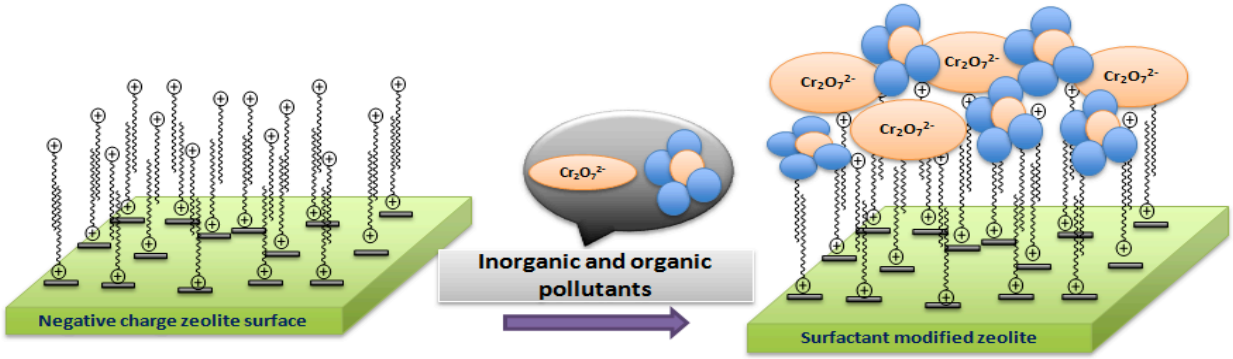

May 2016

Synthesis and Characterization of Zeolite Y Encapsulated Metal Complexes and Surfactant Modified Zeolite Y for Removal of Pollutants

Solomon Legese Hailu

A Thesis Submitted to

Department of Chemistry

Presented in Fulfilment of the Requirements for the Degree of Doctor of Philosophy (Analytical Chemistry)

Addis Ababa University

Addis Ababa, Ethiopia

May 2016

Addis Ababa University

Chemistry Department

This is to certify that the thesis prepared by Solomon Legese Hailu entitled: *Synthesis and Characterization of Zeolite Y Encapsulated Metal Complexes and Surfactant Modified Zeolite Y for Removal of Pollutants* and submitted in partial fulfilment of the requirements for the Degree of Doctor of Philosophy (Analytical Chemistry) complies with the regulations of the University and meets the accepted standards with respect to originality and quality.

Signed by the Examining Committee

Name	Signature	Date
Prof. Robert Ian McCrindle External Examiner	……	……
Dr. Negussie Megersa Examiner	……	……
Dr. Samuel Melaku Examiner	……	……
Dr. Merid Tessema Advisor	……	……
Dr. Balachandran Unni Nair Advisor	……	……
Dr. Mesfin Redi Advisor	……	……
Prof. Isabel Diaz Advisor	……	……

Acknowledgements

This dissertation is the end of my journey with the completion of my Ph.D in Chemistry. This long and tedious journey may not have been possible without the support and encouragement of numerous people including my well-wishers, friends, colleagues and various institutions.

At this moment of accomplishment, first of all I pay homage and express my deep sense of gratitude to my advisors **Dr. Merid Tessema, Dr. Balachandran Unni Nair, Dr. Mesfin Redi and Prof. Isabel Diaz**. I am fortunate to have four different supervisors in different field of chemistry has treated me as their friend. **Dr. Merid Tessema**, I appreciate your encouragement and continuous guidance and meticulous editing of my thesis; **Dr. Balachandran Unni Nair**, I was fortunate to meet a man who always taught me that I have to work step by step to make my dreams come true. Dear Dr, Thank you for everything you gave me and I really appreciate your support. It was really precious and a milestone for my future academic and research carrier. **Dr. Mesfin Redi**, I thank you for your critical comments on manuscripts and constructive criticism throughout my studies. Dear Dr. it is a privilege for me to enjoy your tremendous academic support and inspirations and it made me have a Ph.D with treasured knowledge's. **Prof. Isabel Diaz**, I owe you for introducing me to zeolite chemistry and your encouragement, constructive and valuable comments and suggestions in my research work and on manuscripts writing. My sincere thanks go to **Dr. Ahmed Mustefa**, the chairman of the Department, for providing me with an opportunity to register in the Chemistry department. I also appreciate members of the **Analytical stream**, for their critical evaluation and

constructive comments during seminar and course work. I have also been privileged to receive different kinds of assistance from the staff members of the **Department of Chemistry, AAU**.

I am highly indebted to the **Leather Industry Development Institute (LIDI)** for allowing me to join the PhD program with sponsorship, covering my travel and living expenses during my two years in Chennai, India. I would like to acknowledge the technical support from the **Central Leather Research Institute (CLRI)**, India. In particular, I would like to thank the Chemical Laboratory Scientists (**Dr. Raghava Rao, Dr. Aravindhan, Dr. Subramanian, Dr. Sreeram, Dr. Nishad, Dr. Easwaramoorthi, Dr. Aruna, Dr. Vaidyanathan, Dr. Chandrasekaran, and Dr. Madhan**), PhD students and staff member (**Shanti Aka**) of the laboratory for ordering laboratory supplies and helping me handle analytical instruments. My deeply appreciations are extended to all members of the CLRI with whom I enjoyed a fantastic social and scientific life in Chennai.

I would like to express my gratitude to my friend, **Amsalu Efrem** for your moral and spiritual support and also for the instantaneous supply of necessary journal articles. My grateful appreciation is also extended to all my friends, Ph.D and MSc students for your valuable support. Finally, I would like to thank my family for their spiritual support and their patience that has always been the best encouragement for me.

Above all, I praise and thank almighty God for His showers of blessings that gave me courage and strength throughout my research to successfully complete my studies.

Abstract

Synthesis and Characterization of Zeolite Y Encapsulated Metal Complexes and Surfactant Modified Zeolite Y for Removal of Pollutants

Solomon Legese Hailu

Addis Ababa University

May 2016

In this study heterogeneous catalysts were synthesized based on the encapsulation of iron(III), nickel(II) and copper(II) with complexes of N,N′-ethylenebis(salicylimine), mixed ligands of 2,2'-bipyridine and 1,10-phenanthroline and N,N′-disalicylidene-1,2-phenylenediamine ligands into zeolite Y supercage using ship-in-a-bottle method of synthesis. The catalysts were characterized by X-ray powder diffraction, BET surface area and pore volumes, Fourier transform infrared spectroscopy, electron paramagnetic resonance, thermo-gravimetric and elemental analysis. Computational studies based on Density functional theory (DFT) calculation are carried out on both neat complexes as well as metal complexes encapsulated into zeolite Y to investigate changes in structural parameters like bond length, bond angle and dihedral angle, energies of the highest occupied molecular orbital (HOMO) and lowest unoccupied molecular orbital (LUMO), global hardness and softness value of the metal complexes upon encapsulation into zeolite.

The results obtained from the physico-chemical analytical techniques showed that iron(III), nickel(II) and copper(II) complexes of N,N′-ethylenebis(salicylimine), mixed

ligand of 2,2'-bipyridine and 1,10-phenanthroline and N,N′-disalicylidene-1,2-phenylenediamine ligands were successfully formed into zeolite Y supercage without affecting zeolite structure and properties of the metal complexes. Moreover, Density functional theory (DFT) calculations predicted that zeolite encapsulated metal complexes has higher reactivity compared to respective metal complexes.

The catalysts prepared were found to be very effective in the removal of organic pollutants (i.e. azo dye, 2-phenyl phenol (OPP) and 4-chloro-3-methyl phenol (PCMC)) from synthetic wastewater. Interactive effects of four factors; initial hydrogen peroxide (H_2O_2) concentration, catalyst dosage, temperature and pH on the degradation of selected organic pollutants were determined. Experimental results showed that lower pH and higher temperature were optimal for complete removal of organic pollutants using the prepared catalysts. Moreover, increase in the concentration of hydrogen peroxide (H_2O_2) and catalyst dosage, beyond the optimum concentration had a negative effect attributed to the formation of hydroperoxyl radical (•OOH). This has a lower oxidation potential than the hydroxyl radical (•OH) and aggregation of catalysts, respectively. The extent of reusability for the catalytic oxidation of organic pollutants and the possible deactivation mechanism after successive reuse of each catalyst were studied. The possible intermediate product, degradation pathway and kinetic studies for oxidation of organic pollutants were also studied.

Besides ion exchange zeolite have adsorption properties due to its large surface area and net negative charge. In this study the negative charge and hydrophilic surface properties of neat zeolite were modified by haxadecyltrimethyl ammonium bromide (HDTMA-Br)

surfactant to adsorb both inorganic and organic pollutants simultaneously. The surfactant modification effect on the surface of zeolite was characterized using X-ray powder diffraction, FT-IR spectroscopy, scanning electron microscopy, BET surface area and pore volume, thermo gravimetric analysis, zeta potential and hydrophobicity measurements. The results of physico-chemical analytical techniques showed that a bilayer of surfactant-modified zeolite was successfully formed on the external surface of the zeolite. The surfactant-modified zeolite was investigated for the adsorption of acid blue dye and Cr(VI) in synthetic wastewater. The effects of adsorbent dosage, pH, temperature, time and initial pollutant concentrations were investigated in batch adsorption experiments. The correlation coefficient and the normalized standard deviation value showed that the experimental isotherm data fitted well to Langmuir and Freundlich isotherm models for acid blue dye and Cr(VI), respectively. The kinetic process is well described by pseudo second order kinetic model. The prepared catalyst and the surfactant modified zeolite showed good catalytic and adsorption capacities for removal of organic and inorganic pollutants from real tannery wastewater.

Table of Contents

List of Figures

List of Tables

Abbreviations

PBU	Primary Building Unit
SBU	Secondary Building Unit
D4R	Double Four Ring
D6R	Double Six Ring
DFT	Density Functional Theory
AOP	Advanced Oxidation Process
EOP	Electrochemical Oxidation Potential
SMZ	Surfactant Modified Zeolites
TMAB	Tetramethyl ammonium bromide
TEAB	Tetraethyl ammonium bromide
HDTMAB	Hexadecyltri methyl ammonium bromide
ODTMAB	Octadecyltri methyl ammonium bromide
BTMAC	Benzyltri methyl ammonium chloride
BDTDAC	Benzyltetradecyl dimethyl ammonium chloride
SDBAC	Stearyldimethyl benzyl ammonium chloride
CMC	Critical Micelle Concentration
ECEC	External Cation Exchange Capacity
DMPO	5,5'-dimethyl-1-pyrroline-N-oxide
DMSO	Dimethyl sulfoxide-d_6
PCMC	Para chloro meta cresol
OPP	Ortho phenyl phenol

CSMZ	Cationic Surfactant Modified Zeolite
NMR	Nuclear Magnetic Resonance
FTIR	Fourier Transform Infrared Spectrophotometer
AAS	Atomic Absorption Spectroscopy
ICP	Inductive Coupled Plasma
TGA	Thermo Gravimetric Analysis
DTG	Derivative Thermogravimetry
XRD	X-ray Diffraction
BET	Brunauer, Emmett and Teller
NLDFT	Non Local Density Functional Theory
DA	Dubinin-Astakhov
HK	Horvath-Kawazoe
HR-SEM	High Resolution Scanning Electron Microscope
EPR	Electron Paramagnetic Resonance
ESR	Electron Spin Resonance
HPLC	High Performance Liquid Chromatography
DAD	Photodiode Array Detector
DPC	DiPhenylCarbazide
GGA	Generalized Gradient Approximation
PBE	Perdew-Burke-Ernzerhof
DN	Double Numeric
TOC	Total Organic Carbon
COD	Chemical Oxygen Demand

HOMO	Highest Occupied Molecular Orbital
LUMO	Lowest Unoccupied Molecular Orbital
MHP	Maximum Hardness Principle
MPP	Minimum Polarizability Principle
IUPAC	International Union of Pure and Applied Chemistry
TCEC	Total Cation Exchange Capacity
NSD	Normalized Standard Deviation
CETP	Common Effluent Treatment Plant

1. Introduction

1.1. Background

Catalysts date back to the dawn of civilization when mankind began to produce alcohol by fermentation. However, a Swedish chemist, Jöns Jacob Berzelius, was the first scholar who systematically investigated, with recorded observations, catalysts in 1835 [1]. He reviewed a number of earlier findings on chemical change in both homogeneous and heterogeneous systems, and showed that these findings could be rationally co-ordinated by the introduction of the concept of catalysis. He proposed the existence of a new force, which he called the "catalytic force" and then called this force "catalysis" for the decomposition of materials by this force in his experiment. This is probably the first recognition of catalysis as a wide range of natural phenomenona [2].

In modern times catalysis is an area of prime importance in the forefront of chemistry. The term 'catalysis' refers to the enhancement of a particular chemical reaction by the appropriate use of a suitable material. Catalysis can enhance the rate of a thermodynamically feasible reaction but can't change the position of the thermodynamic equilibrium. Most catalysts are solids or liquids, but they may also be gases. The basic essential characteristics of a catalyst are high activity, good selectivity and stability (regenerability). Activity is a measure of how fast one or more reactions proceed in the presence of the catalyst. The selectivity is related to the fraction of the starting material that is converted to the desired product and stability shows the lifetime or deactivation of the catalyst. Currently, all product-manufacturing industries use

a catalyst for rate enhancement and material saving purposes in various steps of their production.

The growing demands for the design of environmentally friendly products and processes have led to the development of environmentally friendly catalytic system with green chemistry concepts. Furthermore, in view of the growing concern over environmental pollution and with further advance of catalytic sciences, chemical industries are forced to adopt new safe and eco-friendly technologies with less consumption of energy and raw materials. Currently, chemical reactions involving catalysis are more preferred as they are highly effective under milder conditions and generate minimum wastes. Thus there is a constant need to develop regenerable and effective solid catalysts. In accordance with growing industrial activities and the demand for more efficient, selective and cheaper processes, the use of homogeneous transition metal complexes to catalyse organic reactions have received widespread attention in recent years. One of the positive aspects of homogeneous catalysts is that they have well defined reactive centres, which lead to high and reproducible selectivity and operation at low temperatures and pressures.

However, homogeneous catalysts have limited applications due to the fact that they are active only in limited pH range (pH 2-4), they produce metal ion containing waste sludge, which is difficult to dispose. The catalysts are deactivation by some iron complexing agents like phosphates ions and are difficult to separate the product mixture. The low thermal and chemical stability of such systems result in their slow decomposition [3, 4]. The disadvantages associated with homogeneous catalyst have put greater emphasis on the development of new and improved heterogeneous catalytic systems. The most widely

used technique to heterogenize complexes is to encapsulate them into inorganic or organic supporting materials.

Heterogeneous catalyst could be applied in various wastewater treatment processes to overcome the environmental pollutions caused by industrial activities. One of the industrial activities, which drastically cause environmental pollution, is the leather processing industry. Leather industries are major consumers of water and consequently one of the largest groups of industries causing intense water pollution. The extensive use of chemical and water results in generation of large quantities of highly polluted wastewater containing different organic and inorganic hazardous wastes [5].

Hence the leather industry has been categorized as one of the highly polluting industries and the leather making activity can have adverse impact on the environment [5, 6]. The tannery effluents are characterized by high contents of dissolved, suspended organic and inorganic solids giving rise to high oxygen demand and potentially toxic metal salts and chromium ion [5, 6]. The disagreeable odor emanating from the decomposition of proteinous waste material and the presence of sulphide, ammonia and other volatile organic compounds are also associated with tanning activities [7]. Moreover, due to lack of modern and effective treatment methods in the tanning industries the waste generated from the tanning process has an immense impact to the surrounding environment.

Therefore, the motivations behind this research work were the low efficiency of conventional water treatment methods in removing non-biodegradable chemical pollutants from the tanning industry; a new approach to improve immobilization catalyst active moieties inside zeolite cages, namely encapsulation. Although several fragment

reports on encapsulation of metal complex inside the zeolite cage, little or no reports are available on the systematic synthesis and characterization of different metal complex and ligand combination. Neither are they available on comparative investigations of the efficiency of catalysts to remove chemical pollutant found in the tanning industry or the systematic study on the reusability of catalysts and the mechanism of catalyst deactivation. Moreover, there is no literature on studies of adsorption capacity of surfactant-modified zeolite for removal of tannery effluents (both cationic and anionic pollutants) from the same modified surface.

1.2. Objective of the Study

1.2.1. General Objective

The general objective of this research work was to investigate the use of zeolite based heterogeneous catalysis and surface modified zeolite for the efficient and environmentally friendly treatment of chemical pollutants

1.2.2. Specific Objectives

The specific objectives of this research work were:

- Synthesis of Schiff base ligands from ethylenediamine and salicylaldehyde as well as salicylaldehyde and *o*-phenylenediamine and their iron(III), nickel(II) and copper(II) complexes.

- Synthesis of mixed ligand complexes of iron(III), nickel(II) and copper(II) with 2,2-bipyridine and1,10- phenanthroline and surfactant modified zeolites.

- Characterize the neat zeolite, Schiff base ligands, metal complexes, metal exchanged zeolites, zeolite encapsulated metal complexes and surfactant modified zeolite using different physico-chemical methods.

- Characterize the neat metal complexes and zeolite encapsulated metal complexes using quantum chemical calculation based on density functional theory (DFT) computational methods.

- Optimize the concentration of H_2O_2, catalyst dosage, amount of adsorbent, temperature, pH and pollutant concentration in the application of synthesized catalyst and surfactant-modified zeolite for oxidation and adsorption of pollutants.

- Determine the catalytic efficiency and adsorption capacity of synthesized catalyst and surfactant-modified zeolite for tannery effluents.

2. Literature Review

Catalysts fall into two categories depending on their relationship to the phase of the reaction in which they are involved i.e.homogeneous and heterogeneous. A homogeneous catalyst is in the same phase as the components of the reaction that it is catalysing and a heterogeneous catalyst is in a different phase to the components of the reaction for which it is acting. Metal complexes and organometallic compounds are examples of homogeneous catalysts. These catalysts are soluble in the reaction medium and are used in the production of different chemicals. In contrast to homogeneous catalysts, heterogeneous catalysts are usually solid species attached to a solid surface. They are mainly used for large-scale industrial activities.

Both homogeneous and heterogeneous catalysts have been extensively used in industrial activity since the beginning of the twentieth century. But, heterogeneous catalysis has grown at a faster rate than homogeneous catalysis for industrial applications. The main problem in the use of homogeneous systems is the separation of catalysts from reactants and products, which very easy to achieve practically in the case of heterogeneous catalysts. The deactivation of homogeneous catalysts by the self-aggregation of the active sites may also restrict its application in industrial processes, whereas heterogeneous catalysts are relatively more stable. The above mentioned facts maybe the reason for the fast growth of heterogeneous catalyst system for industrial applications.

Homogeneous transition metal catalysed reactions are important in all aspects of chemical reactivity. Wacker (1959) was a pioneer of homogeneous catalyst by using transition metal complexes. The Wacker process was focused on the oxidative conversion

of ethylene to acetaldehyde with palladium(II) catalysed oxidation [8, 9]. The commercial success of the Wacker process provided an immense stimulus for further studies of palladium and other transitional metal complexes as homogeneous catalysts.

All catalytically supported chemical reactions using transition metal complexes are associated with changes in the oxidation state and coordination environment of the central transition metal ion and ligand field environment. The coordination environment around the central metal ion is responsible for the effectiveness of the catalyst. Unlike other metal ions, transition metal ions possess nine orbitals in total that include one s, three p and five d orbitals and there are cases where all the nine orbital's participate in bond formation with ligands. The existence of central transition metal ions in different oxidation states were found to be most promising in catalytic studies and the transition metal ion compounds, by virtue of their readily available multi oxidation states, occupy a key position in the development of most efficient catalysts [10]. Among the transition metal ions, iron(III), nickel(II) and copper(II) are the widely used as catalysts in various fields. The reasons for selecting the above transition metal ions are; they were successfully encaged within the zeolite framework by carefully synthesizing the metal ion exchanged zeolites and metal complexes under optimized conditions and also they are cheap, non-toxic and readily available. They are also well known transition metal ions that undergo Fenton like reaction and have been used successfully for treating various organic pollutants. Additionally, these metal ions have greater stability, better catalytic activity and recyclability in certain reactions [11-15].

Homogeneous catalysts have limited applications due to their high susceptibility to reaction conditions and the difficulty of separating them from the product mixture. The low thermal and chemical stabilities of such systems result in decrease of their catalytic activity. All the problems encountered by homogeneous catalysts can be overcome by immobilizing them on a suitable matrix. The immobilization or encapsulation of homogeneous catalysts leads to higher thermal and chemical stabilities. Product selectivity and substrate specificity is increased to a greater extent by steric crowding around the metal ion. In addition to all these qualities, the ease of separation of the supported catalysts makes them more beneficial when compared to their homogeneous counterparts.

Recent years have witnessed a great deal of interest in the study of heterogeneous catalytic systems due to their importance as catalysts for many reactions. Heterogenization of homogeneous catalysts possesses the advantages of both homogeneous and heterogeneous systems. The term heterogenization refers to the process of immobilization of homogeneous transition metal complexes by anchoring them to an inert polymer or inorganic supports. Some of supporting materials are synthetic and natural zeolites, nafion film or nafion pallet, polyethylene copolymers, silica fabrics and clays [16-19]. However, nafion has a limitation associated with high cost of the perfluorosulphonic polymer [4, 20]. Silica fabrics have a greater iron leaching effect due to instability of the silica-Fe structure [20] and it is expensive, since polyethylene copolymer is a synthetic polymer of ethylene it can be oxidized by the hydroxyl radicals. In addition, it is not an environmentally friendly solid material for supporting metal complexes [21]. Though clay is cheap and abundant it is not be a good

supporting micro porous material owing to the following limitations; low cation exchange capacity, encapsulation of metal ion using cationic exchange of the exchangeable cations of the clay may lead to low content of metal ion, lack of permanent high porosity and it has a layered crystalline structure. It is also subject to shrinking and swelling as water is absorbed and removed between the layers [19, 22-24].

Several materials that can be employed for supporting homogeneous catalysts include silica, alumina, zeolites, clay etc. Interest in inorganic supports has arisen because of their unique characteristics of flexibility and stability. Among the above inorganic and organic hosting materials, zeolites are attractive micro porous supporting materials for the encapsulation of transition metal complexes or organometallics within their voids because it is cheap, naturally abundant and it has unique properties. These include ion exchange abilities and have a rigid and three-dimensional crystalline structure consisting of a network of interconnected tunnels and cages [25-27]. In addition, the stability of metal complexes in actual reaction conditions is expected to be improved by encapsulating into a zeolite supercage. This effect may be explained in terms of the following aspects: (a) the complexes are immobilized inside the cage, (b) dimerization processes of the complexes are retarded resulting in longer life time and (c) zeolite imparts additional stability to the complex by acting as ligands [28, 29]. Besides, the unique structure of the zeolite cage, the steric and electrostatic constraints imposed by the walls of the zeolite framework can influence the geometry of the metal complex and hence change magnetic, electronic and redox properties of the encapsulated metal complex and this can lead to changes in the reactivity of encapsulated transition metal complex [30-33]. The cations in zeolite cage also play an important role in affecting the

fate of transition metal complex in the cage, other than merely compensating the negative charge in zeolite framework [34]. Moreover, it is possible to replace Na^+ of the zeolite-NaY with other transition metal cations and offer different reactive sites for the interaction of the incoming guest molecules. Once the cations in the zeolite cage are exchanged with transition metal complexes the physico-chemical characteristics such as electrostatic potential and electric field within the cage, spin-orbit parameter and space available for guest molecules inside the supercage are known to be controlled by these exchangeable charge compensating alkali metal cations. The bond formed between the ligand with previously exchanged metal ions in the solid surface stabilizes the complex and generates catalytically active centres. The supported complexes possess higher selectivity and greater catalytic activity than their homogeneous analogues [35-38].

2.1. Zeolites

More than 200 years ago a Swedish geologist Axel Fredrik Cronstedt (1722-1765) discovered a new mineral species (stilbite) in rocks that were used as building stone [39]. This new species, a crystalline aluminosilicate, was called zeolite owing to the behaviour of this mineral upon heating. In 1756 he published the article "Observation and description of an unknown species of rock, called ZEOLITES", in a Swedish magazine where he explained that this mineral visibly lost water when heated by a flame. Cronstedt gave these minerals an aptly descriptive name "zeolite" [40]. The term that etymologically comes from classic Greek ζεω (zeo), which means to boil, and λιθοζ (lithos) that means stone. Therefore, these materials are literarily called "boiling stones" From that time it took almost one century before Damour established the reversible dehydration-hydration character of zeolites in 1840 [41]. This phenomenon has led to one

of the most important uses of zeolites both in industrial application and laboratory research, namely as a drying agent for liquids and gases. Another property of zeolite is its ion exchange ability in which the negative charge of the zeolite lattice is neutralized by other species. This ion exchange feature has created opportunities for expanding the use of zeolite to a wide area of applications. Barrer and his co-worker have performed much of the pioneering work regarding the adsorption properties of zeolites and this study was a milestone for the applicability of zeolites in wider fields [42].

Zeolites can be found in a variety of natural geological environments containing siliceous materials (volcanic rocks, clays, feldspar, biogenic silica and other silica rocks). These natural zeolites have a volcanic origin and are formed when flowing water of high pH and salt content interact with volcanic ash, causing rapid crystal formation [43].

2.1.1. Structure of Zeolites

Zeolites are natural and synthetic crystalline, micro porous, aluminosilicate materials with well-defined structures and unique characteristics [25, 26, 44]. It is a crystalline mineral formed by tetrahedral units of $[SiO_4]^{4-}$ and $[AlO_4]^{5-}$, which are connected by sharing their oxygen atoms. These units allow a large number of possible structures, which, in the case of aluminosilicate compounds, produce various crystalline frameworks with interesting properties. The arrangements of these tetrahedral units produce molecular sized pores in a variety of dimensions and geometries.

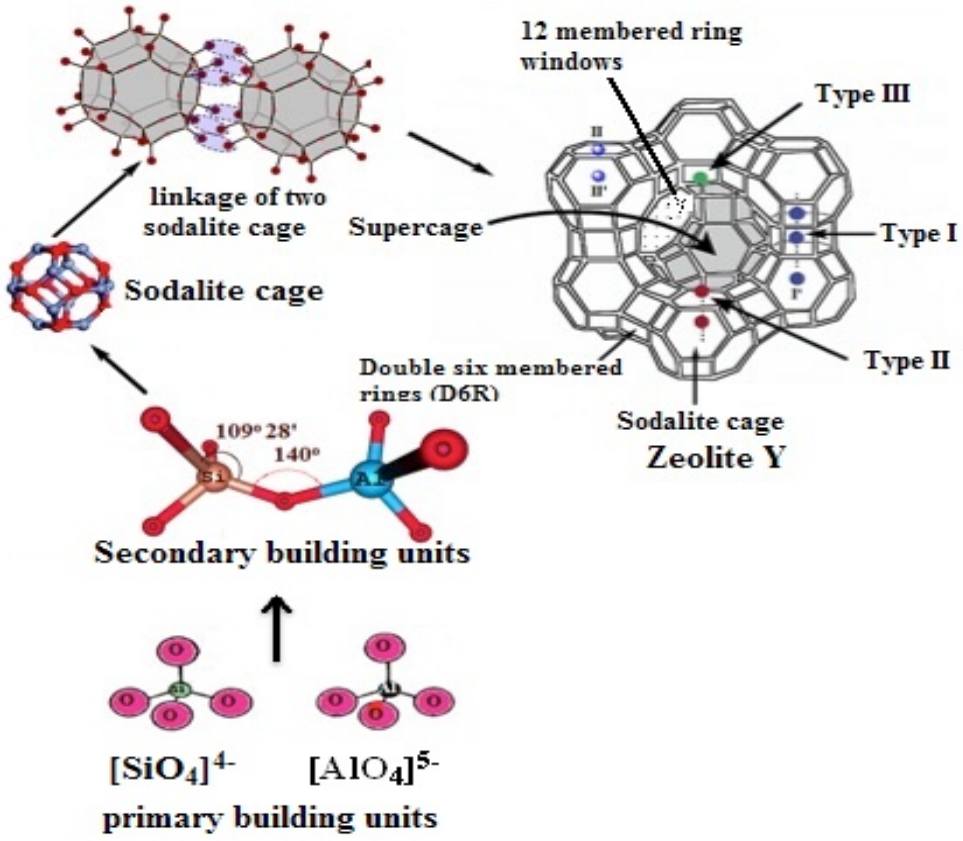

Figure 2.1 Schematic diagram of zeolite structure

In order to simplify the understanding of the structure of zeolites, the term "primary building units" and "secondary building units" are used, which are based on the framework topology of the zeolite. As shown in Figure 2.1 the tetrahedral SiO_4 and AlO_4 are called primary building units (PBUs). When these primary building units connect with each other in different ways, they produce secondary building units (SBUs) [45]. The main zeolite structures are formed based on a secondary building (SBUs) units that consists of 24 silica or alumina tetrahedral linked together; here we find 4- and 6- rings linked together to form a basket-like structure called a sodalite unit (also called a β-cage). Further cross-linking between these sodalite cages (by sharing the apical oxygen atoms)

can generate different three-dimensional zeolite frameworks, such as zeolite A or faujasite (zeolite X or Y). However, the formation of the final zeolite structure is accomplished through the participation of smaller building blocks, denoted by zeolite chemists as double four-ring (D4R) or double six-ring (D6R) building blocks [44, 46, 47] and all known zeolites are formed in a similar fashion. The pore network of a typical zeolite, which is confined by the solid framework, consists of cavities and connecting windows of uniform size occupied by cations and water molecules. In the faujasite-type zeolite, a combination of 4- and 6-rings promote the formation of the β-cage. The framework of faujasite consists of sodalite cages composed of six 4-rings and eight 6-rings. Therefore, the framework of faujasite consists of β-cage (sodalite) and α-cage (supercages); the β-cages are linked together by double six membered rings (D6R) and form the supercages of faujasite, which has a diameter of 13.0 Å [48]. Since the pore openings of the zeolite cage are primarily important for the encapsulation process, the zeolite pore openings using oxygen packing models are shown in Figure 2.2. Based on the number of rings used to construct the pore openings, typically zeolites are classified into: (i) small pore zeolites with eight - ring pores, free diameters of 0.30 - 0.45 nm (e.g. zeolite A) (ii) medium pore zeolites with 10 - ring pores of 0.45 - 0.60 nm (e.g. ZSM-5) (iii) large pore zeolites with 12 - ring pores of 0.6 - 0.8 nm (e.g. zeolites X, Y) and (iv) extra-large pore zeolites with 14 - ring pores of 0.80 – 1.0 nm (e.g. Zeolite UTD-1) [49]. Zeolites with twelve member ring pores are good candidate for the encapsulation process. Zeolite Y is one of faujasite zeolite family having twelve ring openings (i.e. large pore) and has a Si/Al ratio between 2 and 5. A unit cell contains eight

large cavities (supercages), 8 sodalite cages, and 16 double 6-ring units. The diameter of the unit cell is about 13 Å and 12-ring windows, with a free diameter of 7.4 Å [50, 51].

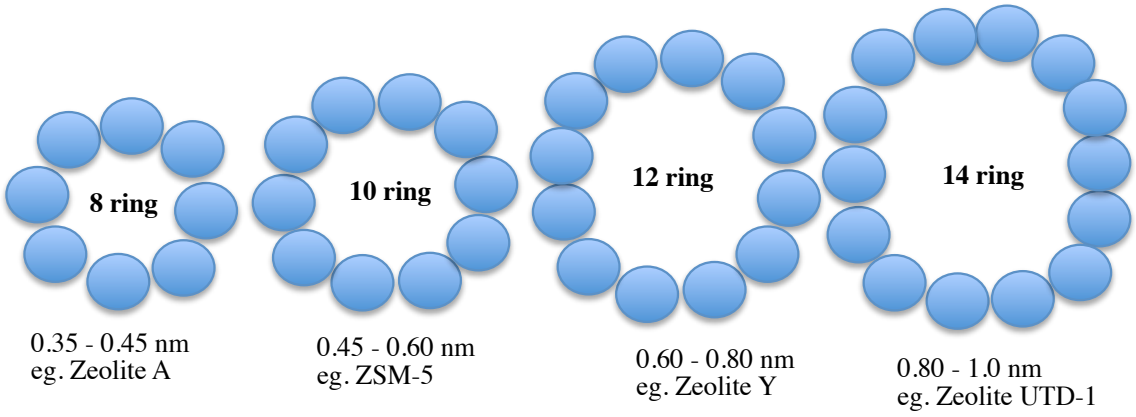

Figure 2.2 Typical zeolite pore sizes illustrated with oxygen packing models

The chemical formula of aluminosilicates, zeolites with cations, is:

$$Mx/n\ [(AlO_2)x\ (SiO_2)y].\ wH_2O \qquad (1.1)$$

Where M is a cation of valence n, w the number of water molecules. x the number of Al atoms per unit cell, usually $1 \leq y/x \leq 5$. The sum (x + y) is the total number of tetrahedra in the unit cell, and the portion represented by the square brackets is the framework composition. The exact Si/Al ratio depends on the crystalline size and the porosity. Their framework structures contain channels and cavities occupied by the cations and water molecules. The zeolites can easily be dehydrated by heating and hydrated in air without significant changes in the framework. These cations are responsible for the ion-exchange properties of the zeolites.

There are more than 40 natural zeolites that have been identified during the past 200 years and more than 150 zeolites have been synthesized. Of the synthetic zeolites the

most common are A, X, Y and ZSM-5 [52, 53]. These different synthetic zeolites were classified depending on their pore size and Si/Al ratio. Pore size based classification it is categorized into four: zeolites having small pore size (3 to 4.5Å), intermediate pore size (4.5 to 6 Å), large pore size (6 to 8 Å) and extra-large pore size (> 8 Å). Based on Si/Al ratio they are also divided into three types as zeolite with low Si/Al ratio (between l and 1.5), intermediate Si/Al ratio (between 2 and 5) and high Si/Al ratio (> 5) [54].

2.1.2. Properties of Zeolites

The arrangements of zeolites with tetrahedral units of SiO_4 and AlO_4, produces molecular sized pores in a variety of dimensions and geometries. This zeolite unique structure is the basis for its use in different application as a catalyst, ion exchange material and adsorbents [27]. The ion exchange ability of zeolite is due to the valency of aluminium +3; the AlO_4 unit will always have a negative charge, which is compensated for by the presence of water and a variety of cations (mainly groups I and II elements) at specific points of the structure. These cations and water molecules have electrostatic interaction that can easily be replaced by other ions. This makes zeolites suitable ion exchangers via an endothermic, spontaneous process. As a general rule, the higher the aluminium content the greater the ion exchange capacity [27]. The permanent negative charges, as well as the interconnection of channels and cages that run through their secondary framework structure makes both synthetic as well as natural zeolites efficient adsorbents for positively charged pollutants such as heavy metal ions and also organic pollutants [53, 55]. The catalytic activity of zeolite-based catalysts is based on their Bronsted acidity and the presence of transition metal cations in the zeolite cage structure [56, 57].

2.1.3. Zeolites as a Hosting Material

Zeolites consist of empty channels and cavities of regular diameter called micro pores. These micro pores allow mass transfer from the exterior to the interior of the zeolite matrix, provided that the size of the diffusing molecule is smaller than the dimensions of the micro pore of the zeolite. The existence of this accessible micro pore ranks zeolites at the top of the list of solids exhibiting large specific surface area. Because of this, zeolites have been extensively used as suitable hosting materials for encapsulation of various organic molecules. During the last few decades it has been proved that this molecular system with channels and cages not only serves as host for organic substrates but also has been used widely for encompassing transition metal complexes.

Synthesis of metal complexes into the supercage of supporting materials offers several advantages over their homogeneous counterparts so as to enable them to be conveniently used as catalysts for many reactions. It is generally stated that the catalytic activity of a metal complex is retained or improved by encapsulating them in zeolite cavities. In addition, the encapsulated metal complexes are able to work at milder temperatures and pressures as compared to that of conventional heterogeneous catalysts. The most attractive advantage of such heterogenized systems is the ease of separation of catalysts from reactants and products.

Besides natural zeolites over 150 synthetic varieties are known. After the first synthesis of zeolite Y by Barrer in the 1948 the use of synthetic zeolites as inorganic support has been widely recognized [47, 58]. Faujasite type zeolites have been used in a wide range of applications such as ion exchangers, catalysts and adsorbents resulting in them having

industrial importance. Zeolite Y is one class of faujasite type zeolite having large size and intermediate Si/Al ratio. It is suitable for the encapsulation of metal complexes [59] because of these physical properties. In this regard, zeolite Y has played an important role in the field of encapsulation of homogeneous transition metal complexes. Due to its large internal surface area and pore volume with extremely narrow pore size distribution as well as the fact that the functional centres in zeolite Y are homogeneously dispersed over the surface, makes Zeolite Y preferable for entrapping transition metal complexes.

2.1.4. Methods for Encapsulation of Metal Complexes into Zeolite Cage

Different synthesis routes, depending on the size of the transition metal complexes, can be used for the immobilization or encapsulation of metal complexes into the zeolite supercage. The most widely used methods for encapsulation of transition metal complexes inside the pore structure of the zeolite are the flexible ligand method (ship-in-a-bottle-method an *in-situ* method) and zeolite synthesis method.

2.1.4.1. Flexible Ligand Method

It is one of the most widely used methods where the flexible nature of the ligand is taken into consideration for the encapsulation. The ligand molecules are sufficiently small to diffuse through the zeolite pores and form complexes with the metal ions in the cavities of the zeolite host material. The metal complexes thus formed are too large to escape from the zeolite void [60]. The ligands employed in this method should have thermal stability so that it is not decomposed during the rigorous encapsulation process. Herron first introduced this idea for the synthesis of encapsulated complexes of bis(salicylaldehyde) ethylenediamine in the cavities of faujasite [60]. As presented in

Figure 2.3, the initial step in this process is the preparation of a transition metal ion exchanged zeolite by ion exchange. In the metal exchanged zeolite, water molecules, in the zeolite structure, surround the metal ion and these weak ligands can readily be replaced by other coordinating ligands. The ligands can enter the cavities of the zeolite through the restricting windows and react with the transition metal ions already present within the supercages of the zeolite [61, 62]. The complex thus formed adopts a suitable geometry and cannot diffuse out of the zeolite pores.

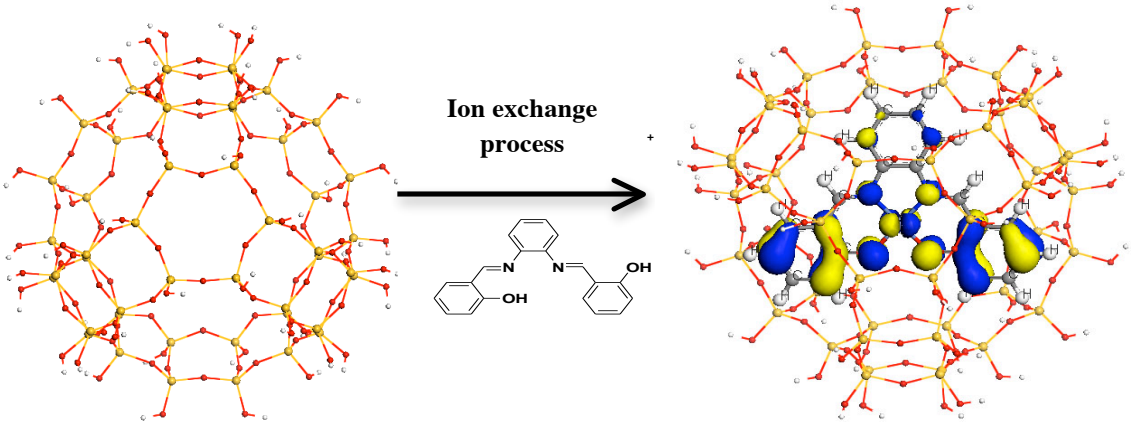

Figure 2.3 Schematic diagram for encapsulation of metal complex into zeolite cage using flexible ligand method

2.1.4.2. Ship-in-a-Bottle (*in-Situ*) Method

The other possible method that has been developed for encapsulation of transition metal complexes is the ship-in-a-bottle or *in-situ* method. According to this concept, the zeolite encapsulated metal complex can be thought as being an artistic bottle containing a ship larger than the neck of the bottle. This method is mainly used if the ligand is larger than the diameter of the zeolite pore openings. Thus, this method of encapsulation involves the

synthesis of the metal complex from smaller components of the ligand within the zeolite voids or assembling it from smaller species around the transition metal ions (Figure 2.4). Romanovsky and co-workers first introduced the concept of ship-in-a-bottle synthesis method for the preparation of zeolite encapsulated transition metal complexes of phthalocyanines [63]. The phthalocyanine complexes of iron(III), cobalt(II), nickel(II), copper(II) and manganese(II) were prepared by this method [64,65].

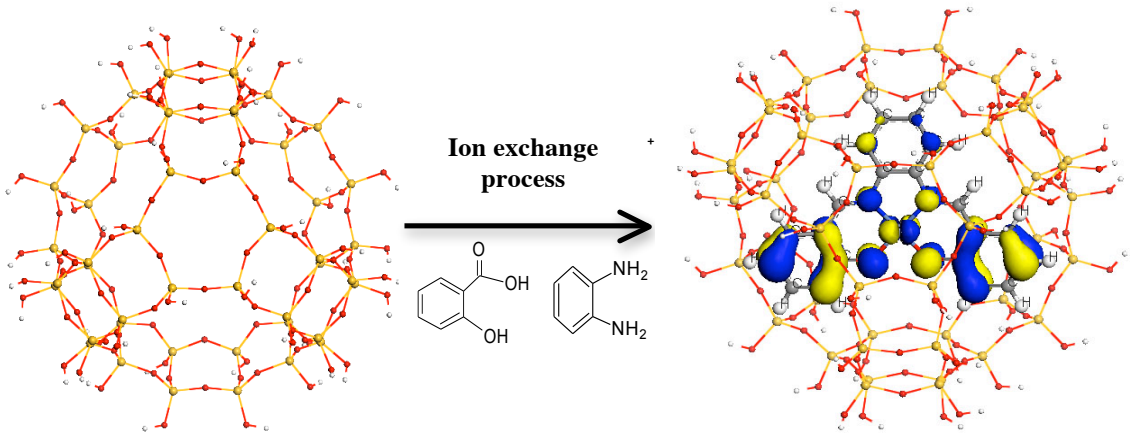

Figure 2.4 Schematic diagram for encapsulation of metal complex into zeolite cage using ship-in-a-bottle (in-situ) method

2.1.4.3. Zeolite Synthesis Method

This method involves the synthesis of the zeolite structure around the pre-formed transition metal complex [66-68]. The metal complex is considered as a template during the crystallisation of zeolites around the complexes (Figure 2.5). This method can be applied only if the metal complex is sufficiently stable in the zeolite synthesis medium (i.e. pH, temperature and hydrothermal condition) and has sufficient solubility to obtain a random distribution of the complex in the synthesis medium to form a well defined

homogeneous product. This method offers several advantages including encapsulation of well-defined intrazeolite complexes without contamination from free ligands as well as uncomplexed metal ions at milder preparation conditions. However, if organic templates are used for zeolite synthesis, they are removed by calcinations of the final product and the intrazeolite metal complex can be destroyed during this calcinations step [68, 69].

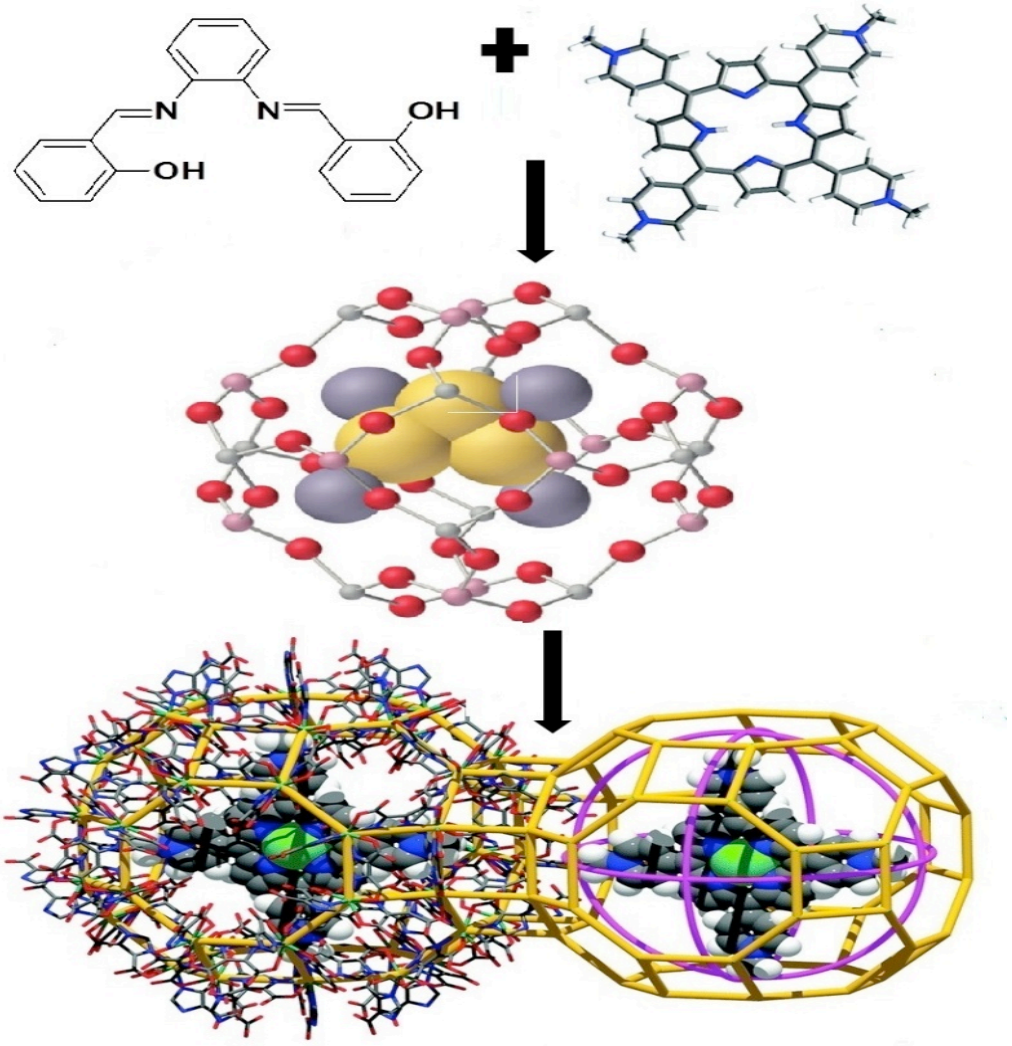

Figure 2.5 Schematic diagram for encapsulation of metal complex into zeolite cage using zeolite synthesis method

2.2. Catalysis by Zeolite Encapsulated Metal Complexes

There is a need to find an efficient and eco-friendly catalyst systems, which would operate under milder conditions without producing hazardous wastes for many industrial applications. Various attempts at the development of new catalyst systems has led to the emergence of a new system based on zeolite encapsulated metal complexes. Zeolite encapsulated metal complexes provide reaction centres for binding molecules that are mobile in the zeolite pores. The steric constraints in zeolites may distort the encapsulated molecules inducing different stability and reactivity. The presence of ligand molecules coordinated to the metal ion enhances the selectivity of metal ion exchanged zeolites in catalytic reactions. Thus, zeolite encapsulated metal complexes have catalytic properties that are different from those of metal ion exchanged zeolites and virgin metal complexes. The activity, selectivity and stability of zeolite complexes are found to be promising and may be exploited as catalysts in various industrially important reactions. Zeolite encapsulated metal complexes have profound uses in various catalytic applications due to their advantages over their homogeneous counterparts. Among the various functions of zeolite encapsulated metal complexes is its application as a heterogeneous catalyst in water and wastewater treatment through advanced oxidation processes (AOPs). This is an emerging catalytic activity in modern chemistry.

2.2.1. Metal Complexes Encapsulated Into Zeolite Cage as the Heterogeneous Catalyst in Advanced Oxidation Processes (AOPs)

Advanced oxidation processes (AOPs) were defined by different scholars. These include; A water treatment process at near ambient temperature and pressure, which involve the

generation of highly reactive radicals (particularly hydroxyl radicals (•OH) in sufficient quantity to effect wastewater purification [70]. Peralta-Hernandez et al. define AOPs as the process that involves the use of the free hydroxyl radicals (•OH) in aqueous solutions, produced by different means such as chemical, photochemical or electrochemical reactions, to promote the oxidation of organic compounds present in wastewater [71]. Gogate et al. also defined advanced oxidation processes as the procedures that generate hydroxyl radicals in sufficient quantities to be able to oxidize the majority of the complex chemicals present in effluent water [72].

Although advanced oxidation processes make use of different reacting systems, the same chemical feature characterizes all, which is the production of hydroxyl radicals. The main mechanism of AOPs is the generation of highly reactive free radicals, like hydroxyl radicals. Hydroxyl radicals (•OH) are effective in destroying organic chemicals because they are reactive electrophiles (electron preferring) that react rapidly and non-selectively with almost all electron rich organic compounds [73, 74]. As indicated in Table 2.1, hydroxyl radicals (•OH) have the highest oxidation potential (Oxidation potential, $E^0 = 2.8$ eV vs normal hydrogen electrode (NHE)) only lower than fluorine [75]. For these reasons, the generation of hydroxyl radical through advanced oxidation processes has gained the attention of many scientists and technology developers.

The mechanisms of AOPs can be defined in two steps, the first step is the generation of hydroxyl radicals (•OH) then the oxidative reaction of these radicals with molecules to convert organic pollutants to low molecular weight organic acids, carbon dioxide and water [76-78].

Hydroxyl radicals (•OH) are extraordinarily reactive species or powerful oxidants that attack most organic molecules [78]. The hydroxyl radicals can be generated by different oxidation processes, such as Fenton reagent (Fe^{2+}/H_2O_2) [79], photo-Fenton process [80], ozone(O_3) [80], Ultraviolet (UV) radiation [81], hydrogen peroxide combined with ultraviolet radiation (H_2O_2/UV) [82], O_3/UV [83], O_3/H_2O_2 and heterogeneous photo catalysis using semiconductors such as zinc oxide (ZnO) or titanium dioxide (TiO_2)-TiO_2/UV process [83].

Table 2.1 Electrochemical oxidations potential for different oxidizing agents [75-77]

Oxidizing agent	Electrochemical oxidation potential (EOP), (eV) vs NHE	Electrochemical oxidation potential relative to chorine
Fluorine	3.06	2.25
Hydroxyl radicals	2.80	2.05
Oxygen (atomic)	2.42	1.78
Ozone	2.08	1.52
Hydrogen peroxide	1.78	1.30
Hypochlorite	1.49	1.10
Chlorine	1.36	1.00
Chlorine dioxide	1.27	0.93
Oxygen (molecular)	1.23	0.90

2.2.2. Types of Advanced Oxidation Processes

Advanced oxidation processes can be classified in two groups based on the generation of hydroxyl radicals with or without using light energy [84]. The first is a non-photochemical AOP, the second a photochemical AOP. Non-photochemical AOP do not require light energy for the generation of hydroxyl radicals and it include cavitations,

Fenton and Fenton-like processes, ozonation at high pH, ozone/hydrogen peroxide, wet air oxidation, etc. [85, 86]. Photochemical oxidation processes require light energy for the generation of hydroxyl radicals and include homogenous (vacuum UV photolysis, UV/hydrogen peroxide, UV/ozone, UV/Ozone/Hydrogen peroxide, photo-Fenton etc.), and heterogeneous (photo catalysis…etc.) processes [85, 86].

The well-known advanced oxidation processes developed from the non-photochemical advanced oxidation process (heterogeneous Fenton like process), that were employed in this research work are described below:

2.2.3. Heterogeneous Fenton Like Process

Various advanced oxidation processes (AOP's) have been developed to meet the increasing demand for effective water and wastewater treatment. Among the various advanced oxidation processes, the use of heterogeneous Fenton like catalysts are a promising alternative method for the removal of dyes and other organic pollutants from the water matrix [28].

The Fenton like process is one of the advanced oxidation processes (AOP's), wherein wastewater reacts with H_2O_2 in a non-pressurized reactor, at low temperature, in the presence of a catalyst; yielding carbon dioxide and water or other oxidation products (small molecular weight organic acids). Hydrogen peroxide (H_2O_2) is a green oxidant, since it produces only oxygen and water as products. Oxidation of many organic substances by H_2O_2 is improved by the addition of a catalyst to activate the H_2O_2 molecule, leading to the formation of hydroxyl radical (•OH) [61].

Fenton like reagents can be supported by different micro porous material to make the catalyst active in heterogeneous media. Among the solid supporting materials, zeolite is the best micro porous material for supporting Fenton reagents or metal complexes. Several research works have been reported in the field of advanced oxidation process for the treatment of different industrial wastewater. However, that research has dealt with the encapsulation of transition metal complexes of certain type of Schiff base ligands on zeolites and treatment of wastewater using homogenous Fenton or photo Fenton systems [61, 62, 86, 87].

2.3. Adsorption of Pollutants through Surfactant Modified Zeolite

Adsorption is a surface phenomenon that is efficient, simple and an economically feasible process for removing different classes of organic and inorganic pollutants form water, wastewater and gas matrixes [88, 89]. When a solution containing a solute that can be absorbed comes into contact with a solid with a highly porous surface structure, liquid-solid intermolecular forces of attraction cause some of the solute molecules from the solution to be concentrated or deposited at the solid surface. The solute retained (on the solid surface) in the adsorption processes is called the adsorbate, whereas, the solid on which it is retained is called an adsorbent. This surface accumulation of adsorbate on adsorbent is called adsorption. The most popular and widely used adsorbent materials for adsorption of pollutants from wastewater are activated carbon, carbon nano tubes, modified granular charcoal and zeolites. Among these, zeolites are well-known adsorbent materials owing to their unique characteristics including ion exchange capability or ability to act as a molecular sieve.

2.3.1. Modification of Zeolites with Cationic Surfactants

The negative charge on the external surface of a zeolite favours the ion exchange of certain cationic pollutants, but not anionic pollutants like Cr(VI) [90]. Additionally, due to their hydrophilic surface properties, zeolites usually have little or no affinity for particular organic pollutants [91, 92]. Hence, the development of materials with the capability to adsorb anions, cations, and neutral molecules is very important. Many research papers have reported that the net negative charge and hydrophilic surface properties of zeolites could be controlled by organic functionalization of the external surface of the zeolite material [93-95]. The common surface functionalization of these inorganic materials is via adsorption of cationic surfactants. It has been demonstrated that the cationic surfactants have a great affinity to this negative charge and surfactant modified zeolites (SMZ) are produced by treating zeolites with long alkyl groups of cationic surfactants.

Surfactants are wetting agents, which reduce the surface tension of the liquid and the interfacial tension between two liquids. The molecular structure of surfactant, represented in Figure 2.6, is made up of water-soluble (hydrophilic) and water insoluble (hydrophobic) parts. The hydrophobic part consists of an uncharged alkyl group that can be straight, branched, cyclic or aromatic. Depending on the nature of the hydrophilic part, surfactants are classified as cationic, anionic and non-ionic. In the cationic surfactant, the hydrophilic part is positively charged while in anionic surfactant, the hydrophilic part is negatively charged. Non-ionic surfactants do not have an electrical charge.

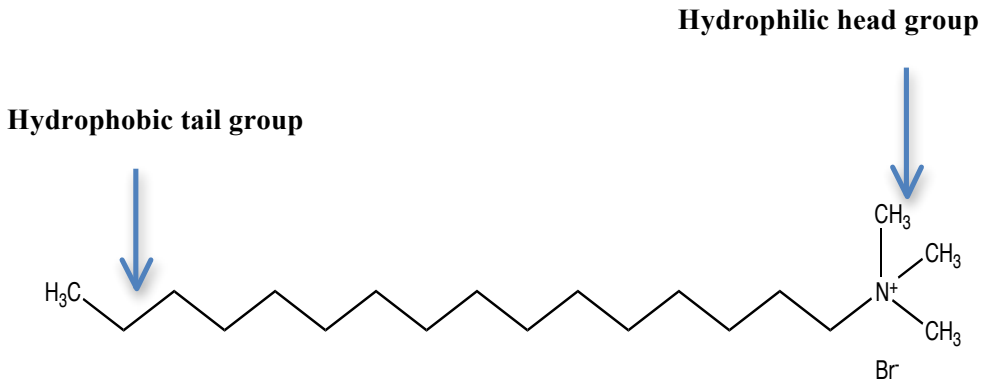

Figure 2.6 Molecular structure of haxadecyltrimethyl ammonium bromide (HDTMA-Br) surfactant

Cationic surfactants increase the fractional organic carbon content and enhance the ability of zeolite for adsorption of non-polar hydrophobic organic contaminants. It was observed that the longer the tail group of the cationic surfactant, the more stable it is the surface [96]. Therefore, mostly cationic surfactants containing long alkyl groups like tetramethyl ammonium (TMA) [97], tetraethyl ammonium bromide (TEA) [98], hexadecyltrimethyl ammonium bromide (HDTMA) [99], octadcyltrimethyl ammonium bromide (ODTMA) [100,101], benzyltrimethyl ammonium chloride (BTMAC) [102], (SDBAC) [102], benzyltetradecyldimethyl ammonium chloride (BDTDAC) [103] are used for surface modification of zeolites.

The adsorption of a cationic surfactant on the external surface of a zeolite is mainly governed by ion exchange and hydrophobic interactions [104, 105]. As shown in Figure 2.7 (a & b), at a low surfactant concentration, the head groups of surfactant cations are exchanged with the exchangeable cations of the zeolite until a monolayer of surfactant cations is formed at the external surface of zeolite. At concentrations above the critical micelle concentration (CMC) of the surfactant, hydrophobic interaction between the tail

groups of the surfactant are responsible for the formation of a bilayer on the zeolite external surface [104]. Hence, the external surface charge of the zeolite is changed from negative to positive and displays anion exchange capacity [106-109].

The zeolite framework structure contains channels and/or interconnected voids of discrete size having small openings that permit only smaller size molecules to do enter. Thus, large surfactant molecules do not have access to the internal surface and sorbs only to the external surface of zeolite. Consequently, the external cation exchange capacity (ECEC) determines the exchange capacity of the zeolite surface for bulky surfactants.

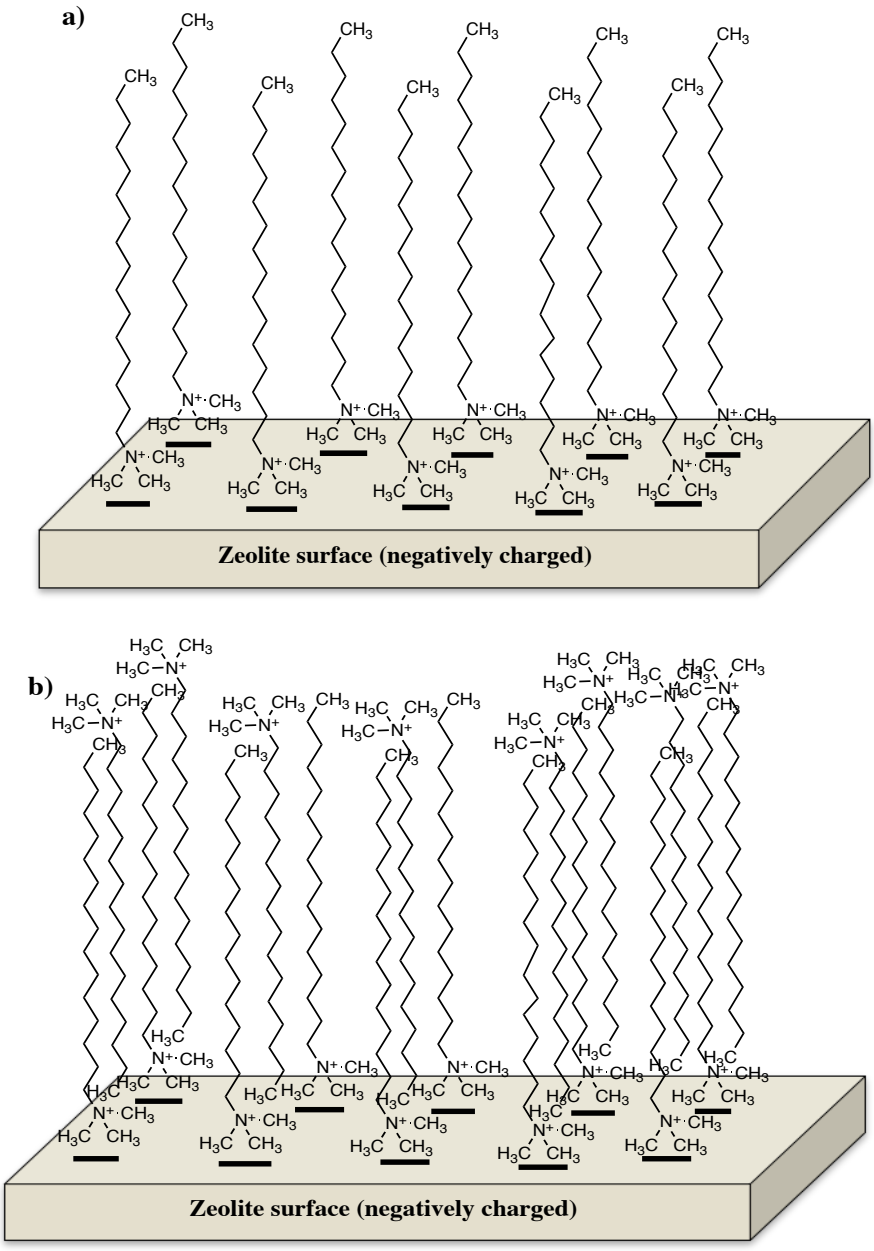

Figure 2.7 Schematic diagrams of HDTMA configurations on the zeolite surface **a**) at 100% of ECEC (monolayer) **b**) at 200% of ECEC (bilayer)

2.4. Characterization Techniques for Zeolite Encapsulated Metal Complex and Surfactant Modified Zeolite

The main issue in the synthesis of zeolite encapsulated metal complexes is to identify appropriate conditions at which well-defined distribution of transition metal complex occur in the zeolite cage, instead of being concentrated on the zeolite external surface. Moreover, the encapsulation of metal complexes in pores of zeolite cage helps to combine the characteristics of both neat zeolite and metal complex to obtain new hybrid catalysts. Therefore, a complete characterization of synthesized catalyst as compared to neat metal complex and neat zeolite is necessary to ensure encapsulation process is properly done. The proper encapsulation of transition metal complexes into zeolite cage can be ascertained by several physico-chemical characterization methods. In general, zeolite encapsulated metal complexes are characterized to address the following aspects: the composition of neat zeolite and metal complexes residing in the zeolite cage; the framework of zeolite is preserved after the encapsulation of metal complexes; thermal stability of the encapsulated metal complexes as compared to neat metal complexes and neat zeolite; morphological changes associated with encapsulation process; effect of molecular confinement on the conformational geometry and the mobility of the complexes inside the zeolite cage; internal versus external confinement and the distribution of guest compounds in zeolite host; nature of the metal complex formed in zeolite cavity compared to neat metal complex and neat zeolite; the effect of host-guest interactions on the structure of metal complex.

Besides such physico-chemical parameters, a theoretical investigation of the physical and chemical properties of metal complexes is important in order to study successful

immobilization or encapsulation of metal complexes into the zeolite supercage. The use of quantum chemical calculations has provided a better understanding for the properties of zeolite-encapsulated complexes and the science behind their catalytic activity. Quantum chemical calculation can play a vital role in understanding the fundamental aspects of the encapsulated metal complexes in comparison to the neat metal complexes. Quantum chemical calculation based on density functional theory (DFT) is a simple working tool in elucidating chemical reactivity of the catalyst [110, 111]. DFT calculation is also applied to understand the change in structural or geometrical parameters through calculations of bond length, bond angle and dihedral angle of neat and encapsulated metal complexes. Besides these the stability and reactivity of encapsulated complexes were investigated through highest occupied molecular orbitals (HOMO) and lowest unoccupied molecular orbitals (LUMO) energies of the metal complexes upon encapsulation into zeolite supercage. Some of characterization techniques applied for proper synthesis of zeolite encapsulated metal complex and surfactant-modified zeolite are:

2.4.1. X-Ray Diffraction (XRD)

X-ray diffraction allows obtaining relevant information on solid samples of neat zeolite, metal complex encapsulated into zeolite cage and surfactant-modified zeolite whether the structure of zeolite Y framework is preserved or not after the encapsulation of complexes and surface modification. The different information to be obtained by XRD is the crystalline structure, the average particle size, the unit cell dimensions and the constituents of the cell. This technique is based on the principle of diffraction or

dispersion of light waves when an X-ray beam bombards a sample. X-rays are electromagnetic radiation with photon energies typically in the range of 100 eV-100 KeV. For diffraction applications, only short wave length X-rays (hard X-rays) in the range of 10 to 0.01 nm (1-120 KeV) are used. Because the wavelength of X-rays is comparable to the interatomic spacing, they are ideally suited for probing the structural arrangement of atoms and molecules in a wide range of materials [86,112-114].

X-ray is generated after bombardment by an electron beam of a stationary or rotating solid target. Electrons collide with atoms in the solid target producing a continuous spectrum of X-rays (Figure 2.8). Common solid targets used in X-ray tubes include Cu and Mo, which emit 8 KeV and 14 KeV X-rays with corresponding wavelengths of 1.54 Å and 0.8 Å, respectively [115].

W. L. Bragg developed an Equation that shows relationship between several factors, which became the basic Equation for diffraction. Those factors are as follows:

1. The distance between similar atomic planes in a sample (interatomic spacing) or *d*-spacing (Å).

2. The angle of the incident X-ray beam on the surface of crystal atom, or θ angle.

3. The wavelength of the X-radiation, or λ (Å).

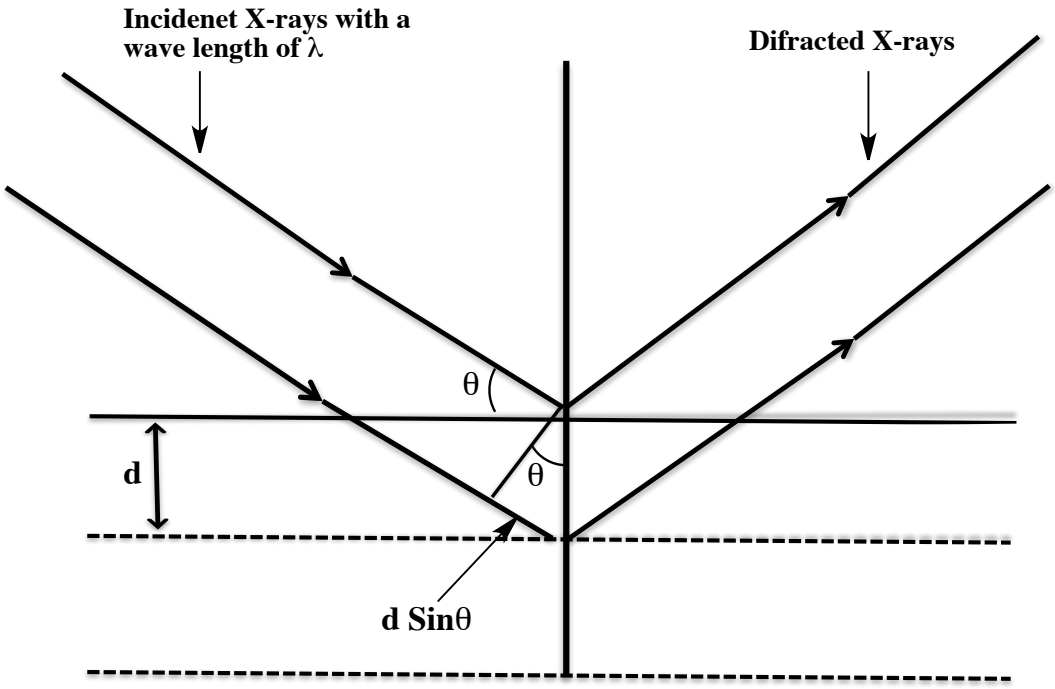

Figure 2.8 Schematic representation of the incident of X-ray beam on the surface of crystal atom

From geometrical considerations (Figure 2.8) it can be shown that X-rays reflected from two adjacent parallel planes will be in the same phase and thus interfere constructively when the following condition is fulfilled, which is known as the Bragg Equation (Eq.2.1).

$$2dSin\theta = n\lambda \qquad (2.1)$$

where d is the inter-plane distance, θ is the angle of diffracted light, λ is the wavelength of incident light and n is the order of diffraction. Considering first order diffraction for a given wavelength of incident light, the direction of the diffracted X-ray light is,

therefore, depends only on the magnitudes of θ and d. Thus by measuring the diffraction values of 2θ, the interplanar distances in the crystal can be elucidated.

2.4.2. Scanning Electron Microscope (SEM)

The surface analysis of zeolite encapsulated metal complex before and after Soxhlet extraction and also surfactant-modified zeolite was carried out using scanning electron microscope (SEM). In SEM instrumentation a narrow beam of electrons from a tungsten filament is scans the sample. In order to protect the sample from surface charging and thermal damage due to collision with electron beam, a thin film of gold is coated over them. The amount of back-scattered or secondary radiation is noted as a function of the primary beam. Through surface analysis information regarding the presence of materials adsorbed on the surface of the support and the morphological changes associated with encapsulation and surface modification may be extracted. The major advantage of this method is its ability to give evidence on the effectiveness of Soxhlet extraction in removing the substances adsorbed on the surface as well as the effect of surfactant modification on the surface of the neat zeolite [113,114,116].

2.4.3. N_2 Adsorption/Desorption Isotherm

The surface area and pore volume of zeolite encapsulated metal complexes and the surfactant-modified zeolite were performed to investigate the encapsulation process in metal complexes and surfactant-modified zeolites. This is performed through comparing the neat zeolite surface area and pore volume to those of the zeolite encapsulated metal complexes and the surfactant modified one. This method involves the measurement of the

amount of gas adsorbed by the respective samples. Initially a very small amount of sample is accurately weighed and taken in a clean dry sample tube. It is then pre-treated under reduced pressure and heat (usually at 473 K), and flowing gas to remove adsorbed contaminants that may be acquired from atmospheric exposure. After the volatile impurities on the surface of the sample are completely removed the sample is then allowed to cool to room temperature. An adsorbate (typically nitrogen) is dosed to the solid in controlled increments. After each dose of adsorbent, the pressure is allowed to equilibrate and the quantity adsorbed is calculated. The quantity adsorbed at each pressure defines an adsorption isotherm, from which the quantity of gas required to form a monolayer over the external surface of the solid is determined. With the area covered by each adsorbed gas molecule known, the surface area can be calculated. The BET Equation (Eq. 2.2) used for calculating the surface area is;

$$\frac{p}{V(p_0 - p)} = \frac{1}{V_m C} + \frac{(C-1)p}{V_m C p_0} \qquad (2.2)$$

where V is the volume of gas adsorbed at relative pressure p / p_0, V_m is the volume of gas in the monolayer, p_0 is the saturation vapour pressure of the adsorbate and C is the BET constant that is related to the heat of adsorption.

The plot of the left side terms in the BET Equation versus p / p_0 results in a straight line with slope $(C - 1) / (V_m C)$ and intercepts $1 / (V_m C)$. The volume of gas in the monolayer V_m can be obtained from these values and hence the number of moles of nitrogen adsorbed X_m (mol) can be calculated. Then the BET surface area S_{BET} ($m^2 g^{-1}$) is determined using Equation 2.3.

$$S_{BET} = X_m N_A A_m \quad (2.3)$$

where N_A (mol^{-1}) and A_m ($m^2\ g^{-1}$) represent the Avogadro number and the cross sectional area of the adsorbate molecule, respectively.

The total pore volume of the sample is computed by converting the volume of N_2 adsorbed at $p / p_0 \approx 0.9$ and using Equation 2.4.

$$V_{tot} = V_{ads} \times D \quad (2.4)$$

where V_{tot} is the total pore volume at $p / p_o \approx 0.9$, V_{add} is the volume of gas adsorbed at $p / p_o \approx 0.9$ and D is the density conversion factor.

The micro pore volume distribution based on N_2 adsorption isotherms can be derived using several methods, such as non-local density functional theory (NLDFT) methods [117], Dubinin-Astakhov (DA) Equation based on micro pore filling theory [118] and Horvath-Kawazoe (HK) method based on the interaction potential between adsorbate and adsorbent [119]. Among the methods that proposed by Harvath and Kawazoe (HK) is the widely employed method [120-122] for the evaluation of micro pore volume distribution in micro porous materials. In this study the effect of encapsulation of a metal complex and surfactant modification onto the neat zeolite pore volume was investigated using HK methods.

2.4.4. FT-IR Spectroscopy

FT-IR spectroscopy provides valuable evidences for the formation of metal complexes in zeolite pores. The ligand molecules are coordinated to transition metal cations if different spectral patterns appear in the free and chelated state or if characteristic bands exhibit shift in frequency upon coordination in the zeolite cage [62, 86].

2.4.5. Electron Paramagnetic Resonance (EPR)

Electron paramagnetic resonance (EPR) spectroscopy, also called electron spin resonance (ESR) spectroscopy, is used to study both molecular and electronic structural information of the paramagnetic ions, and consequently the effect of molecular confinement on the conformational geometry and the mobility of the complexes inside the zeolite cage [123-125]. Since the majority of Ni(II) complexes are square planar and diamagnetic [126], it is EPR inactive. However, Fe(III) and Cu(II) complexes exhibit paramagnetic properties and thus EPR active. A typical EPR spectrum consists of one or more bands depending on the number of unpaired electrons. Analysis of the shape and number of bands in the EPR spectrum provides information about the type of paramagnetic species, e.g. the structure of a free radical, and the coordination sphere environment around the metal centre in a coordination complex. EPR spectroscopic measurements can be performed at variable temperature. Usually, an EPR spectrometer operates at a given magnetic field strength B_0 (measured in gauss or tesla, 1G = 10^{-4} T) that is commonly expressed in frequency units since there is a linear relationship between frequency and magnetic field strength. Excitation of spin states generally occurs in microwave spectral regions.

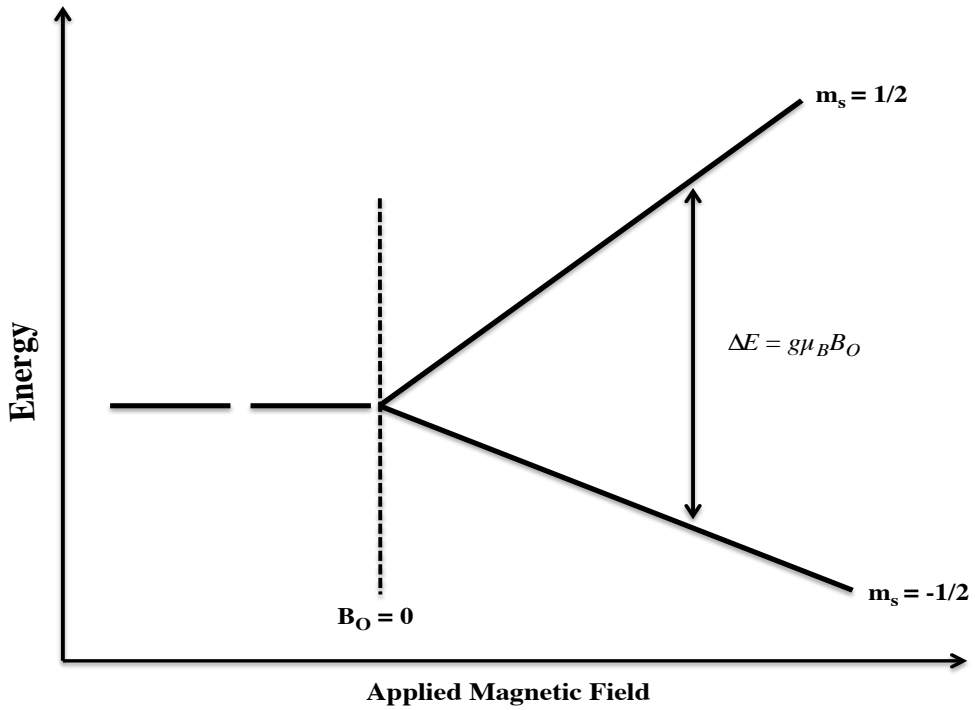

Figure 2.9 Splitting of spin states under applied external magnetic field (Zeeman effect)

For a paramagnetic metal ion with a single unpaired electron, the spin quantum number is *s* equals ½. There are two possible spin states, namely M_s = +½ and M_s = –½. In the absence of a magnetic field, these states are degenerate. Considering a one-electron case, application of a magnetic field, B_0, the interaction between the unpaired electron and the magnetic field leads to a splitting of the energy level (Figure 2.9). This is called the Zeeman effect and the energy difference ΔE is given by Equation 2.5, below.

$$\Delta E = g \mu_B B_0 \qquad (2.5)$$

where g, B_0 and μ_B represent the gyroscopic constant, the applied magnetic field and the Bohr magneton, respectively.

The gyroscopic is a dimensionless constant is given by the ratio $2\ \mu_e / \mu_B$, where μ_e is the electron magnetic moment (9.2848×10^{-24} J T^{-1}). For a free electron, $g = 2.0023$. For a metal ion, spin-orbit coupling leads to *g*-values that are significantly different from that of a free electron. The *g* value obtained from an EPR experiment provides diagnostic information about the system being investigated. For a paramagnetic metal centre, the *g* value is characteristic of the oxidation state (i.e. the number of unpaired electrons), the coordination environment and the molecular symmetry [125-127].

2.4.6. Thermogravimetric Analysis (TGA)

Thermogravimetric analysis (TGA) is an experimental test that is performed on given samples for determining changes in weight in relation to change in temperature. Such analysis requires high degrees of precision in three measurements, i.e. weight, temperature and temperature change. The weight change observed during a specific temperature range can be correlated with the composition and the thermal stability of the sample. This technique is extensively used to determine the composition, thermal stability, moisture and volatile content of samples.

A sensitive analytical balance (thermo balance), a furnace, a purge gas system and microprocessors to control and display of output data are the main component of this instrument. The balance cell is the most important part of any TGA system and consists of a high-precision balance with a pan loaded with the sample. The sample is placed within an electrically heated oven with a thermocouple to accurately measure the variations of temperature. During the measurement, inert gases like nitrogen or argon are purged to avoid any possible reaction of the sample with the atmospheric gases. Analyses

were carried out by measuring the weight change as a function of temperature [62, 86, 112].

One of the advantages of this method is the small amount of sample required for the analysis (10 –20 mg). The TGA method provides information concerning the loss or gain of weight by the sample. The curves obtained during the analysis are the general behavioural patterns and thus cannot be considered as fingerprints of the materials, since any small change in the parameters such as temperature changing rate, purge gas pressure, sample size or even the sample morphology can affect the shape of the curve significantly.

2.4.7. Analysis of Si, Al, Na, Fe, Ni and Cu Metal Ion in the Zeolite Encapsulated Metal Complex Samples

Chemical analysis is used to investigate the composition of neat zeolite and metal complexes residing in the zeolite cage. The Si/Al ratio of the zeolite complexes is compared with pure zeolite to verify whether the zeolite framework is preserved during encapsulation of metal complexes in the zeolite cage [112,113,128].

2.4.8. CHN Analysis

The quantitative analyses for carbon, hydrogen and nitrogen in the neat metal complexes and zeolite encapsulated metal complexes are performed using a CHN analyser. In CHN analysis the compound is completely combusted and the amounts of products are measured. Experimentally a known amount of sample (2-5 mg) is sealed in an aluminium or tin capsule. The sample then passes into a pyrolysis tube and is heated at

approximately 900 °C in an atmosphere of pure O_2. Carbon, hydrogen and nitrogen are oxidized to CO_2, H_2O and nitrogen oxides, respectively. A stream of helium is used as a carrier gas. The carrier gas then transports the mixture of CO_2, H_2O and N_2 into the analysing chamber where they are separated using a specialized type of gas chromatography (frontal chromatography), which does not require a mobile phase. Detection of the gases is conducted through a thermal conductivity detector [129, 130].

2.4.9. Zeta Potential Measurements

The zeta potential, also known as electro kinetic potential, is an important parameter to describe the surface properties of materials. It refers to the electric potential associated with an electrical double layer around a colloid at the radius of shear, relative to the value of the potential in the bulk of the solution far from the colloid, where the radius of shear is the radius of the entity made up of the colloid and the rigid layer of ions at the surface of the colloid. The value of the zeta potential indicates possible behaviour of the surface properties of zeolite before and after being subjected to surfactant modification [131]. There are many factors that affect the zeta potential value, such as type of particles, pH, concentration of particles, background electrolyte and addition of other substances, i.e. surfactants, heavy metals etc. The pH of solution has a significant impact on the value of zeta potential. With the change of pH, stable or unstable system of charge stabilization can be achieved [132]. The value of zeta potential also provides information about the character of the particle surface itself as well as about the processes on the surface (e.g. adsorption, ion exchange, modification).

3. Materials and Methods

3.1. Chemicals

The zeolite Na-Y (99%, Sigma Aldrich, India), Salicylaldehyde (99%, Sisco Research Laboratories PLC, India), zeolite Na-Y (99%, Sudie Chemie Company Ltd., India), ethylenediamine (99%, Sisco Research Laboratories PLC, India), 5,5'-dimethyl-1-pyrroline-N-oxide (DMPO) (99%, Sigma-Aldrich, India), dimethyl sulfoxide-d_6 (DMSO) (99.9%, Sigma-Aldrich, India), 1,10-phenanthroline (99%, Sigma-Aldrich, India), 2,2'-bipyridine (99%, Sigma-Aldrich, India), standard 4-chloro-3-methyl-phenol (PCMC) (AR, Sigma-Aldrich, India), 4-chloro-3-methyl-phenol (PCMC) (99%, Sigma-Aldrich, India), Ortho-phenyl phenol (OPP) (99%, Sigma-Aldrich, India), *o*-Phenylenedaimine (99.5%, Sigma-Aldrich, India), tetrabutyl ammonium bromide (98%, Sigma-Aldrich, India), haxadecyltrimethyl ammonium bromide (HDTMA-Br) (AR, Sigma-Aldrich, India). All other chemicals used were of AR quality.

3.2. Instruments Used for Characterization Techniques

The Schiff base ligands formed from different organic precursors were characterized in d_6-dimethylsulfoxide (DMSO) solution at room temperature using tetramethylsilane (TMS) as internal standard using Nuclear Magnetic Resonance (NMR) spectrometer (ECA 500 MHz, Jeol, Japan).

The ESI mass spectra of the metal complexes were analysed using, Mass Spectrometer (Finnigan LCQ Advantage MAX, Thermo Electron Corporation, USA).

The X-ray powder diffractograms of the samples were recorded with Cu-Kα radiation (λ = 0.1548 nm) applying steps of 0.05 degrees from 5 to 60 degrees using X-ray powder diffraction (Miniflux 11, Rigaku diffractometer, USA).

Scanning electron microscopy analysis of zeolite encapsulated metal complex before and after Soxhlet extraction and also surfactant-modified zeolite was carried out using High-resolution scanning electron microscope (HR-SEM) (FEI Quanta FEG 200, FEI Company, Netherlands).

Surface area and pore volume measurements of the samples at liquid nitrogen temperature were performed using Micromeritics surface area analyser (ASAP-2020, Micromeritics Instruments Corporation, USA).

Infrared spectra of Schiff base ligands, metal complexes, neat zeolite Y, metal exchanged zeolite, zeolite encapsulated metal complexes, neat surfactant and surfactant-modified zeolites in the region 4000 - 400 cm^{-1} using KBr mull technique were recorded using Fourier Transform Infrared Spectrophotometer (FT-IR) (1800, Perkin-Elmer, USA).

The electron paramagnetic resonance (EPR) spectra of the metal complex and catalyst were recorded using EPR spectrometer (EMX-Computer controlled, Bruker BioSpin, Germany).

The TGA analysis of the samples was recorded from room temperature to 800 °C at a heating rate of 10 °C/min in nitrogen atmosphere using thermal analyser (TGA Q50, TA instruments, USA).

The carbon, nitrogen and hydrogen analysis in the zeolite encapsulated metal complex and in the neat metal complex was carried out using CHN analyser (Vario MACRO cube elemental, Elementar Analysensysteme GmbH, Germany).

The metals such as; sodium, aluminium, iron, nickel and copper present in the neat zeolite and zeolite encapsulated metal complexes were analysed using Inductive Coupled Plasma (ICP) (Prodigy Xp high dispersion, Teledyne Leeman Labs, USA) and Atomic absorption spectroscopy (AAS) (Nova 350, Analytik jena AG, Germany). The amount of silicon content present in the neat zeolite and zeolite encapsulated metal complexes were analysed using gravimetric methods accurately weighing 1 g of zeolite sample (W) in a beaker. About 20 mL of conc. H_2SO_4 was added and heated strongly while stirring. It was then cooled, diluted with water (100 mL) and filtered using a Whatman ashless filter paper. The filtrate was then collected in a volumetric flask. The residue was heated in a platinum crucible, cooled and weighed (W_1). Hydrofluoric acid was then added drop wise and heated strongly to dryness to remove silica as H_2SiF_6. This process was repeated three times. The remaining solid was then ignited to 800 °C for about 1 h, then cooled and weighed (W_2). The amount of silica present %Si in the sample was calculated using the equation 3.1.

$$\%\mathrm{Si} = \frac{W_1 - W_2}{W} \times 100 \qquad (3.1)$$

The residue in the crucible was treated with potassium persulphate and fused till a clear melt was obtained. Subsequently, it was dissolved in water and combined with the earlier

filtrate collected in the standard flask. Quantitative analysis of metals was based on calibration curve constructed with a series of standard solutions for each metal.

Zeta potential measurements were carried out using a Zetasizer (Nano ZS series, Malvern Instruments, UK), equipped with a microprocessor unit taking suspensions of 0.0125 g/100 mL of neat zeolite and surfactant-modified zeolite.

Hydrophobicity of neat zeolite, 100%-CSMZ (mono layer) and 200%-CSMZ (bilayer) was determined using little modification of the procedure proposed by Silvio et al. [109]. Under constant stirring 1 g sample was placed in a separation funnel with 100 mL of double distilled water. Then, 100 mL of hexane (98%) was added and stirred for 5 min the mixture was then let to stand for 5 min in order allow the solid to settle. The amount of zeolite transferred to the organic phase was determined by filtration followed by drying and weighing.

Total organic carbon (TOC) of the system was analysed using total organic carbon analyser (TOC-LCPH, Shimadzu Corporation, Japan).

The concentration of 4-chloro-3-methyl phenol (PCMC) was determined with high-performance liquid chromatography (515 Series, Waters, USA) equipped with diode array detector and a C18 column (4.6 mm × 250 mm) in a reversed-phase arrangement.

Investigations to identify the degradation intermediates of PCMC were made using liquid chromatography coupled mass spectrometry (ACQUITY UPLC-Xevo TQD, Waters, USA), equipped with a photo diode array (PDA) lamp, and a mass spectrum (MS) using an atmospheric pressure chemical ionization (APCI) source. The MS was operated in

positive-ion (ES+) and negative-ion (ES−) electrospray modes with a mass range of 10 - 500 m/z.

The pollutant removal efficiency of the given catalyst and adsorbent was determined using UV-Vis Spectrophotometer (UV-1800, Shimadzu, Japan).

3.3. Synthesis of Catalyst

3.3.1. Synthesis of Ligands

3.3.1.1. N,N′-Ethylenebis(Salicylimine) or Salen Ligand

For the synthesis of the ligand, 2 mmol of salicylaldehyde was added to 50 mL of ethanol and then the solution was maintained at 70 °C under stirring. After 30 min, 1 mmol of ethylenediamine in 25 mL of ethanol was added and the temperature maintained for 5 min. The solution was cooled in ice bath until a yellow coloured crystalline product was obtained. The product was filtered, washed with cold ethanol and dried.

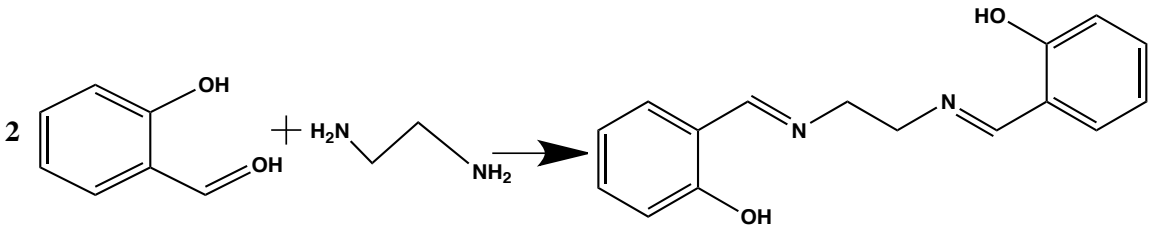

Figure 3.1 Synthesis of N,N′-Ethylenebis(salicylimine) or salen ligand

3.3.1.2. N,N′-Disalicylidene-1,2-Phenylenediamine or Salophen Ligand

N,N'-disalicylidene-1,2-phenylenediamine ligand was synthesized as follows. An ethanolic solution of 2 mmol of salicylaldehyde was added drop wise to an ethanol solution of 1 mmol of *o*-phenylenediamine. The reaction mixture was refluxed in a water

bath at 50 °C for 2 h under constant stirring. The solution was cooled in atmosphere to obtain yellow coloured solid product. The product was washed with cold ethanol several times followed by recrystallization from ethanol.

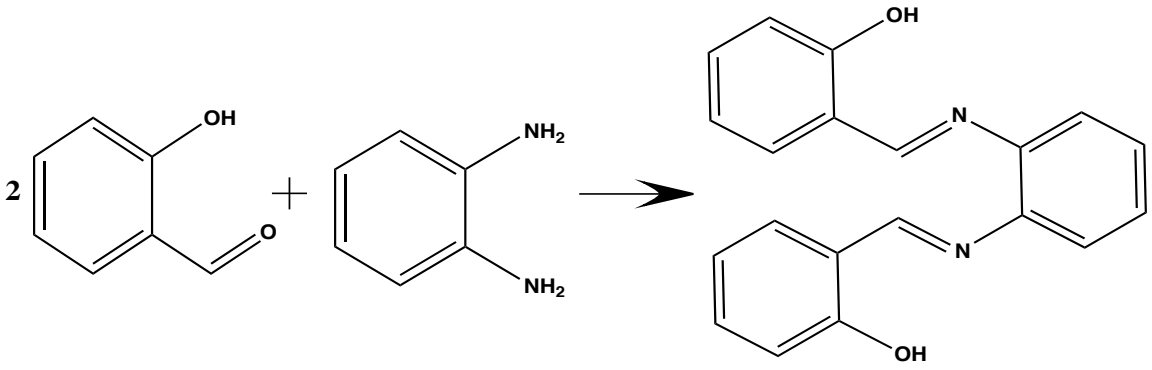

Figure 3.2 Synthesis of N,N′-disalicylidene-1,2-phenylenediamine or Salophen ligand

3.3.2. Synthesis of Metal Complexes

3.3.2.1. Iron(III), Nickel(II) and Copper(II) N,N'-Ethylenebis(Salicylimine) Complex

The N,N′-ethylenebis(salicylimine) metal (Fe(III), Ni(II) and Cu(II)) complexes were prepared by reacting 1 mmol of N,N′-ethylenebis(salicylimine) in methanol with 1 mmol of the respective metal salts (i.e. $FeCl_3$, $NiCl_2$ and $CuSO_4$). The homogeneous solution was then stirred for 3 h and the solution exposed to the atmosphere to obtain solid product. The products were filtered, washed with cold methanol and recrystallized from methanol.

3.3.2.2. Iron(III) and Nickel(II) (2,2- bipyridine) (1,10- phenanthroline) Complex

The complexes were synthesized by reacting the respective metal salts with the ligands in 1:1:1 mole ratio, i.e. one mole of metal salt (i.e. $FeCl_3$ and $NiCl_2$): one mole of 2,2'-bipyridine and one mole of 1,10-phenanthroline. A 2.0 mmol solution of 1,10-

phenanthroline in 25 mL of ethanol was added drop wise to 2.0 mmol solution of respective metal salts in 10 mL of water while stirring at room temperature. Subsequently, 2 mmol 2,2'-bipyridine in ethanol solution was added drop wise to the homogenous solution m while stirring. The solution mixture was continuously stirred at room temperature for 1 h and allowed to stand for 5 days until crystals had formed.

3.3.2.3. Iron(III), Nickel(II) and Copper(II) N,N'-Disalicylidene-1,2-Phenylenediamine Complex

The salophen-metal (Fe(III), Ni(II) and Cu(II)) complexes were prepared by reacting 1 mmol of N,N'-disalicylidene-1,2-phenylenediamine in methanol with 1 mmol of the respective metal salts (i.e. $FeCl_3$, $NiCl_2$ and $CuSO_4$). The homogeneous solution was then stirred for 6 h and then left until crystallization had occurred. The products were recrystallized from methanol.

3.3.3. Preparations of Iron(III), Nickel(II) and Copper(II) Exchanged Zeolite

The metal exchanged zeolite was prepared with little modification of a previously reported method [133,134]. A 3 g portion of the respective metal salts i.e. $FeCl_3$, $NiCl_2$ and $CuSO_4$, were dissolved in 250 mL of warm distilled water. To each solution 5 g of zeolite Y was added while stirring. The reaction mixture was subsequently heated under reflux for 24 h and cooled. The solid was filtered and washed thoroughly with hot distilled water several times till all the unattached metal ions were removed from the surface of the zeolite. The washed solids were dried for 15 h at 150 °C in oven. The metal exchange process was repeated a further two times to achieve maximum metal exchange.

3.3.4. Synthesis of Zeolite Encapsulated Metal Complexes

3.3.4.1. Iron(III), Nickel(II) and Copper(II) N,N'-Ethylenebis(Salicylimine) Complex Encapsulated into Zeolite Cage

For the encapsulation of metal complexes into a zeolite supercage, 1 g of the corresponding metal exchanged zeolite and 2 mmol salicylaldehyde were dissolved in 25 mL of methanol and refluxed under constant stirring for 6 h. Subsequently, the solution was cooled and the solid product removed by filtration. A solution of 1 mmol ethylenediamine in 25 mL methanol was added to the solid product and refluxed, while stirring, for 3 h.The solution was then filtered and the solid filtrate was subjected to Soxhlet extraction with ethanol, dichloromethane and diethyl ether till the washings were colourless. Finally, any uncomplexed metal ion remaining in the surface or inside the zeolite cage after complex formation, was removed by a back exchange process, i.e. by stirring the zeolite encapsulated metal complex and 0.01 M of NaCl solution for 6 h. The solid product was then washed with hot water and dried at 100 °C overnight.

3.3.4.2. Iron(III) and Nickel(II) (2,2-bipyridine) (1,10- phenanthroline) Complex Encapsulated into Zeolite Cage

Encapsulations of the complexes into the zeolite supercage were done using *in-situ* or ship-in-a-bottle method. About 1 g of the corresponding metal exchanged zeolite and 1 mmol 1,10-phenanthroline dissolved in 25 mL of ethanol was refluxed under permanent stirring for 24 h. Subsequently, the solution was cooled and the solid product removed by filtration. A solution of 1 mmol 2,2'-bipyridine in 25 mL ethanol was then added to the solid product and refluxed, while stirring, for 24 h at a constant temperature

of 150 °C. The solution was kept for three days for effective formation of the complexes in the zeolite supercage. The removal of unexchanged metal complexes and ligands were performed by Soxhlet extraction and back exchange procedures similar to that presented in Section 3.3.4.1.

3.3.4.3. Iron(III), Nickel(II) and Copper(II) N,N′-Disalicylidene-1,2-Phenylenediamine Complex Encapsulated into Zeolite Cage

Encapsulation of N,N′-disalicylidene-1,2-phenylenediamine ligands into the zeolite supercage was carried out employing the ship-in-a-bottle method. About 1 g of the corresponding metal exchanged zeolite, viz. FeY, NiY and CuY was mixed with methanolic solution of 2 mmol salicylaldehyde. The mixture was refluxed under constant stirring for 12 h in an oil bath. Subsequently, the solution was filtered and the solid filtrate was again refluxed for 12 h after adding a methanolic solution of 1 mmol *o*-phenylenediamine. The solution was then filtered and the solid material was kept in an oven at 95 ± 3 °C for 8 h. The removal of unexchanged metal complexes and ligands were performed by Soxhlet extraction and back exchange procedures similar to that presented in Section 3.3.4.1.

3.3.5. Preparation of Surfactant Modified Zeolite

The external cation exchange capacity (ECEC) of NaY was determined using the Ming and Dixon method with minor modification [135]. After complete Na-saturation of exchangeable sites of the zeolite with sodium chloride, the external exchangeable sites of the aluminosilicates were covered exchanged with a surfactants whose molecules could hardly penetrate into the pore of the zeolite. Approximately 50 mL of 0.25 mmol L^{-1}

solution of tetrabutylammonium bromide was added to 1 g of Na-saturated zeolite. The mixture was maintained in a tightly closed flask in a universal shaking incubator for 24 h at 30 °C. The liquid was then decanted into a volumetric flask (250 mL). This procedure was repeated four times. The combined solution was diluted to 250 mL with deionized water. The concentration of sodium in the solution was then determined by AAS. Based on the external cation exchange capacity (ECEC) of the neat zeolite, the 100% and 200% cationic surfactant modified zeolite (CSMZ) were prepared as follows: haxadecyltrimethyl ammonium bromide (HDTMA-Br) was employed for modifying the surface of the zeolite. About 1 g of Na-zeolite and the required amount of HDTMA-Br (HDTMA-Br loading levels 100% and 200% of ECEC of zeolite, which corresponds to 0.0437 g and 0.0874 g of HDTMA-Br g^{-1} zeolite, respectively) were put into 500 mL bottles and agitated in a universal shaker for 48 h. Subsequently, the solution was left for 12 h to allow the solid product to settle; then filtered and washed three times with deionized water. The final CSMZ was dried in an oven at 80 °C for 24 h.

3.4. Preparation of Synthetic and Sampling of Tannery Wastewater

The synthetic wastewater (i.e. acid blue dye, ortho phenyl phenol (OPP), 4-chloro-3-methyl phenol (PCMC) and Cr(VI)) stock solution were prepared in distilled water and diluted as required according to the working concentrations. Tannery wastewater samples were collected from a commercial tannery, Pallavarium common effluent treatment plant (CETP), Chennai, India, after primary treatment of the effluent. The wastewater was stored at 4 °C before analysis and allowed to attain the room temperature just before it was analysed. Solid residues were removed by filtration.

3.5. Catalyst Evaluation

3.5.1. Catalysis Based on Iron(III), Nickel(II) and Copper(II) N,N'-Ethylenebis (Salicylimine) Complex

Treatment of organic pollutants through advanced oxidation process (AOP) by heterogeneous Fenton type methods is based on the presence of hydroxyl radicals (•OH). Direct detection of the hydroxyl radical by an electron paramagnetic resonance (EPR) spectroscopic method is not possible due to the very short half life time of radical species. Hence, an indirect technique viz. spin trapping with 5,5'-dimethyl-1-pyrroline-N-oxide (DMPO) was employed. To verify the generation of hydroxyl radicals (•OH), electron paramagnetic resonance (EPR) spectroscopic analysis was performed in accordance with the procedure suggested by Sanchez et al. [136]. The mixtures of the catalyst (25 mg), distilled water, DMPO and H_2O_2 (10 mM) were added sequentially and stirred together at 5000 rpm for 5 min. The supernatant was introduced into Wilmad-Lab glass aqueous flat cell sample holder for immediate EPR analysis.

To study the catalytic activity of the synthesized catalyst, metal exchanged zeolite, the role of H_2O_2 and the ability of the catalyst to act as an adsorbent of acid blue 113 dye, four independent experiments were carried out (i.e. H_2O_2 with catalyst, metal exchanged zeolite with H_2O_2, catalyst alone and H_2O_2 alone). In each case, the initial dye concentration was maintained at 60 mg L^{-1}. The experiments carried out in the presence of both catalyst and H_2O_2, 0.15 g of catalyst and 0.10 M H_2O_2 were employed. For the experiment in the absence of H_2O_2, 0.15 g of catalyst was employed. The experiments were conducted in dynamic condition at room temperature (29±2 °C) at pH 5.4.

Experiments to investigate the effect of H_2O_2 concentration on decolourization of the azo dye were carried out by keeping the amount of catalyst fixed and varying the concentration of H_2O_2 (i.e. 0.05, 0.10, 0.15, 0.20 and 0.25 M). Similarly, the effect of the amount of catalyst was investigated by varying the amount of catalyst (i.e. 0.05, 0.075, 0.15, 0.225 and 0.3 g) while keeping the concentration of H_2O_2 constant. In addition, the effect of pH on the catalytic decolourization of the dye was investigated at pH 2.0, 4.0, 6.0 and 8.0 at room temperature (29 ± 2 °C). Similarly, the effect of temperature was investigated by carrying out the experiments at 25, 30, 40 and 50 °C at pH 5.4. All experiments were performed in 250 mL conical flask taking 50 mL of 60 mg L^{-1} acid blue 113 dye solution. The percentage decolourization was monitored at various time intervals ranging from 15 to 180 min using a UV-Vis spectrophotometer. The reusability of iron(III), nickel(II) and copper(II) catalysts were studied for ten successive cycles of dye decolourization. After each cycle, the solid catalyst was subsequently filtered from the reaction mixture, washed exhaustively with acetonitrile and ethanol solvent and dried in oven at 100 °C for 3 h.

3.5.2. Catalysis Based on Iron(III) and Nickel(II) (2,2-bipyridine) (1,10-phenanthroline) Complex

The catalytic activities of zeolite encapsulated metal complexes were investigated for the decomposition of H_2O_2 at two different time intervals (1 and 2 h). An amount of 0.15 g of the respective catalysts was added to 0.10 M solution of H_2O_2 and the solution kept on a universal shaking incubator (80 rpm) for 120 min. At the end of each reaction time, the catalyst was filtered and the partly decomposed H_2O_2 was diluted to 250 mL. Then

10 mL of this solution was titrated against standard K_2MnO_4 solution after the addition of 20 mL of 2 M H_2SO_4 and 20 mL distilled water [137].

The oxidation of 2-phenyl phenol (OPP) was carried out in a batch reactor. In a 250 mL conical flask, 50 mL of 25 mg L^{-1} 2-phenyl phenol (OPP) solution was treated with 0.10 M H_2O_2 and 0.15 g of the respective catalyst. The experiments were conducted at room temperature (29 ± 2 °C). The reaction was monitored by taking aliquots of the sample at seven different reactions time (i.e. 10, 20, 40, 60, 80,100 and 120 min). After the sample was taken from the reaction mixture, it was centrifuged and filtered. The absorbance of the filtrate was measured at 287 nm using a UV-Vis spectrophotometer. Reusability of catalysts was studied for three successive cycles for oxidation of OPP.

3.5.3. Catalysis Based on Iron(III), Nickel(II) and Copper(II) N,N'-disalicylidene-1,2-Phenylenediamine Complex

Experiments to investigate the effect of the H_2O_2 concentration on the degradation of PCMC were performed by keeping the amount of catalyst fixed and varying the concentration of H_2O_2 (i.e. 0.025, 0.05, 0.075 and 0.1 M). The effect of amount of catalyst was also investigated by varying the amount of catalyst (i.e. 0.05, 0.075, 0.1 and 0.125 g) while the concentration of the H_2O_2 was kept constant. In addition, to investigate the effect of pH the experiments were performed at pH of 3.0, 5.0, 7.0 and 9.0 at room temperature (29±2 °C). Similarly, the effect of temperature was investigated by carrying out the experiments at 25, 30, 40 and 50 °C, at constant pH (5.3). In all cases the experiments were conducted in 250 mL conical flasks on a universal shaking incubator (80 rpm) taking 50 mL of 0.35 mM PCMC solution in a dynamic condition and the

percentage degradation was monitored at various intervals ranging from 15 to 120 min using high performance liquid chromatography (HPLC). The reuse of iron(III), nickel(II) and copper(II) Salophen catalysts was studied for ten successive cycles of PCMC degradation and after each cycle the solid catalyst was filtered from the reaction mixture, washed exhaustively with acetonitrile and ethanol solvents and dried in oven at 150 °C for 1 h.

The kinetics of adsorption was measured employing the pseudo first order kinetic model. The reaction kinetics was investigated by taking PCMC concentrations of 0.03, 0.07, 0.35, 0.52 and 0.70 mM while maintaining other parameters constant. All experiments were conducted in a conical flask (250 mL) placed on a universal shaking incubator (80 rpm) at room temperature (29 ± 2 °C). The experiments were initiated by adding 0.35 mM of PCMC, a specific amount of H_2O_2 and catalyst to the solution. Samples were withdrawn at given time intervals during the reaction. The samples were filtered through a 0.22 μm filter paper to remove catalyst particles prior to the samples being injected into an HPLC column for analysis. Aliquots of 10 μL were injected into the HPLC column to quantify PCMC. Acetonitrile/water (50:50, v/v) at a flow rate of 1.0 μL/min was used as the mobile phase to elute the samples. The electronic spectrum of the eluting sample was recorded from 200 to 380 nm.

3.6. Adsorption Studies

A 1.0 g portion of surfactant modified zeolite was placed in a 250 mL Erlenmeyer flask containing 100 mL of synthetic wastewater having initial concentration of 100 mg L^{-1} and 25 mg L^{-1} for acid blue dye and Cr(VI), respectively. All samples were filtered

through 0.22 μm filter paper prior to analysis to minimize interference of fine particles in the analysis. The residual acid blue dye concentration was estimated using absorbance values obtained at 562 nm. The concentration of Cr(VI) in an aqueous solution was determined by an indirect colorimetric method. This method is based on the reaction between Cr(VI) and diphenylcarbazide (DPC), which produces a violet red colour. The maximum absorbance was at 540 nm. The Cr(VI) concentration of the sample was estimated using a calibration curve prepared from standard Cr(VI) solutions with concentrations ranging from 0.1 to 1.0 mg L^{-1}. The percentage of removal (R%) and adsorption capacity (q_e) were calculated for each run using the following expressions (Equations. 3.2 and 3.3).

$$\%R = \frac{c_i - c_f}{c_i} \times 100 \qquad (3.2)$$

$$q_e\,(\text{mg g}^{-1}) = \frac{(c_i - c_f)V}{m} \qquad (3.3)$$

where c_i and c_e are the initial and final concentration of dye and Cr(VI) in the solution, respectively. V is the volume of solution (in liters) and m is the mass of adsorbent (in grams) used.

The effect of adsorbent dosage (0.25, 0.5, 1, and 1.5 g), contact time (0.5, 1, 2, 3, 6, 12 and 24 h), initial Cr(VI) concentration (10, 20, 25 and 30 mg L^{-1}), initial acid blue dye concentration (25, 50, 100 and 150 mg L^{-1}), temperature (25, 30, 35 and 40 °C) and pH (3, 5, 7 and 9) were investigated. All the experiments were performed in triplicate. Langmuir and Freundlich isotherms were used for adsorption isotherm

studies. The kinetics of adsorption was analysed by applying the pseudo first order and pseudo-second order kinetic model. Both kinetic and isotherm experiments were investigated by taking 25, 50, 100 and 150 mg L^{-1} of acid blue dye and 20, 30, 40 and 50 mg L^{-1} of Cr(VI) while maintaining other parameters constant.

3.7. Computational Studies on Metal Complex Encapsulated into Zeolite Y

Density functional theory (DFT) calculations were performed using $Dmol^3$ program with generalized gradient approximation (GGA) and the Perdew-Burke-Ernzerhof (PBE) exchange functional and double numeric (DN) basis set. In the self-consistent field calculations, the electronic density convergence threshold was set at 1×10^{-6}. Geometric optimization was performed with convergence thresholds of 10^{-5} Ha for the energy, 2×10^{-3} Ha $Å^{-1}$ for the force, and 10^{-3} Å for the atomic displacements. All electronic structure calculations were performed for neat metal complex and zeolite Y encapsulated metal complexes. Zeolite provides well-defined rigid and stable framework with cavities of various sizes and shapes, so that the encapsulation of transition metal complexes in these cavities allows the variation of their environment in a controlled manner. The supercage of zeolite Y was fixed. Its diameter was about 13.0 Å and its pore openings approximately 7.4 Å. Initially, the zeolite clusters were generated by taking 48 tetrahedral units (48T) of faujasite structure around the supercage and saturating them with hydrogen atoms. The framework of Si and O atoms of the clusters were held fixed at their crystallographic positions and all the terminal H atoms were optimized. The gas phase optimized complexes were encapsulated inside the supercage and the calculation was repeated. Based on the Koopmans theorem, global hardness (η) value was calculated using

Equation 3.4 as follows.

$$\eta = \frac{E_{\text{LUMO}} - E_{\text{HOMO}}}{2} \tag{3.4}$$

Where E_{LUMO} and E_{HOMO} represent the energy of the lowest unoccupied molecular orbital and highest occupied molecular orbital, respectively. The global softness(s) was calculated according to Parr et al. as follows (Eq. 3.5) [138].

$$s = \frac{1}{2\eta} \tag{3.5}$$

4. Results and Discussions

4.1. Iron(III), Nickel(II) and Copper(II) N,N′-Ethylenebis(salicylimine) Complex Encapsulated into Zeolite Cage

4.1.1. Characterization of the Catalyst

4.1.1.1. Background

The formation of the N,N′-ethylenebis(salicylimine) schiff base ligand was investigated by ^{1}H NMR and FT-IR. As shown in Figure 7.1 and 7.2 (Appendices), ^{1}H NMR (500 MHz, DMSO-d_6) of the Schiff base ligand shows signals at δ (ppm): 3.93 (s, 4H, 2 × CH_2), 6.85-6.99 (m, 4H, arom), 7.30-7.34 (m, 2H, arom), 7.42-7.44 (d, 2H, arom), 8.59 (s, 2H, 2 × N=C<u>H</u>) and 13.39 (s, H, 2 × -O<u>H</u>). The ligand shows characteristic IR bands at 3434 cm^{-1} (-OH) and 1634 cm^{-1} (-CH=N-) [14]. Thus, based on the proton NMR and FT-IR data the successful synthesis of salen ligand is confirmed.

Ship-in-a-bottle method was adopted to encapsulate Fe(III), Ni(II) and Cu(II) complexes of salen ligand into NaY zeolite. The colour of the catalysts was observed to be brick red, light yellow and green blue for iron(III), nickel(II) and copper(II) catalysts, respectively. Even after purification, the colour of the catalysts did not change indicating that the complexation has occurred in the cavities and the resulting complexes were too large to diffuse out of zeolite through the channels.

4.1.1.2. Structural, Morphological and Textural Properties of Materials

Figure 4.1 shows X-ray diffraction (XRD) patterns of neat zeolite and iron(III), nickel(II) and copper(II) catalysts. Powder X-ray diffraction pattern of zeolite encapsulated respective metal complexes were similar to that observed for neat zeolite, though insignificant change in the intensity of the bands was noticed. This indicates that the framework of the zeolite did not undergo any major structural change during encapsulation. No new peaks were observed in the XRD pattern of zeolite encapsulated metal complexes (Figure 4.1) suggesting that the concentration of metal complexes in the zeolite cavity is relatively low.

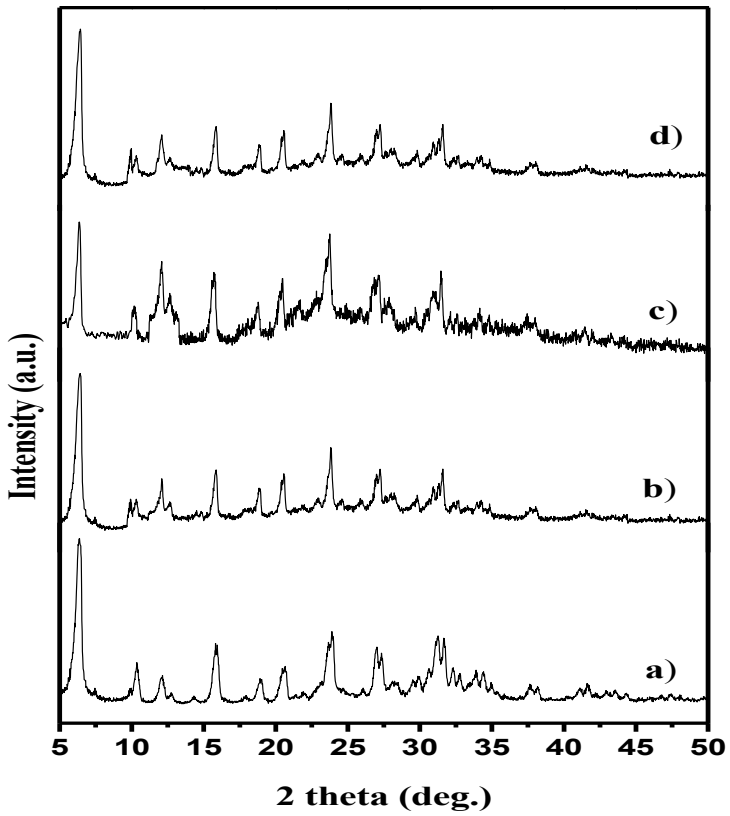

Figure 4.1 X-ray powder diffraction patterns of **a**) neat zeolite **b**) iron salen **c**) nickel salen and **d**) copper salen catalyst

N_2 sorption experiments are carried to investigate the surface area and pore volume of catalyst and results are depicted in Table 4.1. BET surface area of the zeolite encapsulated metal complexes was reduced from 526 $m^2 g^{-1}$ (neat zeolite Y) to 285, 391, 221 $m^2 g^{-1}$ for iron(III), nickel(II) and copper(II) catalyst, respectively. Such significant decrease in BET surface area is indicative of the fact that the respective metal complex is encapsulated within the zeolite Y supercages or blocking of the cage. Likewise, the pore volume decreased from 0.23 $cm^3 g^{-1}$ (neat zeolite Y) to 0.10, 0.11, 0.08 $cm^3 g^{-1}$ for iron(III), nickel(II) and copper(II) catalyst, respectively. Since the zeolite crystallinity is retained, the observed lowering of surface area and pore volume is an indication of the presence of respective metal complexes in the zeolite supercage. Among the three catalysts copper (II) and iron(III) catalyst are lower surface area and pore volume than nickel(II) catalyst, due to higher concentration of respective metal complexes in the zeolite supercage. In the literature similar reduction of surface area and pore volume was reported for zeolite encapsulated metal complex [139,140].

Table 4.1 BET surface area and pore volume of neat zeolite Y and catalyst

Sample	S_{BET} ($m^2 g^{-1}$)	Pore volume ($cm^3 g^{-1}$)
Neat zeolite Y	526	0.23
Iron salen catalyst	285	0.10
Nickel salen catalyst	391	0.11
Copper salen catalyst	221	0.08

4.1.1.3. Spectroscopic Characterization

The FT-IR spectra of zeolite encapsulated Fe(III), Ni(II)and Cu(II) complexes are provided in Figure 4.2. The FT-IR spectra of salen ligand showed intense bands at around 2900 and 1600 cm^{-1} due to CH_2- and CH=N- group stretching vibrations. IR spectra of all

the catalysts were dominated by the IR bands of zeolite due to the low concentration of respective metal complexes in the zeolite cage [141-143]. However, in the case of copper(II) catalyst there was an intense IR bands around 1300-1600 cm^{-1} which is attributed to the presence of higher concentration of salen complexes in the supercage of zeolite that was not the case with the other two catalysts. In the IR spectrum of neat zeolite the broad bands in the region 3488 and 1646 cm^{-1} due to stretching and bending modes of -O-H groups of water molecules in zeolite cavities [144].

The IR spectra of neat zeolite also has a band at 978 cm^{-1}, which could be attributed to the stretching vibrations of $(Si/Al)O_4$ and the bands that appear in the region of 788, 752, 674, 561 and 459 cm^{-1} are the result of several vibrations of -Si-O and -Al-O bonds in the SiO_4 and AlO_4 tetrahedral framework [143-145]. The IR spectral bands of neat zeolite was also observed in the spectrum of zeolite encapsulated metal complexes, which further suggests that, the zeolite framework has remained unchanged upon encapsulation of metal complexes. The band observed at around 1600 cm^{-1} in the IR spectra of free salen ligand, which is characteristic of azomethine groups (-CH=N-), is shifted to around 1550 cm^{-1} for each catalyst indicating that the ligand is coordinated to the respective metal ions through azomethine nitrogen. Likewise, the catalysts show stretching vibrations of methylene groups ($-CH_2-$) at 2923 cm^{-1}, 2935 cm^{-1} and 2923 cm^{-1} for iron(III), nickel(II) and copper(II) catalyst, respectively. IR bands are also observed at 1397 and 1464 cm^{-1} for iron(III), 1397 and 1476 cm^{-1} for nickel(II) and 1329 and 1453 cm^{-1} for copper(II) catalyst, which can be attributed to the bending vibrations of methylene groups.

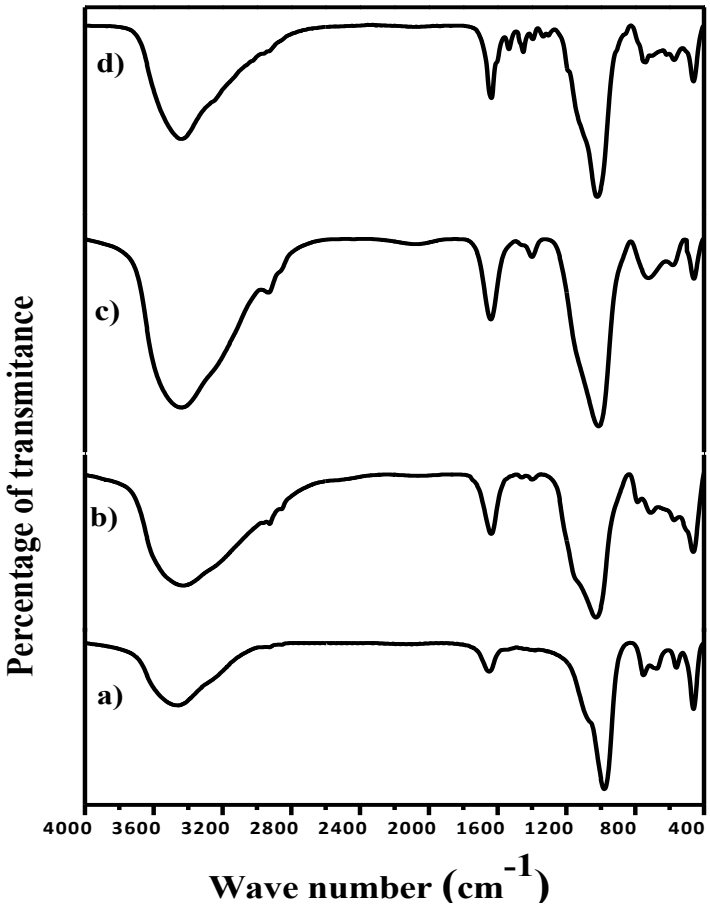

Figure 4.2 FT-IR spectrums of **a**) neat zeolite **b**) iron salen **c**) nickel salen and **d**) copper salen catalyst

Figure 4.3 a and b present EPR spectra of neat iron(III) salen complexes and zeolite encapsulated iron(III) salen complexes obtained at room temperature. The EPR spectrum of iron(III) catalyst has broad signals at *g* values of 2.037 and 4.356; whereas iron(III) salen complex has only one and comparatively sharp signal at *g* value of 2.068. These differences in *g* value and broadness of EPR signal are due to the existence of monomeric iron(III) complexes in supercages of the zeolite [146]. Moreover, the broad EPR signal observed in zeolite encapsulated iron(III) complexes indicate the presence of low-spin iron(III) configurations of axially distorted octahedral complex in the zeolite cage.

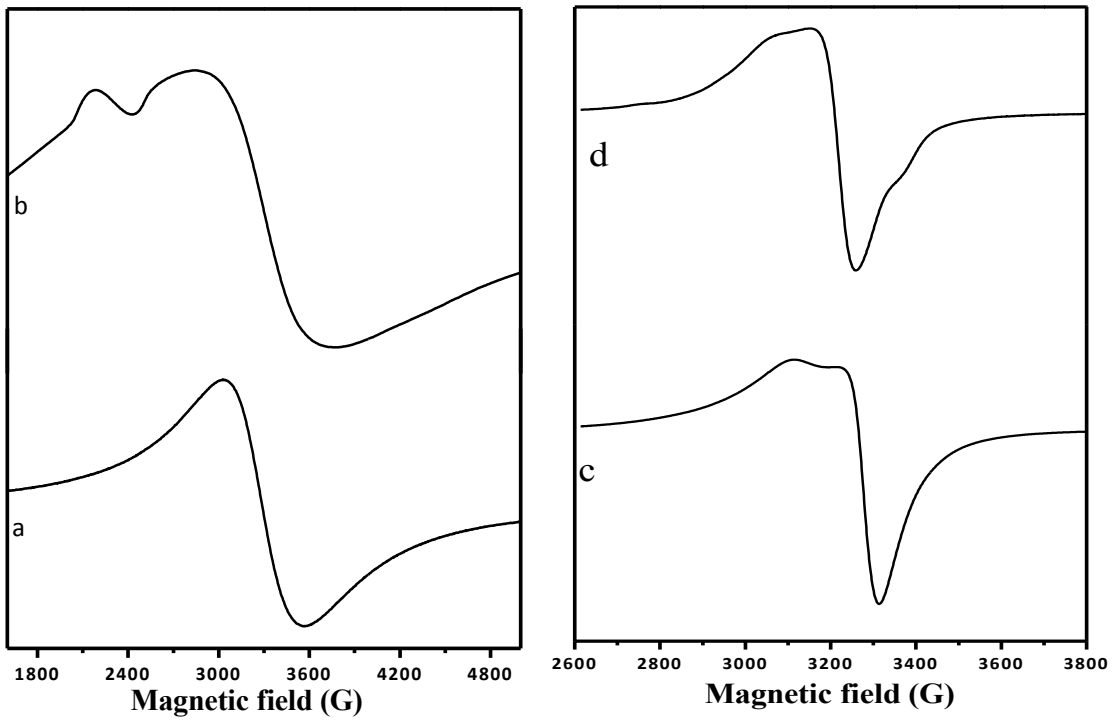

Figure 4.3 Powder EPR spectra of **a**) iron salen complex **b**) iron salen catalyst **c**) copper salen complex and **d**) copper salen catalyst

Figure 4.3 c and d represents the powder EPR spectra of neat copper(II) and zeolite encapsulated copper(II) complex. The difference in the *g* values between the neat complex ($g_{\parallel}$= 2.201 and $g_{\perp}$= 2.093) and zeolite encapsulated copper(II) salen complex ($g_{\parallel}$ = 2.156 and $g_{\perp}$ = 2.034) gives a clear indication that the copper salen complex in the zeolite cage exists in slightly different symmetry than that of neat copper(II) complex. This is due to the encapsulation effect of copper(II) salen into zeolite supercage. Also, from the spectra that both the complex have $g_{\parallel} > g_{\perp} > 2.0023$ indicating that the unpaired electron in copper(II) complex occupies the d_{x2-y2} orbital, which is the characteristic for a tetragonally elongated system [147].

4.1.1.4. Thermogravimetric and Elemental Analysis

In order to investigate the thermal stability of the synthesised catalysts their thermogravimetric analysis (TGA) was carried out and Figure 4.4a and b illustrated TGA thermogram of neat metal complexes, neat zeolite and zeolite encapsulated metal complex. It can be seen from the Figure 4.4 b that, neat zeolite has a single step weight loss due to desorption of free water molecules in the zeolite cage. Unlike the neat zeolite, the zeolite encapsulated iron(III), nickel(II) and copper(II) complexes exhibit two stage weight loss. The first weight loss observed at 25-250 °C can be attributed to desorption of free water and the second weight loss observed at 250-800 °C is due to oxidative removal of organic part of the respective metal catalyst in the zeolite. The total loss of organic part in the case of iron(III), nickel(II) and copper(II) catalyst is about 10.4, 9.3 and 10.7%, respectively. The comparison of TGA pattern of respective neat metal salen complexes with that of the encapsulated one shows that the metal salen complexes become more thermally stable once they were embedded into the highly thermal resistant aluminosilicate frame work of zeolite Y. This also indicates that on encapsulation the thermal stability of the complexes is greatly enhanced and hence can be thermally treated without significant decomposition.

Table 4.2 presents the analytical data of the respective metal catalysts, neat zeolite and neat metal complex. The Si/Al ratio is 2.5, 2.5, 2.5 and 2.5 for the neat zeolite, iron(III), nickel(II) and copper(II) catalyst, respectively, indicating the absence of dealumination during encapsulation of respective metal salen complexes into zeolite supercage. The metal and CHN values indicate that the ligand to metal molar ratio is around 1:1 for each

metal salen complex inside the zeolite cavity. However, trace amount of free metal ions were present in the zeolite super cavities even after back exchange processes. The presence of trace amount of non-exchangeable free metal ions may be attributed to the shielding by the guest molecules (metal salen complex) or some of the sites in the zeolite lattice might be blocked by the encapsulated metal salen complexes for NaCl solution to access the free metal ion in back exchanged process [139]. It has been reported that traces of uncomplexed metal ions do not significantly alter the behaviour of the zeolite encapsulated metal complexes [140,148].

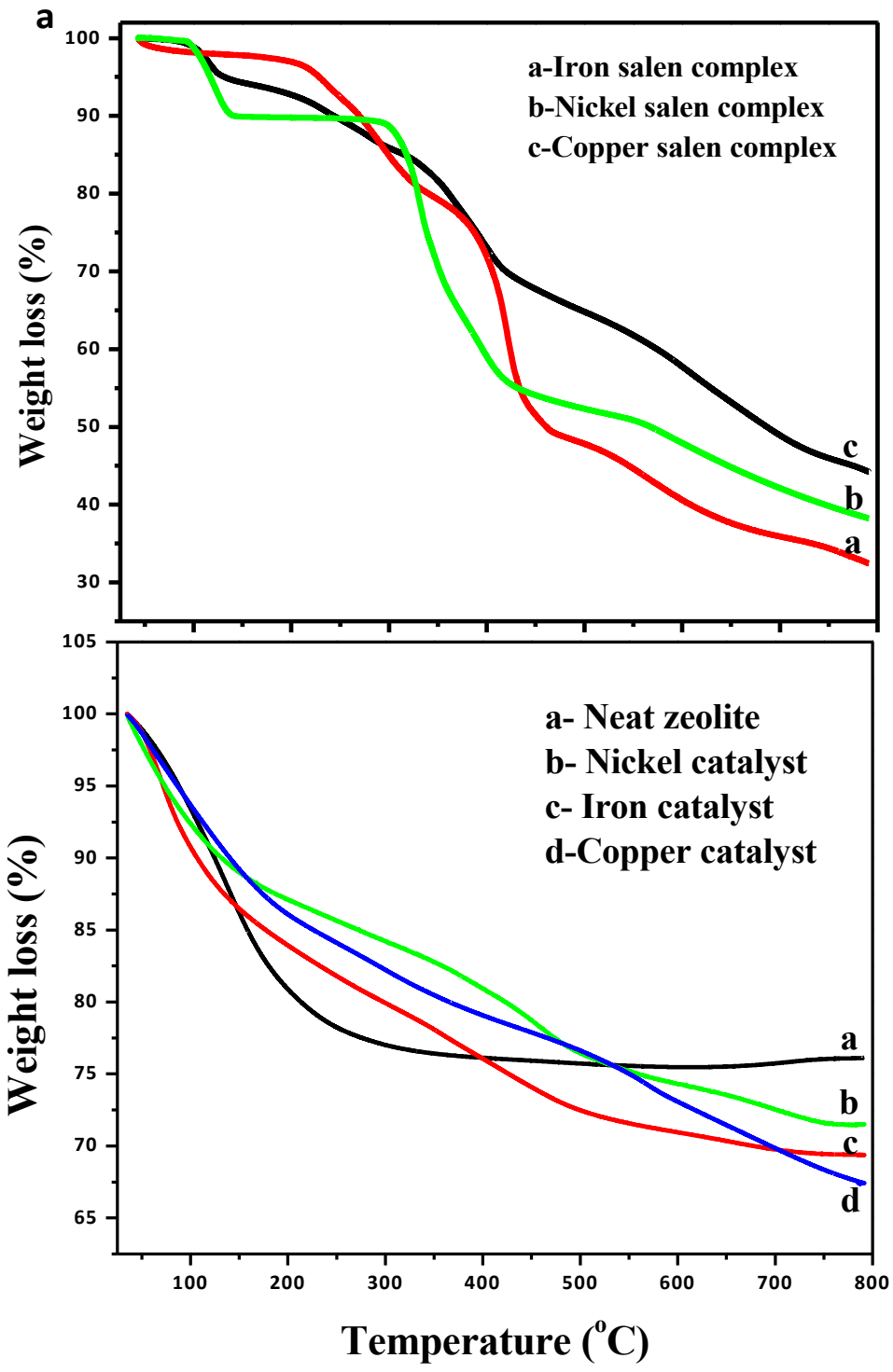

Figure 4.4 TGA profiles of **a**) neat metal complex **b**) neat zeolite and metal catalyst

Table 4.2 Chemical composition (wt. %) of neat zeolite, neat metal complexes and metal catalyst

Sample	Metal (%)	Si (%)	Al (%)	Si/Al	Na (%)	C (%)	N (%)	H (%)	C/N
Fe-salen complex	17.09 (17.34)[a]	-	-	-	-	59.47 (59.65)[a]	8.63 (8.70)[a]	4.35 (4.38)[a]	6.89 (6.87)[a]
Ni-salen complex	17.95 (18.06)[a]	-	-	-	-	58.89 (59.13)[a]	8.53 (8.62)[a]	4.31 (4.34)[a]	6.90 (6.86)[a]
Cu-salen complex	18.97 (19.27)[a]	-	-	-	-	58.26 (58.18)[a]	8.43 (8.49)[a]	4.21 (4.28)[a]	6.91 (6.85)[a]
Neat zeolite	-	20.64	8.12	2.5	7.43	-	-	-	-
Fe- catalyst	2.03	20.18	7.95	2.5	5.21	6.48	0.94	0.76	6.89
Ni-catalyst	1.97	20.21	8.04	2.5	5.07	5.96	0.87	0.55	6.85
Cu-catalyst	2.36	20.09	7.97	2.5	5.58	6.74	1.01	0.69	6.67

[a] theoretical CHN value

4.1.2. Catalyst Evaluation

4.1.2.1. Role of the Catalyst

Figure 4.5 the EPR spectrum exhibits a four-line signal, with a peak ratio of 1:2:2:1 confirming the presence of free radicals. This conclusively proves that the synthesized zeolite encapsulated metal complex can act as a catalyst to activate hydrogen peroxide molecule leading to the formation of hydroxyl radical (•OH) [149].

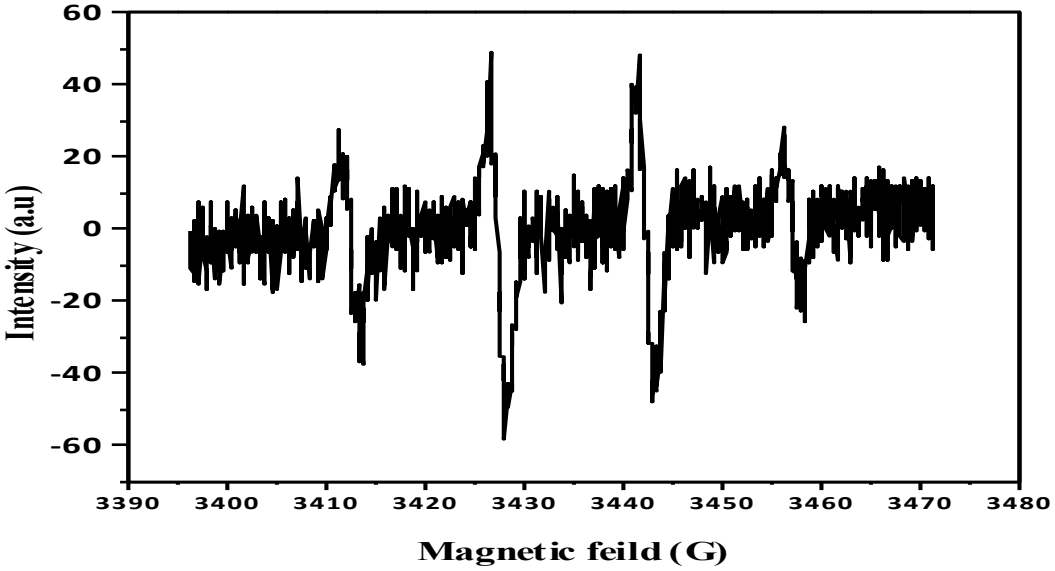

Figure 4.5 EPR spectrum for DMPO-•OH radical

The result of the experimental results is conducted to evaluate the catalytic activity of synthesized catalyst revealed that the concentration of dye left in the solution was 14, 21 and 15 mg L^{-1} in the presence of H_2O_2 and iron(III), nickel(II) and copper(II) catalyst, respectively. The residual concentration of acid blue dye treated with metal exchanged zeolite with H_2O_2 was 35, 40, 37 for iron(III), nickel(II) and copper(II) metal exchanged zeolite, respectively. The residual concentration of dye in the reaction carried out only using catalyst was 52, 49 and 54 mg L^{-1} for iron(III), nickel(II) and copper(II) catalyst, respectively. However, the residual amount of dye left in solution in the experiments conducted with only H_2O_2 was 41 mg L^{-1} after 120 min reaction time. This difference in residual concentration of dye clearly indicates the importance of the catalyst in the degradation of the dye molecule. Moreover, it can be concluded that in these experiments the adsorption of dye molecules does not contribute significantly to the overall decolourization and mineralization of organic pollutants when using zeolite based

heterogeneous catalyst. This may be due to the hydrophilic properties of the zeolite surface. Moreover, metal exchanged zeolite has little oxidation abilities but in this study their contribution was insignificant because of metal ion forms a complex after encapsulation process.

4.1.2.2. Effect of Hydrogen Peroxide Concentration and Catalyst Amount

The effect of H_2O_2 concentration (varying from 0.05 to 0.25 M) on the oxidation of acid blue dye, while maintaining other parameters constant can be seen in Figure 4.6. The degradation of dyes increased from 60 to 82.9% for iron(III) catalyst, 60.2 to 76.5% for nickel(II) catalyst and 64 to 83.3% for copper(II) catalyst with increase in concentration of H_2O_2 from 0.05 M to 0.25 M. This significant improvement in decolourization of the dye at higher concentration of H_2O_2 can be attributed to the increased amount of •OH radical obtained from decomposition of H_2O_2 as its concentration increased.

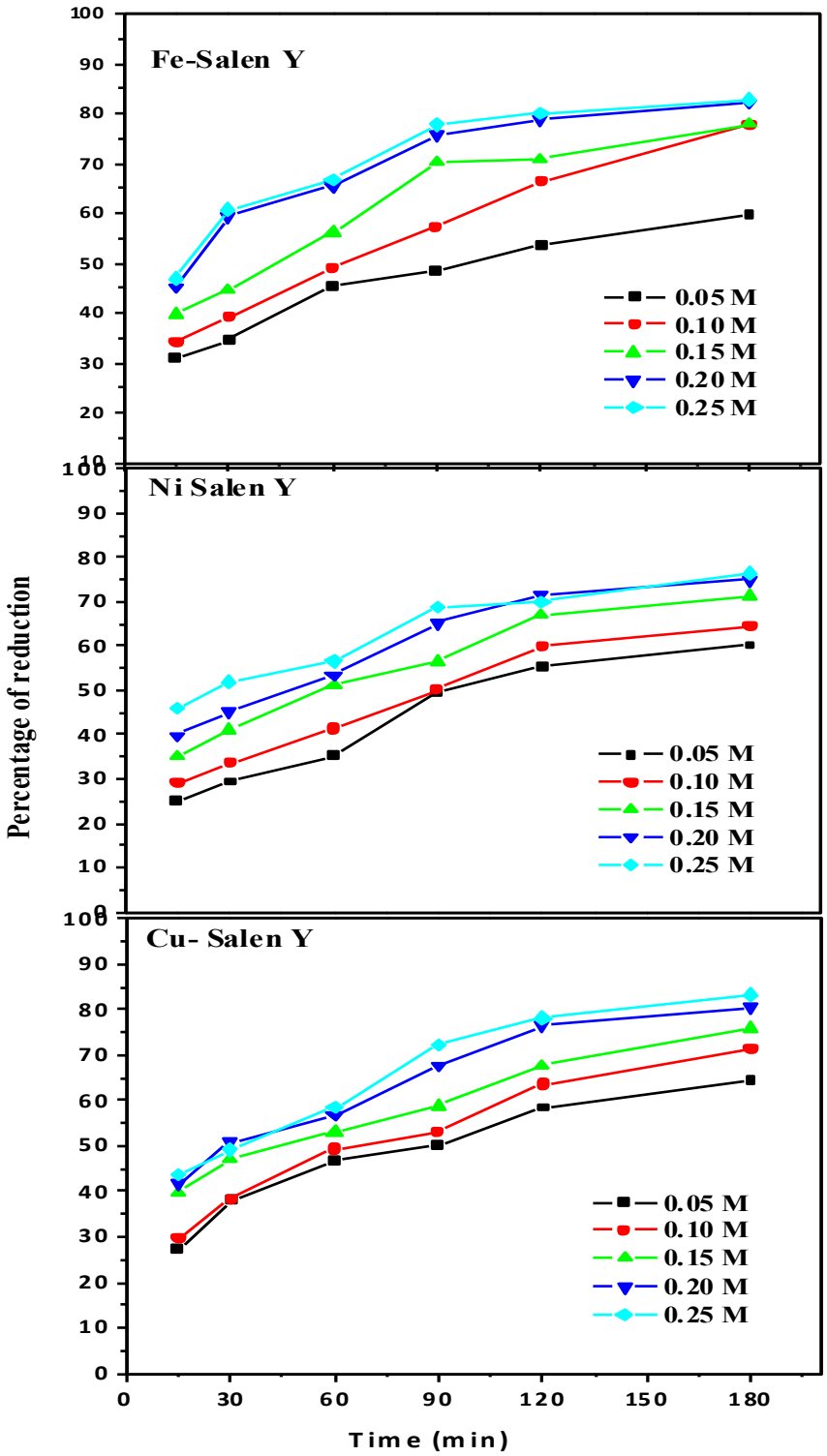

Figure 4.6 Effect of H_2O_2 concentration on degradation of dye by iron, nickel and copper salen catalyst: [dye] = 60 mg L^{-1}, [catalyst] = 0.15 g; temperature = 29±2 °C; pH = 5.4; period = 180 min

Also, it can be observed from Figure 4.6 that the improvement in decolourization was not significant for higher concentrations of H_2O_2 for all catalysts. This can be due to the fact that at higher concentrations, there is a possibility of formation of hydroperoxyl radical (Eq. 4.1) which has lower oxidation potential than the hydroxyl radical [150-152].

$$H_2O_2 + \bullet OH \rightarrow H_2O + \bullet OOH \qquad (4.1)$$

The EPR spectrum (Figure 4.7) obtained for higher concentration of H_2O_2 clearly proves the shift of the equilibrium to hydroperoxyl radical [136].

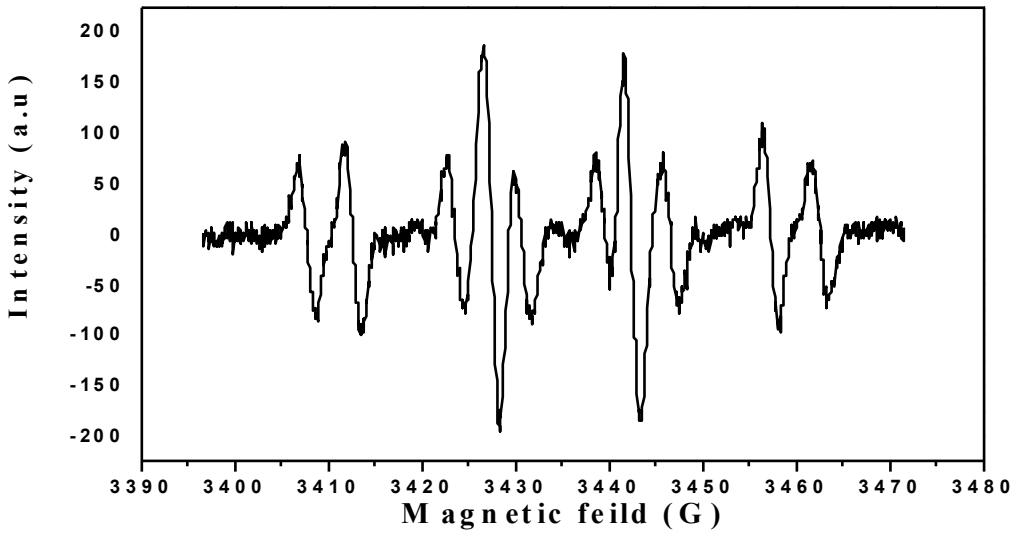

Figure 4.7 EPR spectrum of DMPO-•OOH radical

Figure 4.8 represents the effect of catalyst amount on degradation of acid blue dye with the amount of catalyst varying from 0.05 to 0.3 g while keeping all other reaction parameters constant. As shown in Figure 4.8, decolourization of the acid blue dye increased as the amount of catalyst was increased to a certain catalyst load, after which it becomes less efficient. An increase in the amount of catalyst dosed provides more sites on the catalyst surface for accelerating the decomposition of H_2O_2, which in turn

increased the number of hydroxyl radical (•OH) significantly. However, at higher catalyst dosage aggregation of the catalyst molecules cannot be ruled out, some thing which may cause a decrease in the number of the surface active sites available [61, 62]. This effect is clearly observed in the Figure 4.8. The removal of dye at 0.225 and 0.3 g of catalyst is not significantly higher than 0.15 g of catalyst for all catalysts. Hence, 0.15 g was taken as optimum amount of catalyst for further experiments. Moreover, to investigate the degree of mineralization (dye degradation) during catalytic oxidation process, reduction of total organic carbon (TOC) was assessed while maintaining 0.15 g of catalyst amount and 0.10 M H_2O_2 in dynamic condition. It was found that TOC value of azo dyes decreased by 71%, 58% and 67% in the presence of iron(III), nickel(II) and copper(II) catalysts, respectively. It can be seen that the extent of reduction in TOC value was less when compared to the percentage decolourization (Figure 4.8) of azo dyes during the catalytic dye degradation process. The observed lower reduction in TOC value compared to the efficiency of decolourization may be attributed to the higher stability of the aromatic ring structures in the dye molecules as compared to azo bond (-N=N-) and/or relatively high stability of intermediate products formed during the catalytic dye degradation process. Similar trends in the reduction of TOC and decolourization of azo dyes have also been reported elsewhere [153,154].

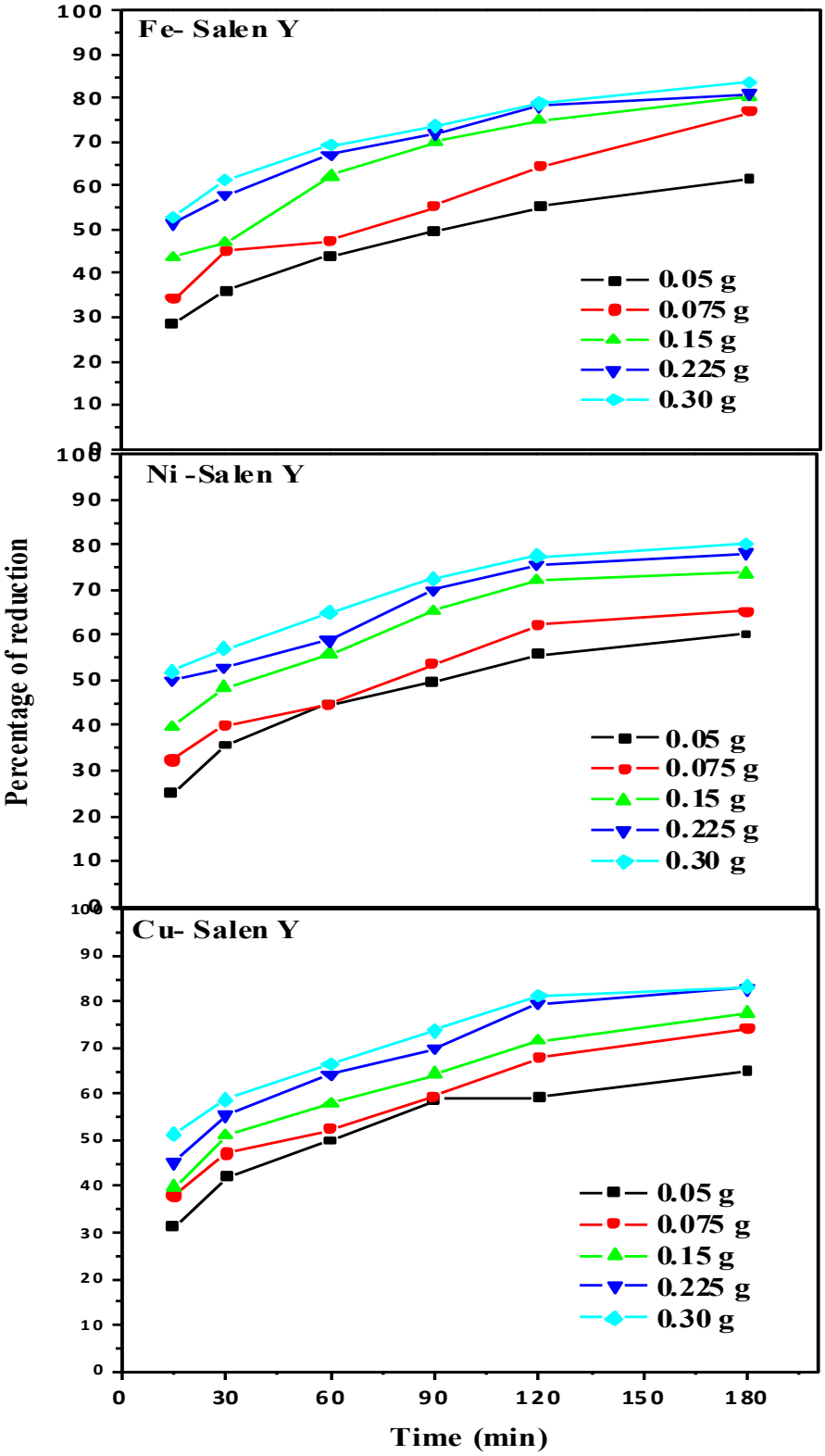

Figure 4.8 Effect of catalyst amount on degradation of dye by iron, nickel and copper salen catalyst: [dye] = 60 mg L^{-1}, [H_2O_2] = 0.1 M; temperature =29±2 °C; pH = 5.4; period = 180 min

4.1.2.3. Effect of pH and Temperature

The effect of pH on degradation of acid blue dyes was investigated by selecting four pH values (2, 4, 6 and 8). The effect of pH and temperature on the decolourization of acid dye is summarised in Table 4.3.

Table 4.3 The effect of pH and temperature variation in reduction of dye concentration

pH	Percentage of reduction			Temperature (°C)	Percentage of reduction		
	Fe-catalyst	Ni-catalyst	Cu-catalyst		Fe-catalyst	Ni-catalyst	Cu-catalyst
2	99.8	86.5	96.2	25	77.9	64.8	72.1
4	90.8	79.7	79.7	30	79.1	74.7	80.5
6	78.7	74.5	77.9	40	90.4	80.3	83.3
8	71.9	64.2	72.7	50	93.2	83.1	89.6

- The pH variation experiments were conducted at 29±2 °C and the temperature variation experiments were conducted at a pH of 5.4

It can be deduced from Table 4.3 that the optimum solution pH value for efficient decolourization of acid dye was 2. The maximum decolourization achieved was 99, 86 and 96% within 180 min reaction times for iron(III), nickel(II) and copper(II) catalysts, respectively. The results indicate that pH of the solution has significant influence on the oxidation of dyes. This is due to the fact that variation of pH has direct effect on the mechanism and rate of production of hydroxyl radicals. Earlier studies on heterogeneous Fenton type advanced oxidation systems showed that a lower pH is favoured the maximum removal of dyes [61,155]. The reason for this can be that many transition metal complexes and hydroxyl radicals have lower oxidation potential at higher pH values [156].

The influence of reaction temperature on the degradation efficiency of acid blue dye was also investigated. The reaction was carried out at temperatures 25, 30, 40 and 50 °C. The result is provided in Table 4.3. It can be observed from the Table that raising the temperature had a positive impact on the degradation of dyes. The decolourization efficiency within 180 min reaction time increased from 77 to 93% for iron (III), 64 to 83% for nickel (II) and 72 to 89% for copper(II) catalyst, when the temperature increased from 25 to 50 °C. This is due to the fact that higher temperature favouring the forward reaction between H_2O_2 and the catalyst, thus increasing the rate for generation of hydroxyl radical. The better catalytic performance exhibited by the iron(III) catalyst than copper(II) and nickel(II) based catalyst may be attributed to higher oxidizing capability of the iron catalyst as compared to that of copper and nickel catalysts. However, at higher pH values the catalytic activity of Cu(II) catalyst is marginally better than that of the Fe(III) catalyst. This is due to the Fe(III)/Fe(II) oxidation potential being generally higher at lower pH.

4.1.2.4. Reusability and the Possible Deactivation Mechanism of Catalyst

Reusability is one of the major requirements for heterogeneous catalyst and thus repeated experiments were carried out in order to investigate the reusability of catalyst for degradation of acid blue dyes. The efficiency of the catalyst for ten successive reuses is presented in Table 4.4. The iron(III), nickel(II) and copper(II) catalyst retain their catalytic efficiency to 85.0, 81.2 and 89.6% respectively as compared to the fresh catalyst. Hence, it is clear that the loss in catalytic efficiency is not significant and thus the catalysts may be used successively for many cycles.

Table 4.4 Reusability of the catalyst

	Percentage of reduction		
	Fe- catalyst	Ni- catalyst	Cu- catalyst
Fresh catalyst	77.8	65.0	74.0
1st reuse	75.6	63.6	72.8
2nd reuse	73.0	62.8	72.0
3rd reuse	71.8	61.8	70.8
4th reuse	70.6	60.4	70.2
5th reuse	69.3	58.8	68.6
6th reuse	69.1	58.3	66.7
7th reuse	68.4	56.9	65.5
8th reuse	67.8	55.5	64.7
9th reuse	67.5	54.3	62.8
10th reuse	66.1	52.8	66.3

Though the loss in catalytic efficiency was minor, effort was made to investigate the mechanism of catalyst deactivation. To propose the possible deactivation mechanism, the metal content and BET surface area was determined for the last reused catalyst. The metal content (wt.%) of reused iron(III), nickel(II) and copper(II) catalyst was 2.00, 1.92 and 2.29% respectively, which is still comparable to the values observed in the case of the respective fresh catalyst (Table 4.1). Therefore, leaching of the metal ion from the catalyst may not be considered as the major cause for the deactivation of the catalyst after repeated reuse. It has also been reported in the literature that no significant leaching is observed when the complex is successfully confined exclusively in the zeolite pores [140]. On the other hand, the BET surface area of the sample was found to change

considerably after successive reuse of the catalyst. After ten successive reuse of the catalyst, the BET surface area decreased from 285 to 261 $m^2 g^{-1}$, 391 to 374 $m^2 g^{-1}$ and 221 to 209 $m^2 g^{-1}$ for iron(III), nickel(II) and copper(II) catalyst, respectively as compared to respective fresh catalyst. Hence, the most probable reason for the deactivation of the catalyst observed is the reduction in the surface area of the catalyst due to masking or pore blockage, caused by the physical deposit of substances on the outer surface of the catalyst in the zeolite cage [61, 62].

4.2. Iron(III) and Nickel(II) (2,2-bipyridine) (1,10-phenanthroline) Complex Encapsulated into Zeolite Cage

4.2.1. Characterization of the Catalyst

4.2.1.1. Background

1:1 molar ratio of metal ion to ligand was used in the synthesis of the metal complex. 1,10-phenanthroline has high affinity for metal ions and possesses π-acceptor capability. In the first step of synthesis of metal complex it forms simple metal-phen intermediate complexes. The final iron(III) or nickel(II) bipy-phen mixed liganded complexes are then formed in the second step by addition of 2,2'-bipyridine ligand to the intermediate metal phenanthroline complex. To verify the formation of mixed ligand metal complexes the synthesized complexes were analysed using ESI-MS. The ESI-MS spectrum of the Fe(III) complex and Ni(II) complexes are shown in Figure 7.3 and 7.4 (Appendices). The Fe(III) complex shows a base peak at *m*/*z* 461.408 which can be attributed to the cationic complex $[Fe(bipy)(phen)Cl_2]^+$. Similarly the ESI-MS spectrum of the Ni(II) complex shows base peak at *m*/*z* 429.435 which can be attributed to the cationic species $[Ni(bipy)(phen)Cl]^+$.

The zeolite Y structure contains uniform sized pores and cages. The supercages have internal diameter of 13.0 Å and are connected to each other by tunnels or "windows" of 7.4 Å diameters [51, 157]. Evidently, only active components with lesser size and shape can be incorporated into this cage. The diameters of $[Fe(bipy)(phen)Cl_2]^+$ and $[Ni(bipy)(phen)Cl]^+$, however, are too large for the ligands to effectively pass through the free aperture of the zeolite supercage, but are sufficiently small to be confined in the larger cavities once they have formed a complex in the cage. On the other hand, their

easily flexibility nature of 2,2′-bipyridine and 1,10-phenanthroline ligand means they can diffuse into the zeolite and form complexes with previously exchanged metal ions inside the supercage using the *in-situ* method [64,65].

4.1.1.2. Structural, Morphological and Textural Properties of Materials

Figure 4.9 shows the X-ray powder difractograms of neat zeolite Y, iron(III) and nickel(II) catalyst. The diffraction pattern indicates that a well crystalline zeolite encapsulated catalysts are formed. Diffraction patterns of both zeolite encapsulated metal complexes are similar to that observed for the neat zeolite. The similarity of XRD pattern of all the samples suggests that the crystallinity of zeolite Y is preserved during encapsulation of respective metal complexes into zeolite cage. However, as shown in the Figure 4.9, a slight change in the peak intensity is observed around $2\theta < 20^{o}$, i.e. I_{220} at $2\theta = 10°$ and I_{311} at 12°, for both neat zeolite and metal catalyst [158]. In addition, the relative peak intensity for zeolite Y is $I_{220} > I_{311}$ whereas for zeolite encapsulated metal complexes it is $I_{311} > I_{220}$. The change in relative intensities may be associated with redistribution of randomly coordinated metal cations in zeolite Y at sites II and I. Similar observation have been reported before [158, 159] and the above observation may therefore be interpreted as evidence for the successful encapsulation of $[Fe(bipy)(phen)Cl_2]^+$ and $[Ni(bipy)(phen)Cl]^+$ complex within the supercage of zeolite Y.

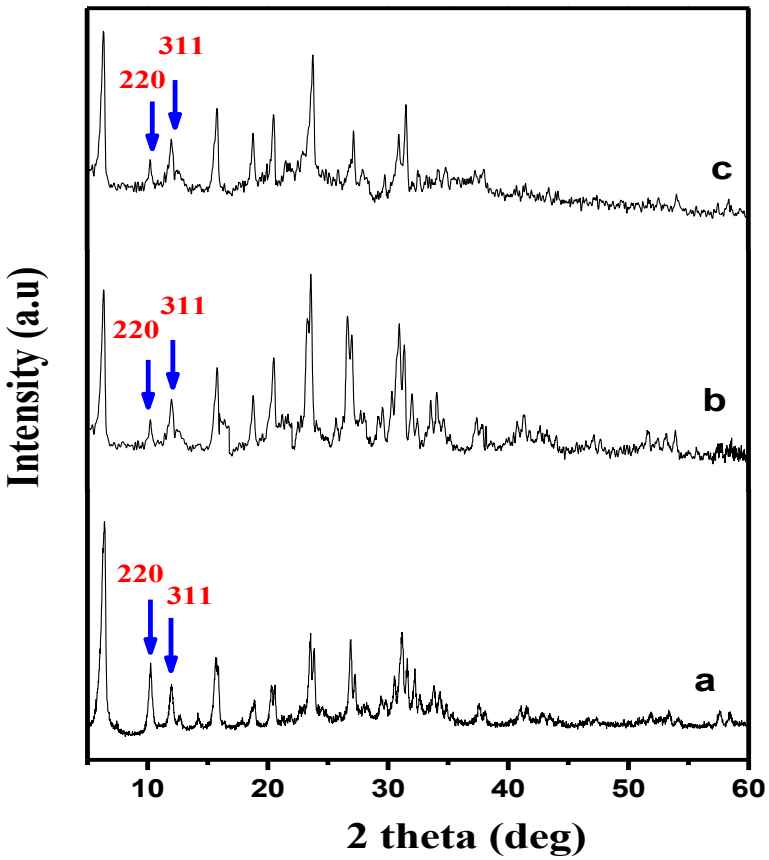

Figure 4.9 XRD pattern of **a**) NaY **b**) $[Fe(bipy)(phen)Cl_2]^+$-Y **c**)$[Ni(bipy)(phen)Cl]^+$-Y

After encapsulation of the respective metal complexes, the solid catalyst was purified by extensive Soxhlet extraction with organic solvents to remove unreacted ligand and/or surface adsorbed complexes. The SEM morphology of the metal catalysts before and after Soxhlet extraction is depicted in Figure 4.10 and 4.11. In the SEM image (Figure 4.10a and Figure 4.11c) taken before purification there is no defined particle boundaries indicating that the metal complexes are deposited on the external surface of zeolite. However, the SEM image (Figure 4.10b and Figure 4.11d) of the all catalysts after solvent extraction shows particle boundaries, indicating that surface adsorbed complexes are not present in this case. This suggests that Soxhlet extraction procedure

effectively remove extraneous complexes, leading to well define encapsulation in the zeolite cavity. Also, it can be concluded that encapsulation of respective metal complexes into the zeolite supercage did not significantly affect the crystal structure of the parent zeolite

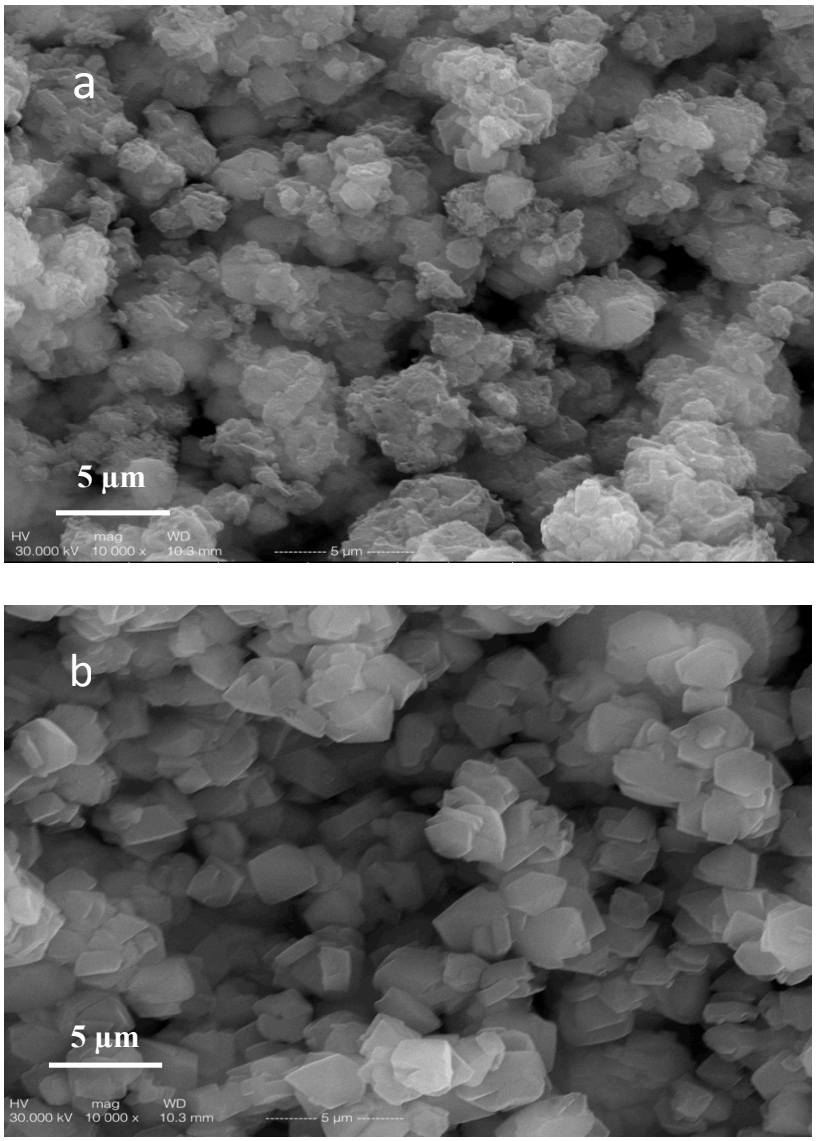

Figure 4.10 SEM morphology of **a**) $[Fe(bipy)(phen)Cl_2]^+$-Y before

b) $[Fe(bipy)(phen)Cl_2]^+$-Y after Soxhlet extraction

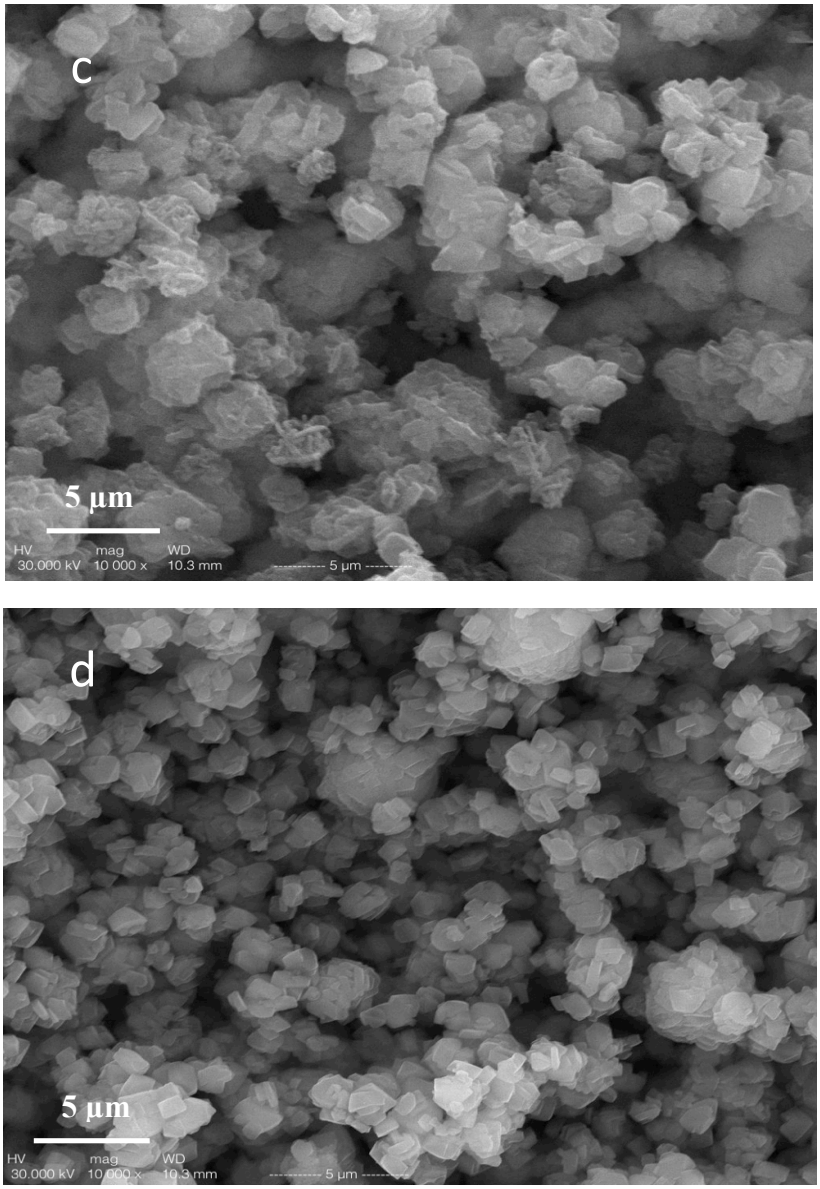

Figure 4.11 SEM morphology of **c**) $[Ni(bipy)(phen)Cl]^{+}$-Y before

d) $[Ni(bipy)(phen)Cl]^{+}$-Y after Soxhlet extraction

The Surface area and pore volume studies of neat zeolite (NaY), $[Fe(bipy)(phen)Cl_2]^{+}$-Y and $[Ni(bipy)(phen)Cl]^{+}$-Y were performed using Brunauer-Emmett-Teller (BET) and Horvath-Kawazoe methods (HK), respectively and the results are shown in Figure 4.12. The two catalysts and neat zeolite show typical type-I characterstics in their N_2 sorption

isotherms and, according to IUPAC and Brunauer et al. classification, they are characteristic of micro porous materials [160,161]. This also indicates that the characteristic micro porous structure of NaY is preserved during the encapsulation of metal complexes into zeolite supercage. The surface area of NaY has the values of 634 m^2 g^{-1}. However, after encapsulation of the respective metal mixed ligand complexes into the zeolite cage, the surface area was reduced to 519 m^2 g^{-1} and 548 m^2 g^{-1} for $[Fe(bipy)(phen)Cl_2]^+$-Y and $[Ni(bipy)(phen)Cl]^+$-Y catalyst, respectively. The pore volume of NaY (0.23 cm^3 g^{-1}) was also reduced to 0.14 cm^3 g^{-1} and 0.16 cm^3 g^{-1} for $[Fe(bipy)(phen)Cl_2]^+$-Y and $[Ni(bipy)(phen)Cl]^+$-Y respectively. This is primarily due to the presence of respective metal complexes in the pores of zeolite. This clearly suggests that the metal-(bipy)(phen) complex is encapsulated in the cavities of zeolite.

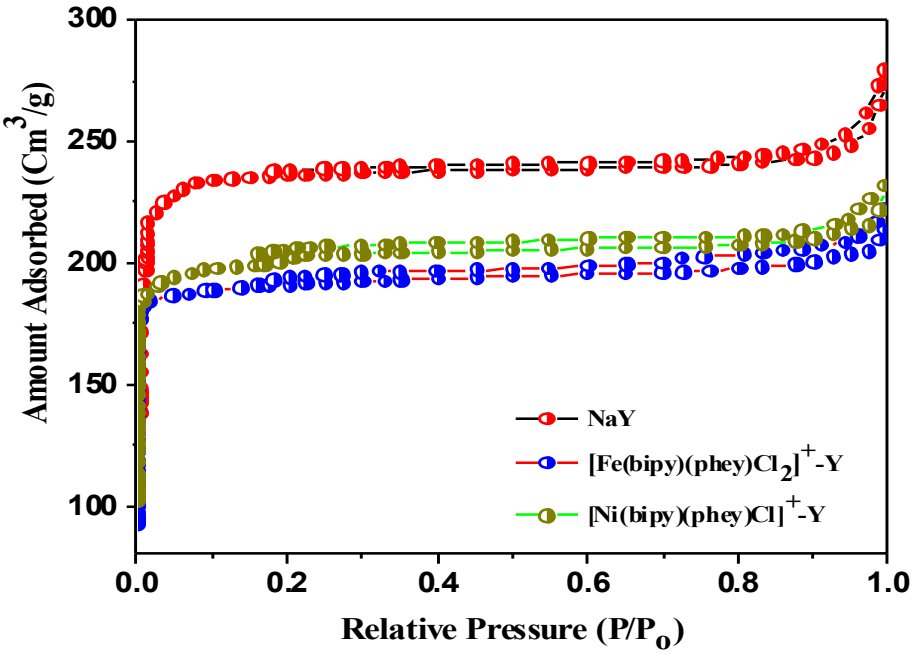

Figure 4.12 N_2 sorption isotherms plot for NaY, $[Fe(bipy)(phen)Cl_2]^+$-Y and $[Ni(bipy)(phen)Cl]^+$-Y

4.1.1.3. Spectroscopic Characterization

The FT-IR spectra of NaY as well as that of $[Fe(bipy)(phen)Cl_2]^+$ and $[Ni(bipy)(phen)Cl]^+$ complex encapsulated into zeolite cage are provided in Figure 4.13. It can be seen that vibrational bands of zeolite dominate IR spectra's of two the catalysts. The broad bands in the regions 3450 cm^{-1} and 1650 cm^{-1} are due to asymmetric stretching and bending modes of water molecules or surface hydroxylic groups, respectively [162,163]. FT-IR spectra of neat zeolite Y show strong zeolite lattice bands in the range of 450-1100 cm^{-1}. The strong and broad bands in the region 1010-1030 cm^{-1} may be attributed to the asymmetric stretching vibrations of $(Si/Al)O_4$ units [163,164]. The parent zeolite shows characteristic bands at 455, 559, 663, and 975 cm^{-1} that are attributed to -Si/Al-O bending, symmetric and asymmetric stretching modes [164-165]. The neat zeolite bands are also observed with little band shift upon introduction of the metal complexes into the zeolite supercage. This again suggests that the metal complex encapsulated catalysts retain the zeolite framework. The specific IR bands of the two encapsulated metal complexes are very weak because of their low concentration in the zeolite cage. The neat iron(III), and nickel(II) complexes show -C=C- stretching and -C-H- bending vibrations between 1310-1585 cm^{-1} and 720-850 cm^{-1}, respectively. Similar IR bands are also observed in the case of all encapsulated metal complexes with a minor shift in the position of the bands. The bands observed at 1516 and 1425 cm^{-1} in the case of the metal complexes are observed slightly shifted at 1522 cm^{-1} and 1422 cm^{-1} for iron(III) catalyst,1512 cm^{-1} and 1426 cm^{-1} for nickel(II) catalyst. The shift in absorption position in the IR spectra of the catalysts is a further confirmation for the formation of respective metal bipy-phen complex inside the cavity of zeolite framework.

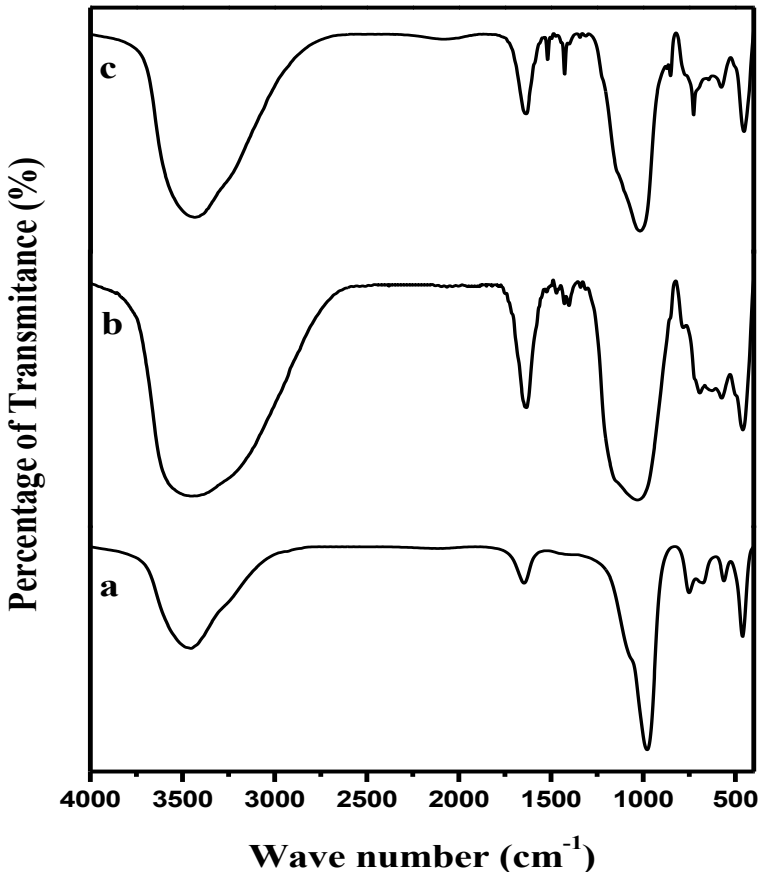

Figure 4.13 FT-IR spectra's of **a**) NaY **b**) $[Fe(bipy)(phen)Cl_2]^+$-Y and **c**) $[Ni(bipy)(phen)Cl]^+$-Y

Powder EPR spectra of neat $[Fe(bipy)(phey)Cl_2]^+$ complexes as well as the encapsulated complexes were taken in X-band microwave region (~9 GHz) at room temperature in order to acquire information about the extent of delocalization of unpaired electron and symmetry of the complex. The EPR spectra of neat $[Fe(bipy)(phey)Cl_2]^+$ complexes having *g*-values of 2.2366, 2.1040, 2.0781 and 2.0479 can be seen in Figure 4.14. However, due to the influence of the zeolite cage, the symmetry of the iron complex changes and forms broad bands having *g*-values of 4.3610, 2.0672 and 1.9976. As expected, for axially distorted octahedral Fe(III) ions, single broad band is observed with

g_{II} value of > 4.23 in all the cases which correspond to low spin d^5 ion in the weak field region. Many monomeric iron(III) complexes show an absorption pattern of similar nature, and the difference in the *g*-values between the neat and the encapsulated complexes provides a clear indication that the ferric complexes inside zeolite exists in different symmetrical environment.

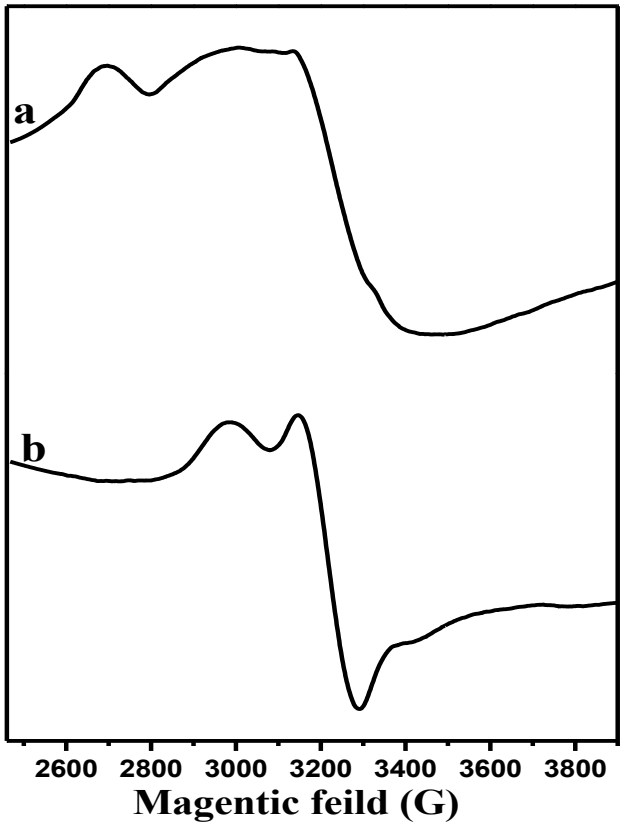

Figure 4.14 EPR spectra of **a**) $[Fe(bipy)(phey)Cl_2]^+$ **b**) $[Fe(bipy)(phey)Cl_2]^+$-Y

4.1.1.4. Thermogravimetric and Elemental Analysis

The thermogravimetric (TGA) and derivative thermogravimetry (DTG) curves of NaY, $[Fe(bipy)(phen)Cl_2]^+$ and $[Ni(bipy)(phen)Cl]^+$ complexes and zeolite encapsulated $[Fe(bipy)(phen)Cl_2]^+$ and $[Ni(bipy)(phen)Cl]^+$ complexes are displayed in Figure 4.15a

and Figure 4.15b. The two metal complexes exhibit three weight loss steps (Figure 4.15a). The first weight loss step in both neat complexes corresponds to the loss of water molecule. The second weight loss may be correlated to the loss of Cl_2 molecule coordinated to the central metal ions. In the last stage the weight loss was relatively large, i.e. with highest percentage of weight loss at 364 °C for the iron(III) complex and at 417 °C for the nickel(II) complex, which is attributed to the loss of organic moieties of the complexes. Different weight loss behaviour is observed for the respective zeolite encapsulated metal complexes, which show only two weight loss stages. The first weight loss in the temperature range of 0-150 °C was mainly due to desorption of physically adsorbed and possibly chemically bonded water molecules. The second stage weight loss, covering a wide temperature range (150-800 °C) is attributed to the decomposition of organic part of the catalyst and chlorine molecules coordinated to the central metal ions. Figure 1.15b TGA-DTG graph shows that there is substantial weight loss at 440 °C and 450 °C for $[Fe(bipy)(phen)Cl_2]^+$-Y and $[Ni(bipy)(phen)Cl]^+$-Y catalysts, respectively, which is attributed to the loss of bipy-phen mixed ligands. For the corresponding encapsulated complex the weight loss extend up to 500 °C, indicating the thermal stability of the metal complex was greatly enhanced through the encapsulation into a highly thermal resistant aluminosilicate frame work of zeolite Y. The loss of total organic component in the case of $[Fe(bipy)(phen)Cl_2]^+$-Y and $[Ni(bipy)(phen)Cl]^+$-Y upon heating up to 800 °C is consistent with the data obtained from CHN analysis (Table 4.5). The minor weight difference observed can be attributed to the decomposition of chloride ion coordinated to the metal ions.

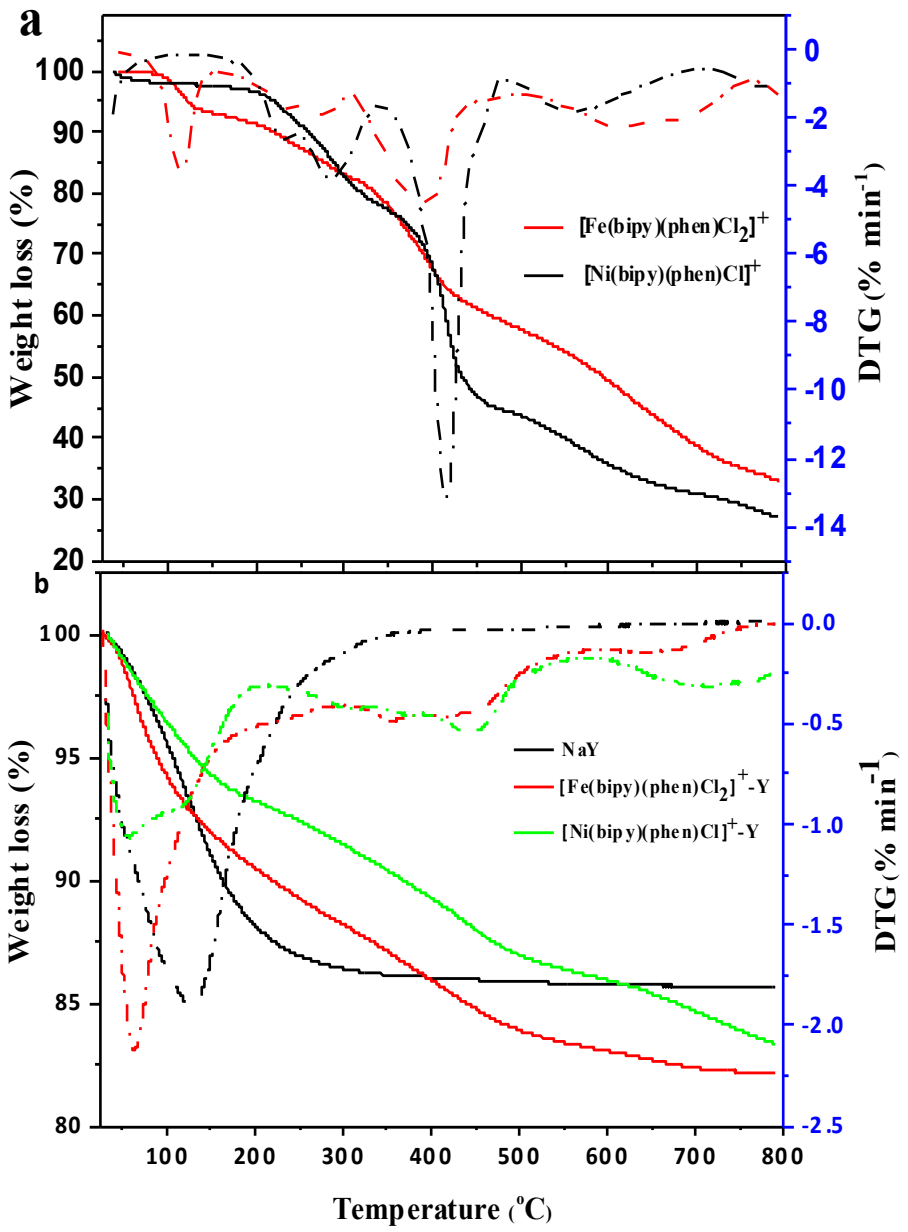

Figure 4.15 Thermogravimetric analysis (TGA) and derivative thermogravimetry (DTG) results for a) $[Fe(bipy)(phen)Cl_2]^+$ and $[Ni(bipy)(phen)Cl]^+$ **b**) NaY, $[Fe(bipy)(phen)Cl_2]^+$-Y and $[Ni(bipy)(phen)Cl]^+$-Y

Table 4.5 Results of thermogravimetric analysis and CHN analysis for the catalyst sample

Sample	Temperature (°C)	Weight loss (%)	Type of loss	Total CHN weight (%)
$[Fe(bipy)(phen)Cl_2]^+$-Y	0-150	7.93	Water desorption	-
	150-800	11.54	Complexes decomposition	10.52
$[Ni(bipy)(phen)Cl]^+$-Y	0-150	5.71	Water desorption	-
	150-800	10.85	Complexes decomposition	9.75

The result of CHN quantitative analysis of neat zeolite, neat metal complex and zeolite encapsulated metal complexes in molar ratio are presented in Table 4.6. The Si/Al ratio of neat zeolite Y, zeolite encapsulated iron(III) and nickel(II) complex was 2.46, 2.44 and 2.45, respectively. This revels that there is no dealumination during encapsulation of respective metal complexes into zeolite supercage and hence the zeolite framework was unaffected during the encapsulation process. As can be deduced from Table 4.6, the metal, carbon and nitrogen percentage values for the neat metal complexes and encapsulated metal complexes are comparable with the carbon to nitrogen ratio with respect to the theoretical value of the respective metal complexes. This provides a further evidence for the successful formation of exclusively mixed-ligand metal complexes of $[Fe(bipy)(phen)Cl_2]^+$ and $[Ni(bipy)(phen)Cl]^+$ in zeolite supercage with complexation of four nitrogen ligands with iron(III) and nickel(II) central metal ion. Nonetheless, minute

traces amounts of free metal ions are still present in the zeolite cage even after back exchange processes were applied, which however, did not significantly alter the behaviour of the zeolite encapsulated metal complexes [166, 167]. The presence of trace amount of non-exchangeable free metal ions may be attributed to the shielding by the guest molecules (metal complex) or the zeolite lattice [165].

Table 4.6 Chemical composition (molar ratio) of neat zeolite, neat metal complexes and metal catalyst

Sample	Metal (%)	Si (%)	Al (%)	Si/Al	Na (%)	C (%)	N (%)	C/N
$[Fe(bipy)(phen)Cl_2]^+$	0.22 (0.21)[a]	-	-	-	-	4.75 (4.73)[a]	0.87 (0.86)[a]	5.46 (5.50)[a]
$[Ni(bipy)(phen)Cl]^+$	0.24 (0.23)[a]	-	-	-	-	5.12 (5.09)[a]	0.93 (0.92)[a]	5.51 (5.53)[a]
Zeolite Y	-	0.79	0.32	2.46	0.32	-	-	-
$[Fe(bipy)(phen)Cl_2]^+$-Y	0.03	0.78	0.32	2.43	0.24	0.67	0.12	5.58
$[Ni(bipy)(phen)Cl]^+$-Y	0.03	0.76	0.31	2.45	0.23	0.62	0.11	5.63

[a] theoretical CHN value

4.2.2. Theoretical DFT Studies

The geometrical parameters obtained from PBE/DN level calculations for the neat and encapsulated metal complexes are depicted in Table 4.7. The geometrical parameters (such as bond length, bond angles and dihedral angle) of $[Fe(bipy)(phen)Cl_2]^+$ and $[Ni(bipy)(phen)Cl]^+$ have been compared with that of zeolite encapsulated $[Fe(bipy)(phen)Cl_2]^+$ and $[Ni(bipy)(phen)Cl]^+$ and were found to be in good agreement. The average bond length differences observed between neat metal complex and zeolite encapsulated metal complexes after optimization, were 0.081 and 0.037 Å for

$[Fe(bipy)(phen)Cl_2]^+$ and $[Ni(bipy)(phen)Cl]^+$, respectively. In addition, bond angle difference of 2.862 and 5.564 degree were observed for $[Fe(bipy)(phen)Cl_2]^+$ and $[Ni(bipy)(phen)Cl]^+$, respectively. The most significant differences are observed in the values of the bond angles and dihedral angles were around the metal ion. The change in bond angle and dihedral angle of the metal complexes on encapsulation maybe attributed to the influence of zeolite framework. It has previously been reported that Si-O bonds in zeolites have solely covalent character [110]. Therefore, the structural and electronic properties of the encapsulated metal complexes are expected tobe influenced by the electron-electron repulsions between the metal complex and the nearby partially delocalized electrons in the zeolite supercage.

Table 4.7 Bond distances (in Å), bond angles (in degree) and dihedral angle (in degree) of the optimized neat complexes and zeolite encapsulated metal complexes, (M = Fe(III) and Ni(II))

	$[Fe(bipy)(phen)Cl_2]^+$	$[Fe(bipy)(phen)Cl_2]^+$-Y	$[Ni(bipy)(phen)Cl]^+$	$[Ni(bipy)(phen)Cl]^+$-Y
Bond length				
N_1-M	2.062	2.201	1.953	1.991
N_2-M	2.102	1.992	1.870	1.888
N_3-M	2.022	2.009	1.929	1.915
N_4-M	2.139	2.004	1.886	1.875
Cl_1-M	2.162	2.175	2.266	2.160
Cl_2-M	2.162	2.237		
Bond angle				
N_1-M-N_2	94.327	85.358	97.521	97.037
N_2-M-N_3	78.702	81.004	84.159	85.347
N_3-M-N_4	95.728	92.793	98.485	92.381
N_4-M-N_1	78.627	79.553	85.011	86.086
N_1-M-N_3	86.640	84.879	140.449	123.854
N_2-M-N_4	171.345	164.160	110.319	103.685
N_1-M-Cl_1	87.539	88.087	86.605	94.162
N_2-M-Cl_1	93.624	94.574	109.227	118.367
N_3-M-Cl_1	169.980	171.962	85.792	87.096
N_4-M-Cl_1	91.108	89.745		
N_1-M-Cl_2	169.705	172.302		
N_1-M-Cl_2	93.984	97.226		
N_1-M-Cl_2	89.042	88.357		
N_1-M-Cl_2	92.528	97.148		
Dihedral angle				
N_1-N_2-N_3-N_4	47.204	49.712	30.301	42.048

- Cl_1, Cl_2 and N_1, N_2, N_3, N_4 are belongs to chlorine and nitrogen atoms attached to the metal ion (M) in the bipy-phen complex

Figure 4.16 shows the HOMO and LUMO for the neat complexes and zeolite encapsulated metal complexes, and the calculated energy values are given in Table 4.8.

The calculation were performed considering spin-unrestricted systems, since the energies of HOMO and LUMO orbitals that correspond to the spin-up and spin-down state were found to be same in both neat and encapsulated system of iron (III) and nickel (II) mixed ligand complexes. It can be deduced from the data in Table 4.8 that the individual HOMO and LUMO energies of the metal complexes increase upon encapsulation into zeolite, indicating that the complexes are destabilized upon encapsulation. Moreover, the HOMO-LUMO gaps ($\Delta E_{H\text{-}L}$) of $[Fe(bipy)(phen)Cl_2]^+$ and $[Ni(bipy)(phen)Cl]^+$ are found to decrease upon encapsulation (Figure 4.17 and Figure 4.18). This indicates that transfer of electrons from the prepared catalysts is much more feasible than neat complexes. The change in the energies of the HOMO-LUMO orbital upon encapsulation of $[Fe(bipy)(phen)Cl_2]^+$ and $[Ni(bipy)(phen)Cl]^+$ may be due to either the effect of the counter ion in zeolite Y or the steric constraint generated by the zeolite supercage. A metal complex confined inside the zeolite is subjected to coulombic effect. This coulombic effect is produced by the charge redistribution along the framework because of the partial ionic character of the zeolite lattice. This charge redistribution generates a strong coulombic field in the cavities, which might alter the energy level of the transition-metal complexes [107,154,164].

Table 4.8 Calculated Energy of HOMO and LUMO (in eV), HOMO-LUMO gap ($\Delta E_{H\text{-}L}$, in eV), Global Hardness (η, in eV) and Global Softness (s, in eV)

Sample	E_{HOMO}	E_{LUMO}	$\Delta E_{H\text{-}L}$	η	s
$[Fe(bipy)(phen)Cl_2]^+$	-0.563135	-0.542304	0.020831	0.010416	48.01
$[Fe(bipy)(phen)Cl_2]^+$-Y	-0.420351	-0.404554	0.015797	0.007898	63.30
$[Ni(bipy)(phen)Cl]^+$	-0.463879	-0.434131	0.029748	0.014874	33.61
$[Ni(bipy)(phen)Cl]^+$-Y	-0.378830	-0.354480	0.024350	0.012174	41.07

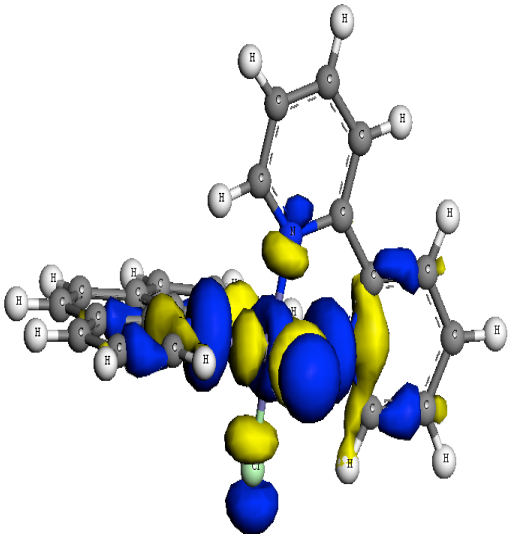

HOMO ($[Fe(bipy)(phen)Cl_2]^+$)

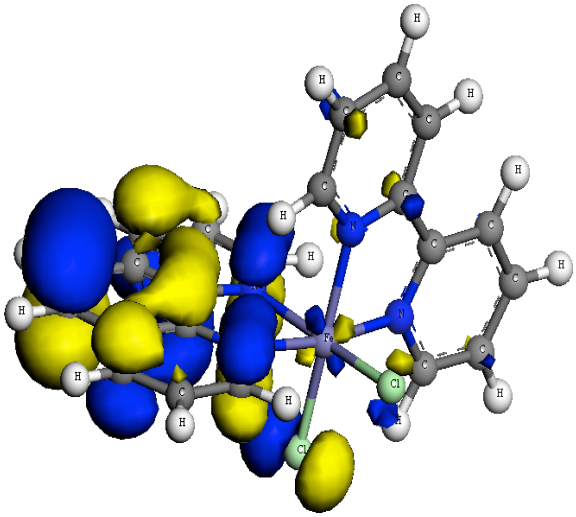

LUMO ($[Fe(bipy)(phen)Cl_2]^+$)

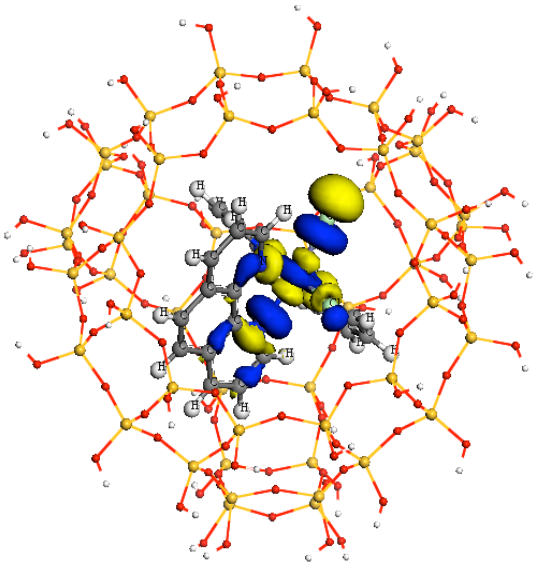

HOMO ($[Fe(bipy)(phen)Cl_2]^+$-Y)

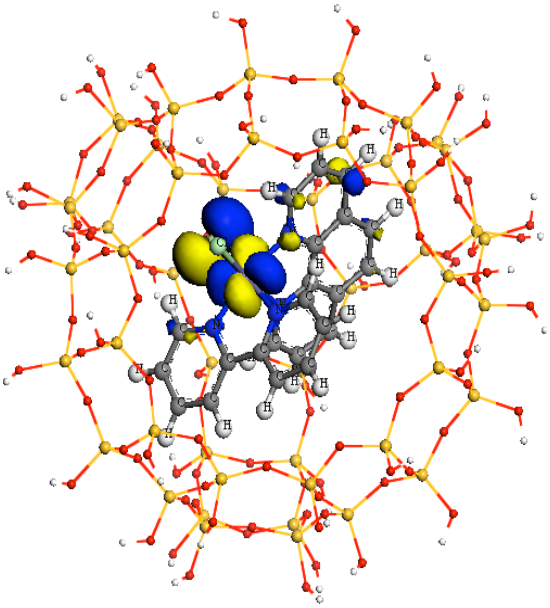

LUMO ($[Fe(bipy)(phen)Cl_2]^+$-Y)

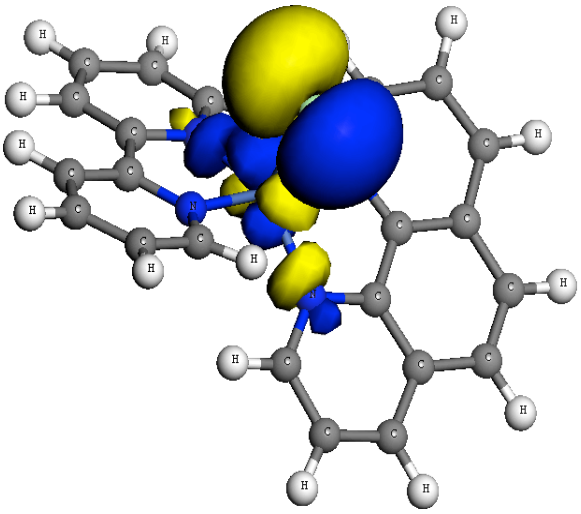

HOMO ([Ni(bipy)(phen)Cl]$^{+}$)

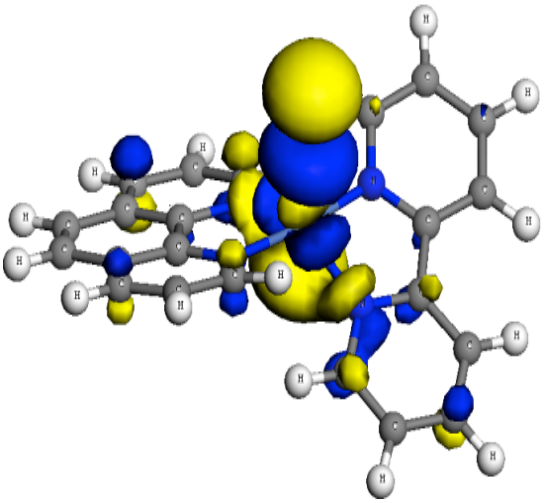

LUMO ([Ni(bipy)(phen)Cl]$^{+}$)

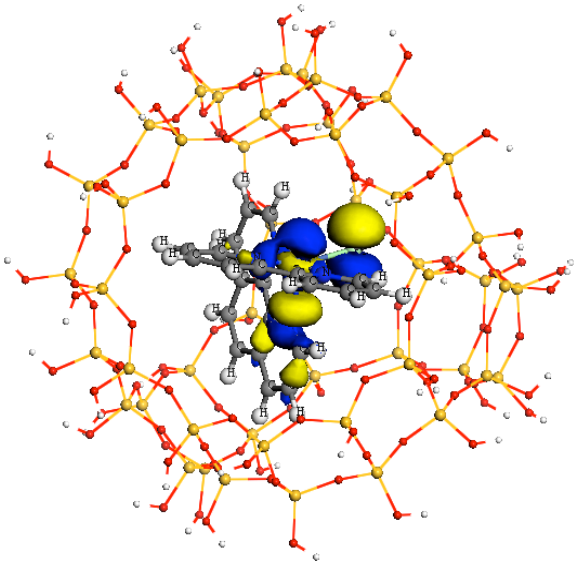

HOMO ([Ni(bipy)(phen)Cl]$^{+}$-Y)

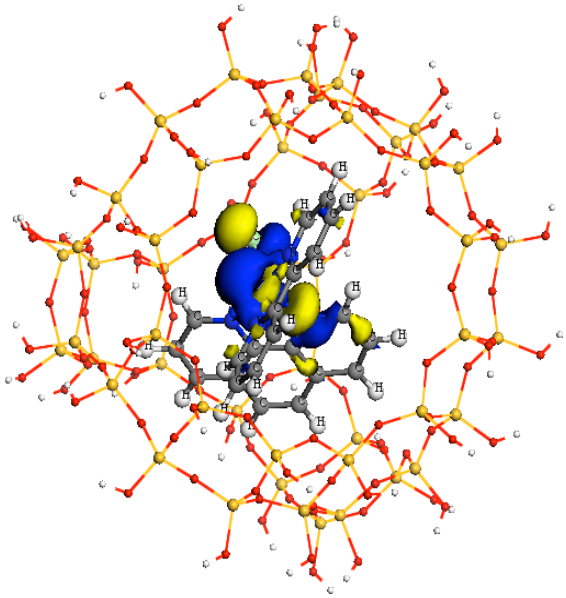

LUMO ([Ni(bipy)(phen)Cl]$^{+}$-Y)

Figure 4.16 Schematic representation of the HOMO and LUMO level of the neat and encapsulated complexes Fe(III) and Ni(II) complexes of 1,10-phenanthroline and 2,2'-bipyridine ligands

Applying Koopmans' theorem, global hardness (η) and softness (s) values of the neat and encapsulated complexes were calculated. It can be extracted from Table 4.8 that the global hardness values of $[Fe(bipy)(phen)Cl_2]^+$ and $[Ni(bipy)(phen)Cl]^+$ decrease on encapsulation into the zeolite cavities. On the other hand, the softness values of the metal complexes increase on encapsulation. According to the maximum hardness principle (MHP) and the minimum polarizability principle (MPP), (the hardness measures the stability of structure and the polarizablity (softness) measures reactivity), the most stable structure has maximum hardness and the less reactive species has minimum softness value. Hence, it is clear that the complexes $[Fe(bipy)(phen)Cl_2]^+$ and $[Ni(bipy)(phen)Cl]^+$ were destabilized and become more reactive on encapsulation compared to free metal complexes.

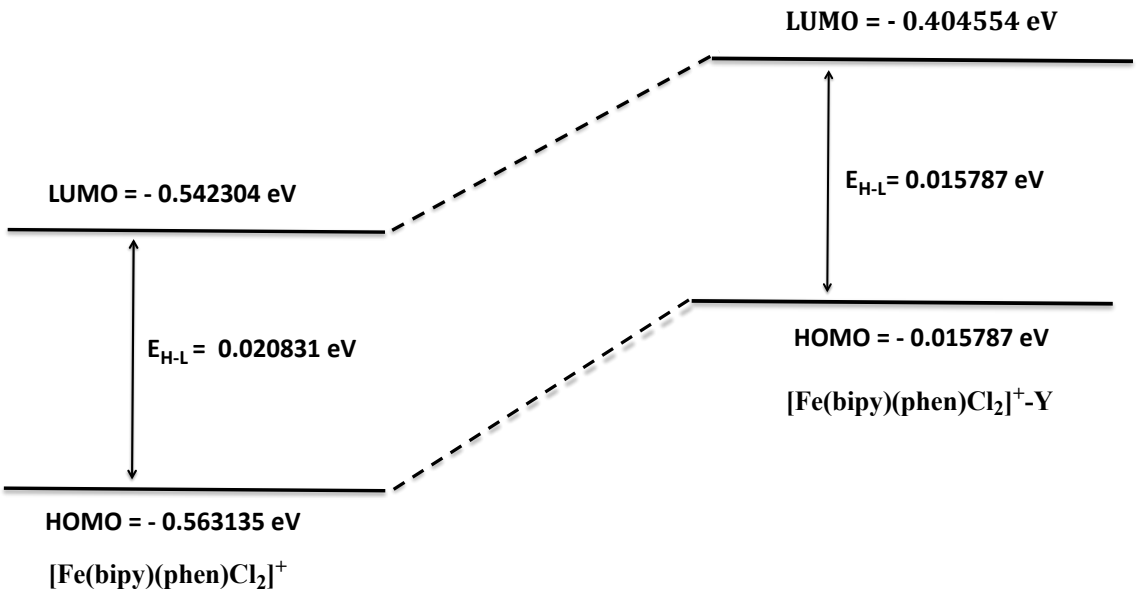

Figure 4.17 Pictorial representation of the change in the HOMO-LUMO gap for Fe(III) complexes of 1,10-phenanthroline and 2,2'-bipyridine ligands

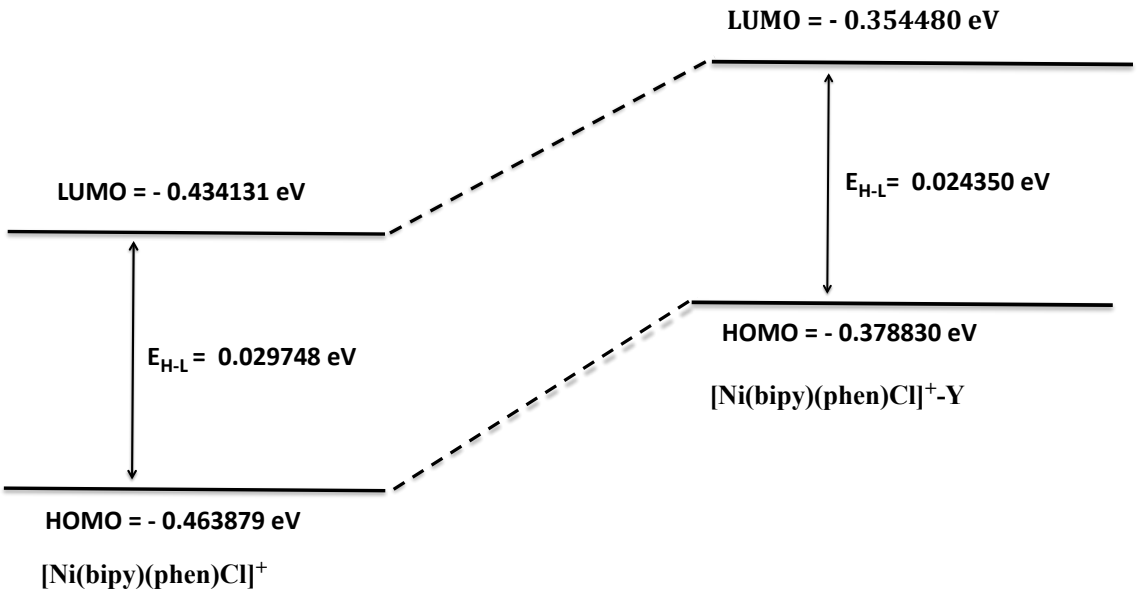

Figure 4.18 Pictorial representation of the change in the HOMO-LUMO gap for Ni(II) complexes of 1,10-phenanthroline and 2,2'-bipyridine ligands

4.2.3. Application of Synthesized Catalyst for Oxidation of *o*-Phenyl Phenol (OPP)

The potential catalytic ability of synthesized catalyst was investigated by considering the decomposition of hydrogen peroxide over time. The results show that the decomposition of hydrogen peroxide after 1 h was relatively slow for both iron (6.89%) and nickel (4.63%) based heterogeneous catalyst. However, after 2 h contact time the decomposition rate of hydrogen peroxide became greater for iron (22.75%) than nickel (19.47%) catalyst. These results indicate that $[Fe(bipy)(phen)Cl_2]^+$-Y and $[Ni(bipy)(phen)Cl]^+$-Y require a relatively longer contact time to attain the maximum equilibrium for generation of hydroxyl radicals [167,169].

To study the role of catalyst and hydrogen peroxide in degradation of OPP (*o*-phenylphenol) as a function of time, two independent experiments were carried out. In

one experiment, hydrogen peroxide was used without any catalyst, in the other set of experiments; hydrogen peroxide together with iron(III) and nickel(II) catalysts were employed with initial OPP concentration of 25 mg L^{-1}.

It can be observed from response presented in Figure 4.19a that the residual concentration of OPP after 120 min was 5.46 mg L^{-1} (21.84%) and 7.14 mg L^{-1} (28.56%) for experiments carried out in the presence of iron(III) and nickel(II) catalyst, respectively. It is known that encapsulation of metal complexes in zeolites can result in unusual oxidation states and consequently unique chemical properties of zeolite encapsulated metal complexes may arise, which may facilitate the formation of hydroxyl radicals (•OH) from hydrogen peroxide [31,33]. Even though hydrogen peroxide is a well-known oxidizing agent with high mobility in the pores of zeolite systems; the experiment conducted with hydrogen peroxide alone did not result in a significant oxidation of OPP. The residual concentration of OPP was 19.34 mg L^{-1} (77.36%) after 120 min reaction time. These observation clearly indicates that to attain maximum oxidation of OPP, along with enhancement in the rate of the reaction, the presence of $[Fe(bipy)(phen)Cl_2]^+$-Y and $[Ni(bipy)(phen)Cl]^+$-Y catalyst were vitally important. It is known that alteration of redox potential of metal complexes by the partially delocalized electron cloud of zeolite supercage is responsible for increasing the catalytic performance of both catalysts [110]. However, the better catalytic performance exhibited by the iron(III) catalyst than nickel(II) based catalyst may be attributed to higher oxidizing capability of the Fe(III)/Fe(II) than Ni(II)/Ni(I).

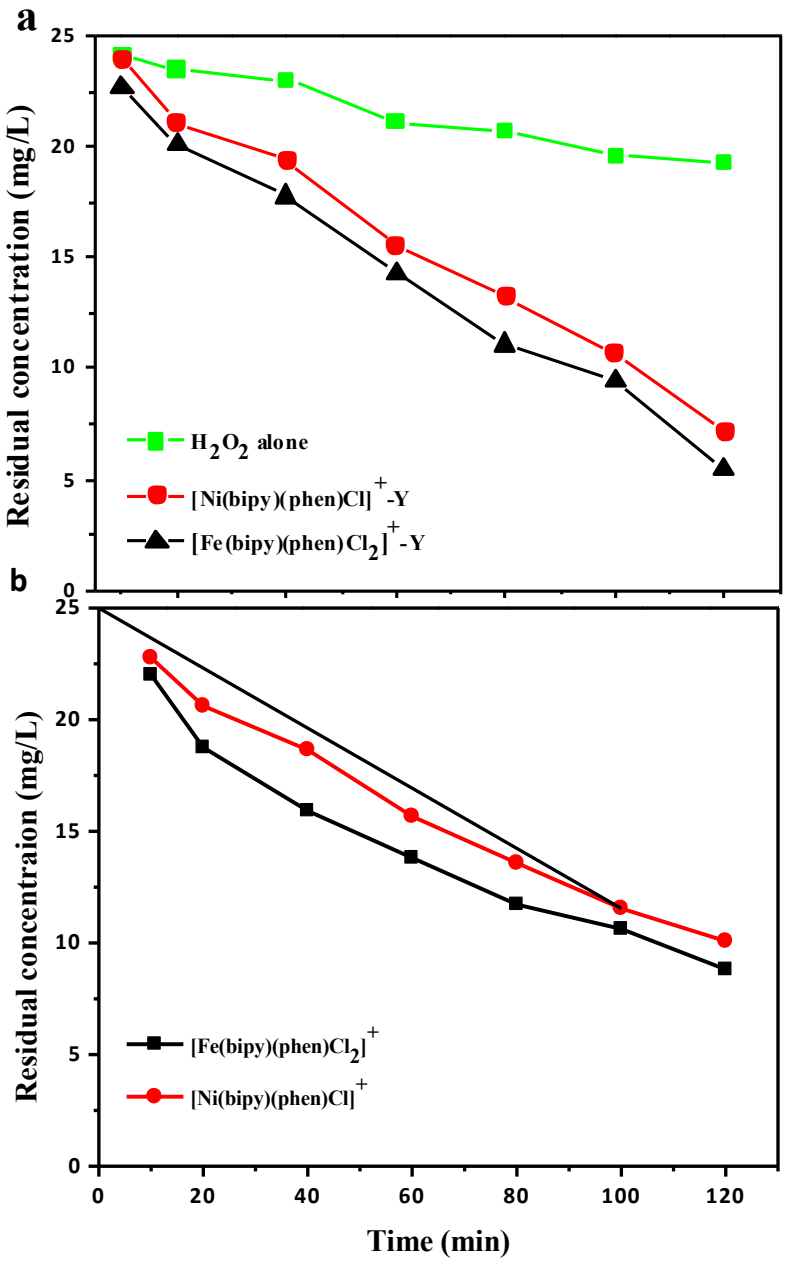

Figure 4.19 Oxidation of OPP in **a**) heterogeneous and **b**) homogeneous catalyst

In the other set of experiments the efficiency of zeolite based heterogeneous catalyst was compared with its corresponding homogeneous catalyst by taking the same amount of active metal complexes. As shown in Figure 4.19a and b**,** the residual concentration of OPP left after 120 min oxidation time using homogeneous catalyst was 8.81 mg L^{-1}

(35.24%) and 10.08 mg L^{-1} (40.32%) for iron and nickel catalyst, respectively. This demonstrates that the metal catalysts in heterogeneous phase had better overall catalytic efficiency than its homogenous counterparts. However, the rate in the heterogeneous phase was lower than that observed in the homogeneous phase, which may be due to reduced accessibility between the catalyst active site of $[Fe(bipy)(phen)Cl_2]^+$-Y and $[Ni(bipy)(phen)Cl]^+$-Y catalyst and H_2O_2 as the complex is occluded in the zeolite channels.

Therefore, the observed more efficient performance of heterogeneous catalyst over homogeneous catalyst can be explained through the kinetic effects that result from steric and electrostatic constraints imposed by the walls of the zeolite framework [110,158].

Further, to investigate the resueability of the new catalytic system, a series of three consecutive runs of reaction were performed for each catalyst. The residual concentrations obtained after the first, second and third cycle of iron(III) and nickel(II) catalyst are about 5.52, 5.71, 5.78 mg L^{-1} and 7.39, 7.55, 7.67 mg L^{-1}, respectively. These results further indicate that the synthesized catalyst can be employed for more than three successive times without losing its efficiency significantly. This fact demonstrates that the metal complex, once encapsulated in the supercages of zeolite, is prevented from leaching under reaction conditions and makes it recoverable.

4.2.4. Encapsulation and Characterization for Individual Ligands of (2,2'-Bipyridine) and (1,10-Phenanthroline) Iron(III) and Nickel(II) Complex into Zeolite Y

To investigate the effect of ligand mixing on the catalytic effeiciency, bipy-phen liganded complex with simple bipy or phen ligand complexes were encapsulated into the zeolite supper cage. The same experimental procedure was employed for both cases with exception of refluxing time and amount of ligand used. In Table 4.9 all the necessary information regarding the characterisation of the metal complexes are summerised.

Table 4.9 Physical and chemical analytical composition (molar ratio) of metal complex encapsulated into the zeolite superacge

Catalyst type	Color of the catalyst	Elemental analysis			
		Metal (%)	C (%)	N (%)	C/N
$[Fe(bipy)(phen)Cl_2]^+$-Y	Light orange	0.03	0.67	0.12	5.58
$[Ni(bipy)(phen)Cl]^+$-Y	Light blue	0.03	0.62	0.11	5.63
$[Fe(bipy)_2Cl_2]^+$-Y	Light pink	0.02	0.51	0.12	4.25
$[Ni(bipy)_2Cl_2]^+$-Y	Bluish green	0.01	0.28	0.06	4.67
$[Fe(phen)_2Cl_2]^+$-Y	Brick red	0.02	0.41	0.08	5.12
$[Ni(phen)_2Cl]^+$-Y	Light green	0.02	0.36	0.07	5.14

In contrast to $[Fe(bipy)(phen)Cl_2]^+$-Y (Light orange) and $[Ni(bipy)(phen)Cl]^+$-Y (Light blue) the color of the final catalyst for $[Fe(bipy)_2Cl_2]^+$-Y, $[Ni(bipy)_2Cl_2]^+$-Y, $[Fe(phen)_2Cl_2]^+$-Y and $[Ni(phen)_2Cl]^+$-Y is light pink, blush green, brick red and light green respectively. As presented in Table 4.9, the elemental composition analyses also confirmed the purity of simple bipy or phen iron and nickel complexes encapsulated into the zeolite supercage. The chemical analyses of encapsulated samples indicates the

presence of organic matter with a C/N ratio roughly similar to the theoretical value and it indicates the successful formation of intended Fe(III) and Ni(II) complexes into the zeolite supercage. In comparison, bipy-phen mixed liganded iron(III) and nickel(II) complexes have, as expected, had different in C/N values and metal-to-carbon ratios.

Subsequently, the removal efficiencies of simple iron(III) and nickel(II) bipy or phen and mixed bipy-phen ligand complexes based catalysts were compared on batch oxidation of 2-phenyl phenol (OPP). The observed residual concentration of 2-phenylphenol (OPP), after 120 min oxidation time, were 8.19, 8.75, 10.81 and 11.66 mg L^{-1} for $[Fe(phen)_2Cl_2]^+$-Y, $[Ni(phen)_2Cl]^+$-Y, $[Fe(bipy)_2Cl_2]^+$-Y and $[Ni(bipy)_2Cl_2]^+$-Y catalysts, respectively. Compared to mixed ligand based catalysts such as $[Fe(bipy)(phen)Cl_2]^+$-Y (5.46 mg L^{-1}) and $[Ni(bipy)(phen)Cl]^+$-Y (7.13 mg L^{-1}), simple bipy or phen metal complex based catalyst demonstrated lower catalytic activity. The increase in catalytic efficiency of the mixed ligand based metal complexes maybe attributed to the existence of the central metal ions in two different coordination atmospheres that may have enabled them to exhibit better oxidation properties. In conclusion, it can be deduced that the mixed ligand complexes of Fe(III) and Ni(II) are more efficient catalysts for the oxidation of OPP than the individual complexes of phen or bipy.

4.3. Iron(III), Nickel(II) and Copper(II) N,N′-Disalicylidene-1,2-Phenylenediamine Complex Encapsulated into Zeolite Cage

4.3.1. Characterization of the Catalyst

4.3.1.1. Background

The formation of the Schiff base ligand was investigated by ^{1}H NMR, ^{13}C NMR and FT-IR and its results are tabulated in Figure 7.5, 7.6 and 7.7 (Appendices). ^{1}H NMR (500 MHz, DMSO-d_6) of the Schiff base ligand shows a signals at δ (ppm): 6.91-6.93 (m, 2H, arom), 7.02-7.05 (d, 2H, arom), 7.20-7.28 (m, 2H, arom), 7.30-7.35, (m, 2H, arom), 7.35-7.40 (d, 4H, arom) 8.62 (s, 2H, 2 × N=C<u>H</u>), 13.03 (s, 2H, 2 × O<u>H</u>). ^{13}C NMR (500 MHz, DMSO-d_6) Schiff base ligand shows signals at δ (ppm): 163.74, 161.36, 142.57, 133.38, 132.36, 127.71, 119.75, 119.25, 118.99, and 117.56, IR bands at 1629 cm^{-1} (-CH=N-) and CHN analysis ($C_{20}H_{16}N_2O_2$): C=76.21, H=5.23 and N=8.93 is in agreement with the theoretical values (i.e. C=75.93, H=5.10 and N=8.86). Thus, based on the ^{1}H NMR, ^{13}C NMR, FT-IR and CHN data the successful synthesis of Salophen ligand is confirmed.

Ship-in-a-bottle method was adopted to encapsulate Fe(III), Ni(II) and Cu(II) Salophen complexes into NaY zeolite. During the encapsulation stage, ligand species reacts with the pre-exchanged metal ions in the zeolite cavities to give encapsulated metal Salophen complexes.

4.3.1.2. Structural, Morphological and Textural Properties of Materials

The X-ray diffraction patterns of neat zeolite Y and zeolite encapsulated metal Salophen complexes were recorded at room temperature at 2θ values between 5° and 50°. The

results are presented in Figure 4.20. The XRD patterns of encapsulated metal complexes are similar to that of neat zeolite Y, though slight change in the peak intensity of the bands was noticed, which indicated that the framework of zeolite had not undergone any significant structural change during encapsulation. The relative peak intensity of neat zeolite was in the order of $I_{331} > I_{220} > I_{311}$, but it is clearly seen from the Figure 4.20 that for all catalysts there were changes in the relative intensities (i.e. $I_{331} > I_{311} > I_{220}$) upon impregnation of NaY with metal Salophen complex. This difference in peak intensity is a clear indication that respective metal complexes were distributed all over the zeolite cage following complex formation. It is also reported that an empirically derived relationships exists between the relative peak intensities at around $2\theta < 20^{o}$, i.e. I_{220} at $2\theta = 10°$, I_{311} at $2\theta = 12°$ and I_{331} at $2\theta = 16°$ and cation location in faujasite type zeolites [170]. Moreover, no new peaks were detected in the zeolite-encapsulated complexes due to the low concentration of metal complexes in the zeolite nano pores. These observations have been reported previously [133,165,171].

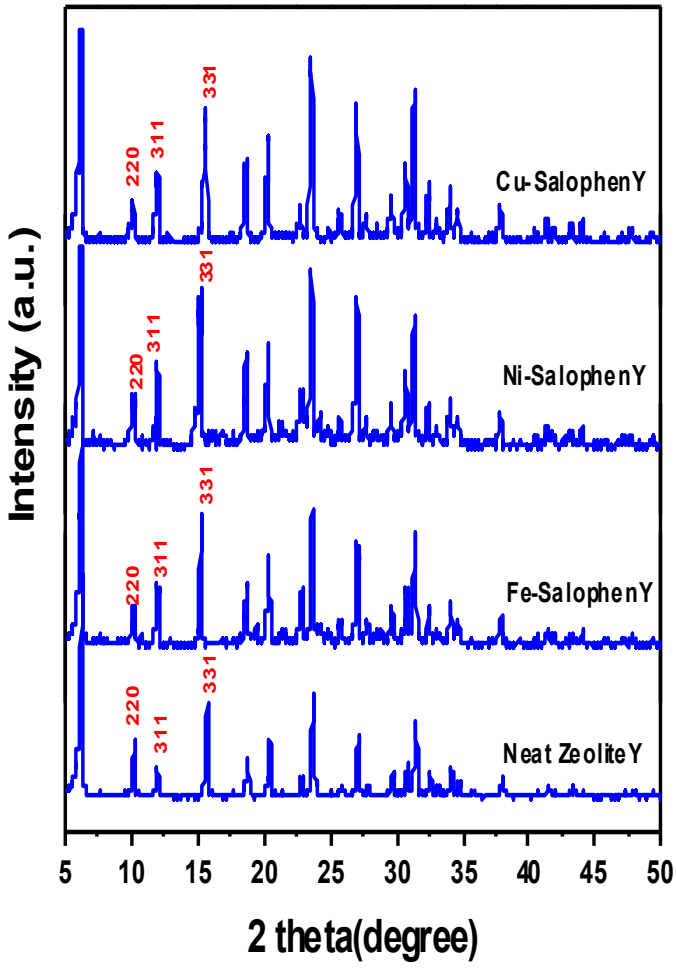

Figure 4.20 X-ray powder diffraction patterns of neat zeolite and respective catalysts

The prepared catalyst was washed by extensive Soxhlet extraction with organic solvents to ensure complete removal of the ligand species, surface complexes and metal ions. Consequently, to determine the efficiency of the applied Soxhlet extraction, SEM morphologies of the metal catalysts before and after Soxhlet extraction were taken (Figure 4.21, 4.22 and 4.23). The SEM image of samples taken before Soxhlet extraction clearly show aggregates of species on the surface. However, the surface appears to be clean, having well defined zeolite crystals in the SEM image taken after Soxhlet

extraction. This reveals the effectiveness of Soxhlet extraction to remove surface adsorbed metal complex or/and metal ions.

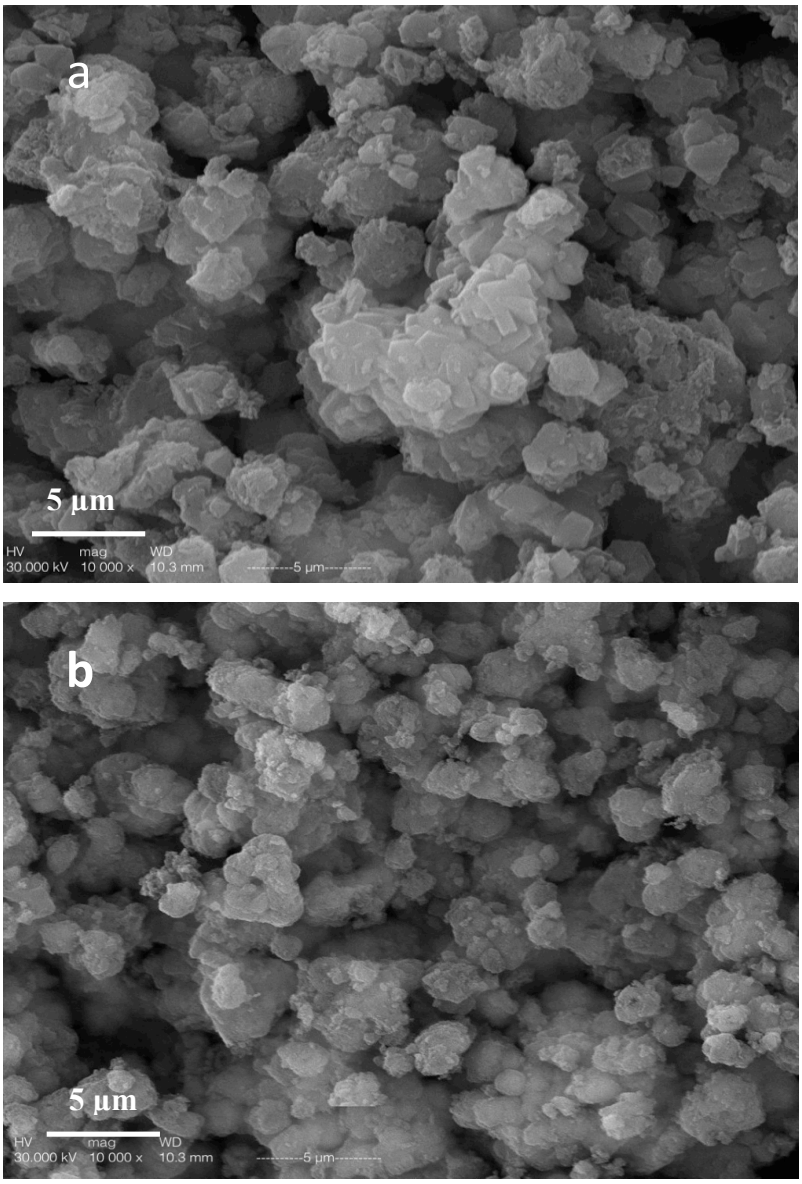

Figure 4.21 SEM morphology of **a**) Fe-Salophen-Y before **b**) Fe-Salophen-Y after Soxhlet extraction

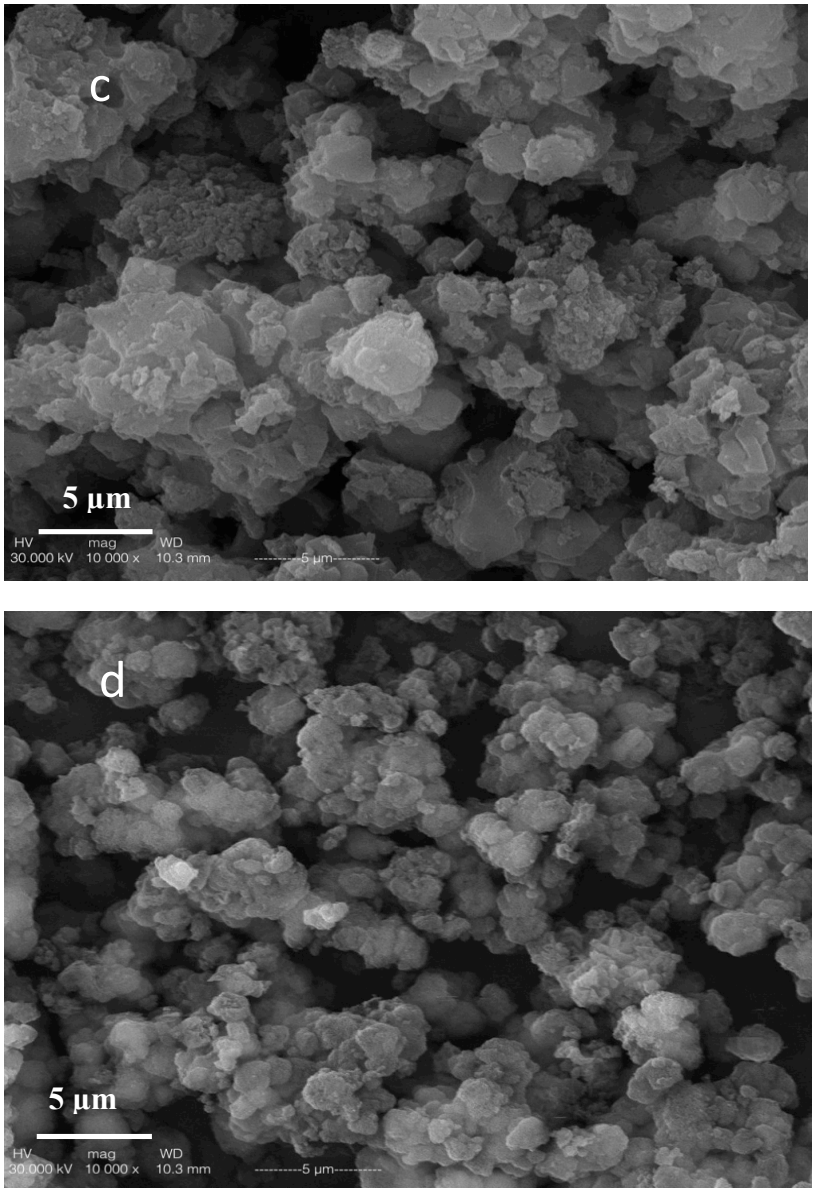

Figure 4.22 SEM morphology of **c**) Ni-Salophen-Y before **d**) Ni-Salophen-Y after Soxhlet extraction

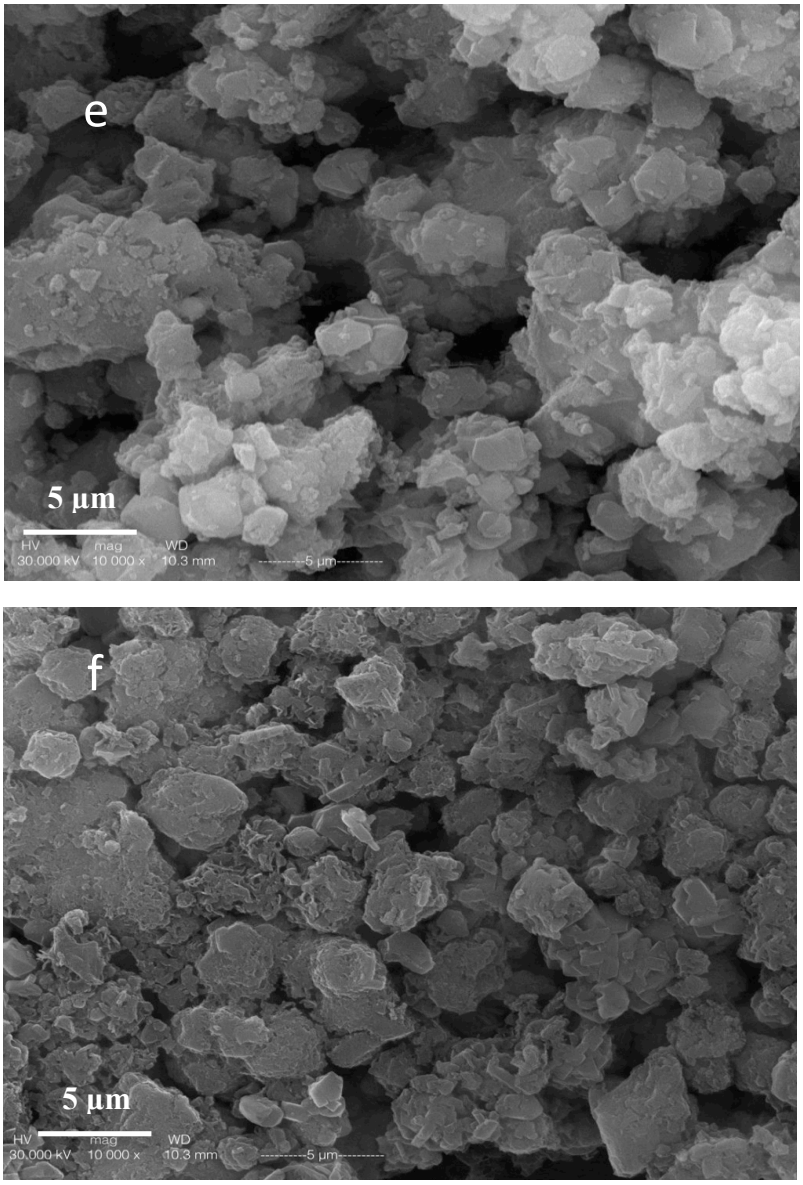

Figure 4.23 SEM morphology of **e**) Cu-Salophen-Y before **f**) Cu-Salophen-Y after Soxhlet extraction

The BET adsorption and desorption isotherms for zeolite Y, iron(III), nickel(II) and copper(II) Salophen complex encapsulated into zeolite Y are shown in Figure 4.24. The curves in the figure illustrating adsorption and desorption isotherms for zeolite Y and synthesized catalysts show typical type-I according to the International Union of Pure and

Applied Chemistry (IUPAC) and BET classification [172]. This is the characteristic of micro porous materials and it reveals that the crystalline structure of the zeolite was not affected by the encapsulation. BET surface area and micro pore volume were calculated by BET and Horvath-Kawazoe theories respectively and the values are given in Table 4.10. As shown in the Table, there is a decrease in both surface area and pore volume for all three zeolites encapsulated metal complexes as compared to neat zeolite. Since the zeolite framework structure was not affected by encapsulation, as can be seen from N_2 sorption isotherms plot in the Figure 4.24, such lowering of surface area and pore volume of each catalyst is an indication of the formation of particular metal complex by ‘‘ship-in-a-bottle’’ approach within the super cages of zeolites and not on the external surface. A similar observation is also found for the inclusion of metal dimethylglyoxime and salen complexes into zeolite Y [173]. Nevertheless, the decrease in the surface area and pore volume of the catalyst depended on the amount of incorporated metal complex as well as their molecular size and geometry inside the zeolitic host [174]. As a result, compared to neat zeolite their respective pore volume were reduced by about 23, 21 and 26% respectively upon encapsulation of Fe(III), Ni(II) and Cu(II) complexes of Salophen ligand into zeolite Y. This is also consistent with the quantitative data obtained from TGA and CHN analysis.

Table 4.10 BET surface area and pore volume of neat zeolite Y and catalyst

Sample	S_{BET} area ($m^2 g^{-1}$)	Pore volume ($cm^3 g^{-1}$)
Neat zeoliteY	567	0.32
Fe-SalophenY	437	0.28
Ni-SalophenY	447	0.29
Cu-SalophenY	420	0.27

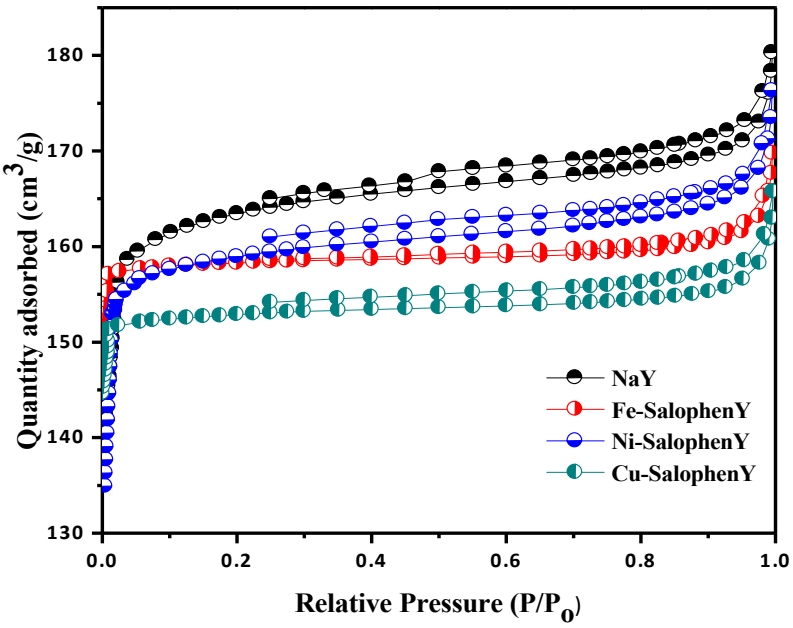

Figure 4.24 N_2 sorption isotherms plot for neat zeolite Y and zeolite encapsulated metal Salophen complex

4.3.1.3. Spectroscopic Characterization

A preliminary confirmation of the successful formation of metal Salophen complexes in the zeolite Nano pore was made on the basis of comparison of IR spectra of the zeolite encapsulated metal complexes with Salophen ligands and neat zeolite Y as shown in Figure 4.25. IR spectra of all zeolite encapsulated metal Salophen complexes and neat zeolite Y had an intense band at 1022, 791 and 463 cm^{-1} attributable to the asymmetric stretching, symmetric stretching and bending frequency of Al-O-Si framework of zeolite respectively [175-177]. This indicated that due to encapsulation of the metal complex, the zeolite framework did not undergoing any significant structural changes. In the spectra of the ligand, the strong band at 1629 cm^{-1} can be ascribed to the *ν*C=N, and the characteristic band at 1293 cm^{-1} can be assigned to *ν*(phenolic C-O). As compared to

Salophen ligand, some changes had taken place in the IR spectra of zeolite encapsulated metal complexes. The spectral band due to azomethine (νC=N) was shifted by 13-16 cm^{-1} to lower wave number and appeared at 1613, 1615 and 1613 cm^{-1} for iron(III), nickel(II) and copper(II) catalyst respectively. In the same manner the spectral band due to ν(phenolic C-O) had also shifted towards a lower wave length and appeared at 1276, 1276 and 1275 cm^{-1} for iron(III), nickel(II) and copper(II) catalyst respectively. This indicates the possibility of coordination of the imino nitrogen (-CH=N-) and phenolic oxygen (-OH) to the metal ions. The less intense bands appearing at the lower frequency region around 500 cm^{-1} in the encapsulated complexes originate from νM-N=C vibrations. Thus, FT-IR spectral analysis provides evidence for the encapsulation of metal complexes in the zeolite matrix.

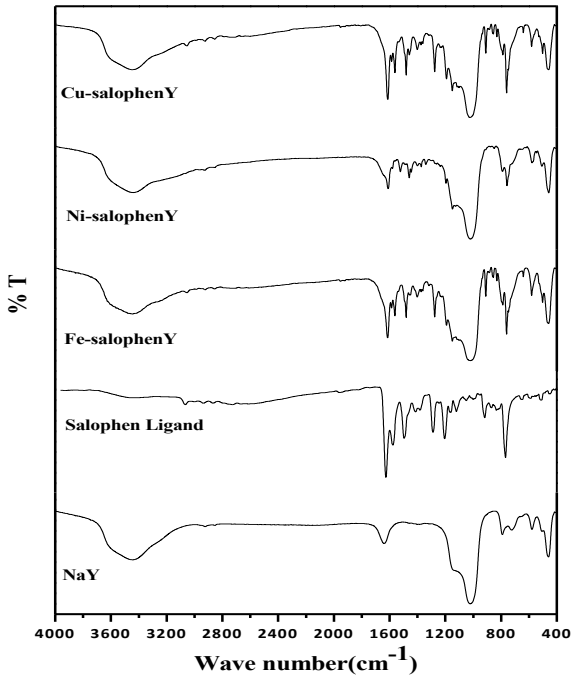

Figure 4.25 FT-IR spectrum of neat zeolite and zeolite encapsulated metal Salophen complex

4.3.1.4. Elemental Analysis

The thermograms of neat zeolite Y and metal Salophen complex encapsulated into zeolite cage are depicted in Figure 4.26. Unlike the neat zeolite Y, the metal catalysts showed two stage weight losses and this is an indication of organic species residing in the zeolite cage. The first stage weight loss from 35 °C till 250 °C for iron(III), nickel(II) and copper (II) catalysts corresponded to losses of loss of about 13%, 11% and 15 %, respectively. These correspond to desorption of physically adsorbed and occluded water molecules from zeolite. As the temperature increased the three metal catalysts showed different TGA-DTG pattern due to the various concentration of metal Salophen complex inside the zeolite cage. The weight loss started immediately after the first stage in the wider temperature range of 250-650 °C suggesting the slow decomposition of Salophen chelating ligand. The TGA-DTG showed two peak at 305 °C and 448 °C with a weight loss of about 11.4% for iron(III), at 356 °C and 438 °C corresponding to a weight loss of about 9.5% for nickel(II) and at 332 °C and 401 °C with a weight loss of about 12.4% for copper(II) catalyst. These weight losses are associated with decomposition of respective zeolite encapsulated Salophen metal complexes. The weight loss associated with the second stage is in good agreement with C, H, and N content (Table 4.11) in the zeolite encapsulated metal complexes.

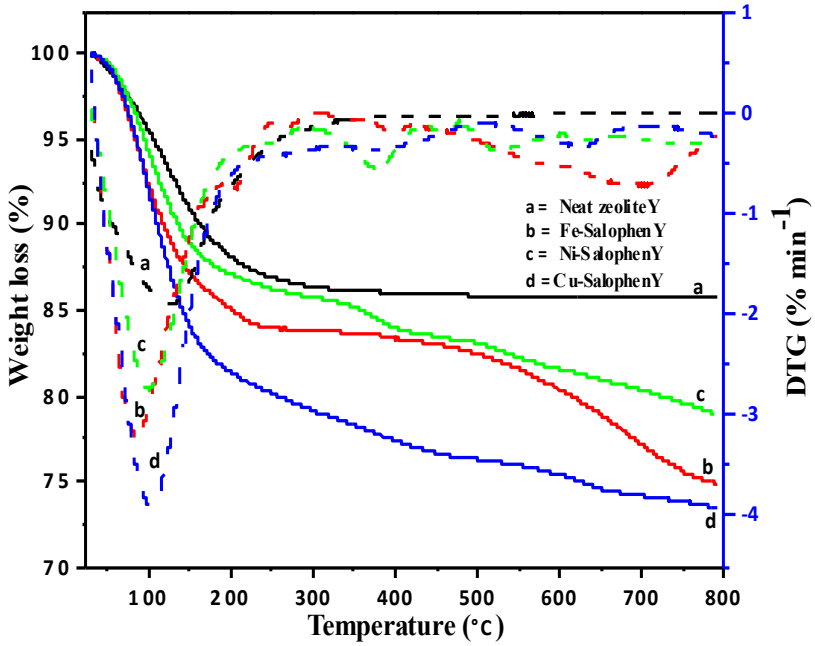

Figure 4.26 TGA profiles of neat zeolite Y and zeolite encapsulated metal Salophen complex

According to elemental analysis data (Table 4.11), the silicon to aluminum molar ratio of zeolite encapsulated Fe(III), Ni(II) and Cu(II) Salophen complexes was almost the same as that observed for the parent zeolite Y (i.e. 2.46). This consistency of silicon to aluminum molar ratio suggests that there is no change in the zeolite framework due to the encapsulation process and leaching of aluminum did not occur. Chemical analysis data shown in Table 4.11 also confirms the purity and stoichiometry of encapsulated complexes. The chemical analyses of encapsulated samples revealed the presence of organic matter with a C/N ratio roughly similar to the theoretical value. Moreover, the metal to carbon ratio is approximately 0.05 for all the catalysts indicating the successful formations of respective metal complexes inside the zeolite cage. More interestingly, the elemental analysis data indicated that the amount of metal ions, carbon and nitrogen in

the catalysts was higher than previously reported [174]. This is an indication of presence of greater amount of the respective metal complex within the cages of zeolite than that achieved previously.

Table 4.11 Chemical composition of neat zeolite Y, neat metal complexes and metal catalyst

Sample	Metal (%)	Si (%)	Al (%)	Na (%)	Si/Al	C (%)	N (%)	C/N
Fe-Salophen complex	0.27 (0.27)[a]	-	-	-	-	5.42 (5.40)[a]	0.54 (0.54)[a]	9.97 (10.0)[a]
Ni-Salophen complex	0.27 (0.26)[a]	-	-	-	-	5.45 (5.36)[a]	0.54 (0.53)[a]	9.95 (10.0)[a]
Cu-Salophen complex	0.26 (0.26)[a]	-	-	-	-	5.33 (5.29)[a]	0.53 (0.52)[a]	9.98 (10.0)[a]
Neat zeolite Y	-	0.79	0.32	0.31	2.46	-	-	-
Fe-Salophen-Y	0.04	0.74	0.30	0.21	2.44	0.70	0.07	9.95
Ni-Salophen-Y	0.03	0.75	0.31	0.22	2.43	0.69	0.07	9.85
Cu-Salophen-Y	0.04	0.75	0.31	0.23	2.42	0.76	0.08	9.50

[a] theoretical CHN value

4.3.2. Theoretical DFT Studies

The geometrical parameters obtained from PBE/DN level calculations for the neat and encapsulated metal complexes are depicted in Table 4.12. The geometrical parameters of bond length, bond angles and dihedral angle of Fe(III), Ni(II) and Cu(II) Salophen complexes were compared with that of zeolite encapsulated Fe(III), Ni(II) and Cu(II) Salophen complexes and were found to be in good agreement. The average bond length differences observed between neat metal complex and zeolite encapsulated metal

complexes after optimization was 0.070, 0.004 and 0.014 Å for Fe(III), Ni(II) and Cu(II) Salophen complexes respectively. Similarly bond angle difference of 1.0, 0.1925 and 1.69 degree were observed for Fe(III), Ni(II) and Cu(II) Salophen complexes respectively. This indicates that, encapsulation of respective metal complexes into the zeolite super cage has an effect on the geometry of the neat complexes due to steric constraint imposed by the zeolite cage. Furthermore, the influence of zeolite framework on the geometry of the neat complexes can also be seen by comparing the values of dihedral angles of neat and encapsulated metal complexes.

Table 4.12 Bond distances (in Å), bond angles (in degree) and dihedral angle (in degree) of the optimized neat complexes and zeolite encapsulated metal complexes, (M = Fe(III), Ni(II) and Cu(II))

	FeS	FeSY	NiS	NiSY	CuS	CuSY
Bond length						
N_1-M	1.946	1.861	1.881	1.878	1.951	1.958
N_2-M	1.946	1.855	1.881	1.876	1.957	1.977
O_1-M	1.869	1.953	1.851	1.849	1.980	1.992
O_2-M	1.870	1.952	1.851	1.846	1.977	1.982
Cl-M	2.135	2.144	-	-	2.396	2.370
Bond angle						
O_1-M-O_2	84.16	85.23	83.88	83.92	86.40	89.08
O_2-M-N_2	92.14	91.72	94.74	94.72	92.82	90.20
N_2-M-N_1	82.26	81.75	86.64	86.29	83.56	83.10
N_1-M-O_1	92.15	92.26	94.74	95.10	91.82	91.56
O_1-M-Cl	104.00	103.24			100.68	99.20
O_2-M-Cl	104.11	106.69			102.59	101.68
N_2-M-Cl	99.08	98.20			96.42	97.55
N_1-M-Cl	99.10	97.43			95.10	99.08
Dihedral angle						
C-O_1-M-Cl	-83.69	-80.74	-		-67.36	-68.31
C-O_1-M-N_2	91.45	90.59	-179.78	117.83	102.58	102.34
C-O_1-M-O_2	173.19	173.22	179.97	173.25	-169.50	-169.99
C-O_1-M-N_1	16.24	17.43	-0.03	-7.79	28.20	31.14
C-O_2-M-Cl	83.77	84.65	-		75.06	65.79
C-O_2-M-N_2	-16.15	-14.44	0.03	9.67	-22.16	-31.97
C-O_2-M-N_1	-91.42	-88.04	-179.84	144.61	-99.76	-103.07
C-O_2-M-O_1	-173.23	-172.94	-179.98	-168.36	175.21	164.99

- Cl, C and N_1, N_2, O_1, O_2 are belongs to chlorine and nitrogen atoms attached to the metal ion (M) in the Salophen complex

The HOMO and LUMO for the neat complexes and zeolite encapsulated metal complexes are depicted in Figure 4.27 and their energies are given in Table 4.13. It is observed from Table 4.13 that the HOMO-LUMO energy of the metal complexes increases upon encapsulation into zeolite, indicating that the complexes are destabilized upon encapsulation. Moreover, the HOMO-LUMO gap of Fe(III), Ni(II) and Cu(II) Salophen complexes (Figure 4.28, 4.29 and 4.30) was found to decrease on encapsulation. This indicates that transfer of electrons from Fe(III), Ni(II) and Cu(II) Salophen complexes encapsulated into the zeolite cage is much more feasible than respective neat complexes.

Table 4.13 Calculated Energy of HOMO and LUMO (in eV), HOMO-LUMO gap ($\Delta E_{H\text{-}L}$, in eV), Global Hardness (η, in eV) and Global Softness (s, in eV)

Sample	E_{HOMO}	E_{LUMO}	$\Delta E_{H\text{-}L}$	η	S
$[Fe(Salophen)Cl]^+$	-0.3219	-0.2956	0.0263	0.0132	38.0228
$[Fe(Salophen)Cl]^+$-Y	-0.2726	-0.2469	0.0257	0.0128	38.9105
$[Ni(Salophen)]^+$	-0.4489	-0.3906	0.0583	0.0292	17.1527
$[Ni(Salophen)]^+$-Y	-0.3632	-0.3144	0.0488	0.0244	20.4918
$[Cu(Salophen)Cl]^+$	-0.1799	-0.1427	0.0372	0.0186	26.8817
$[Cu(Salophen)Cl]^+$-Y	-0.1725	-0.1374	0.0351	0.0176	28.4900

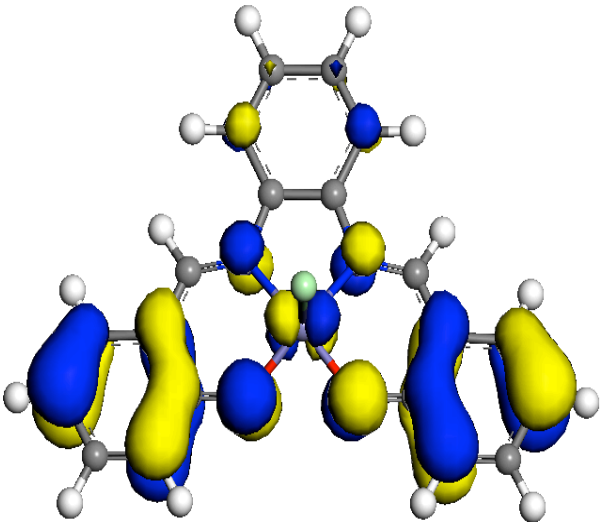

HOMO-Fe-Salophen

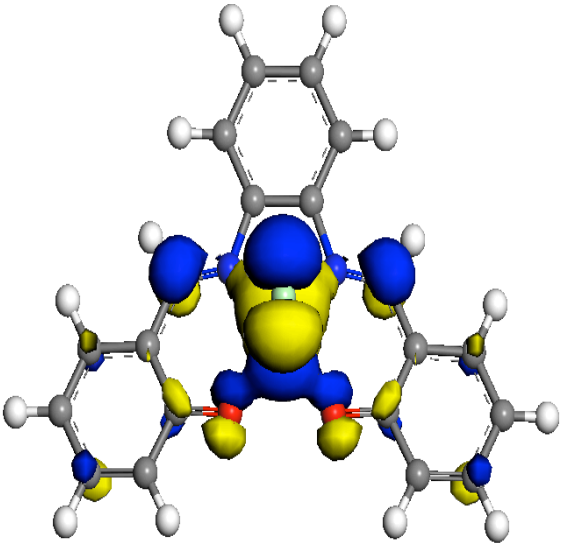

LUMO-Fe-Salophen

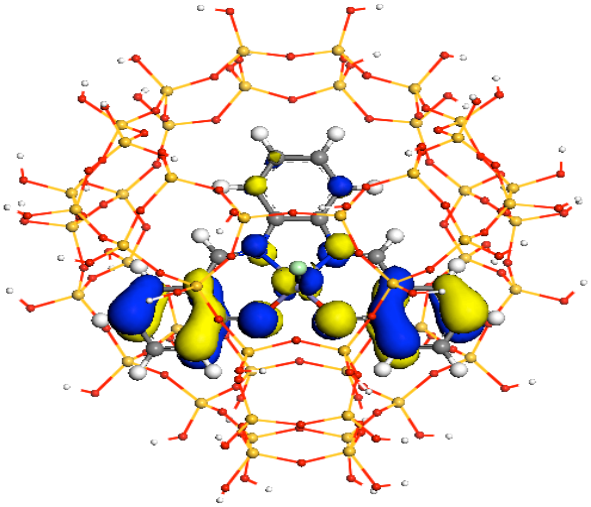

HOMO-Fe-Salophen-Y

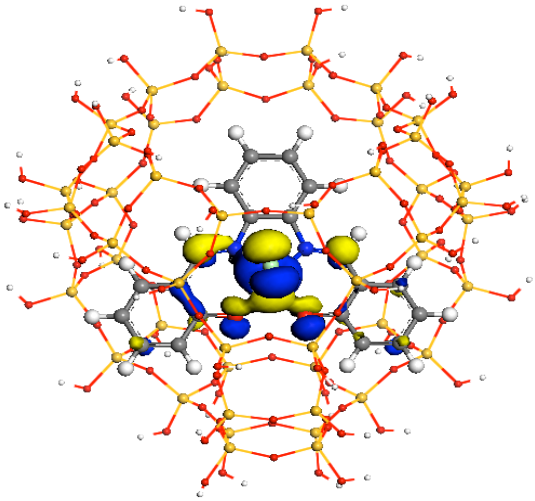

LUMO-Fe-Salophen-Y

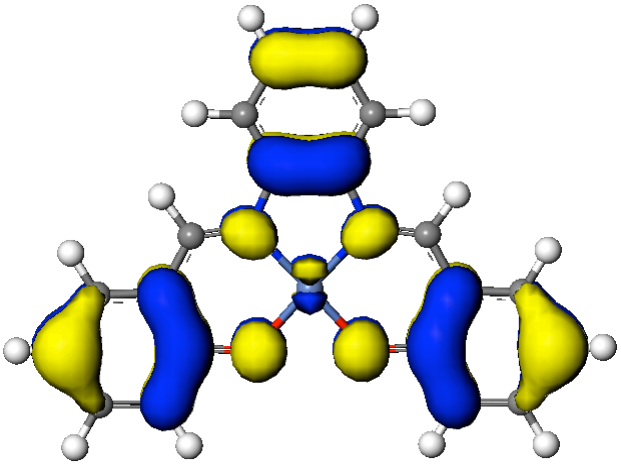

HOMO-Ni-Salophen

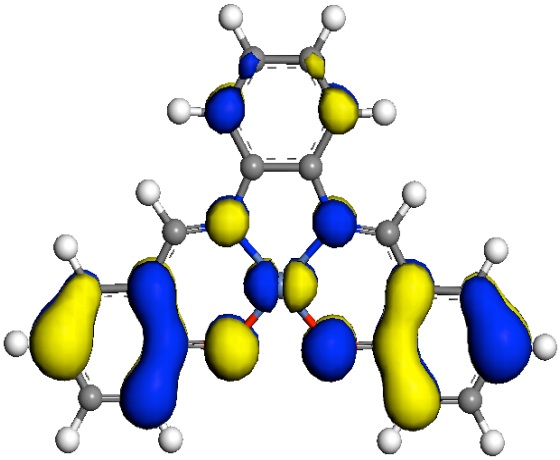

LUMO-Ni-Salophen

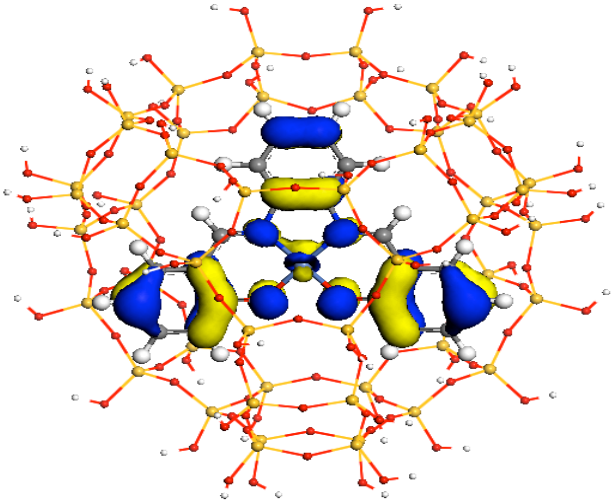

HOMO-Ni-Salophen-Y

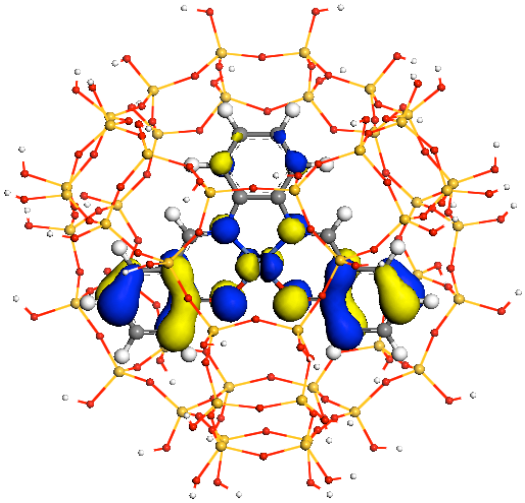

LUMO-Ni-Salophen-Y

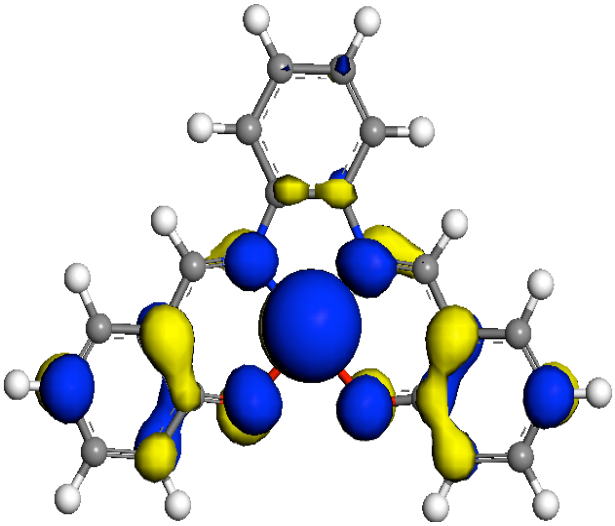

HOMO-Cu-Salophen

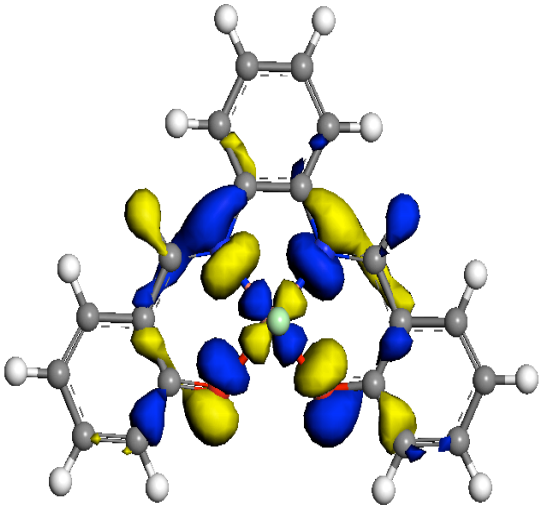

LUMO-Cu-Salophen

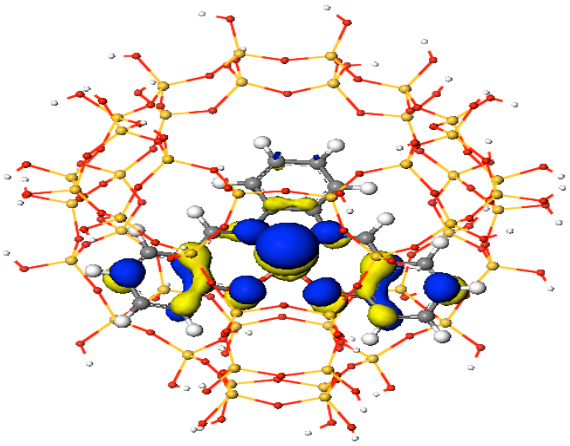

HOMO-Cu-Salophen-Y

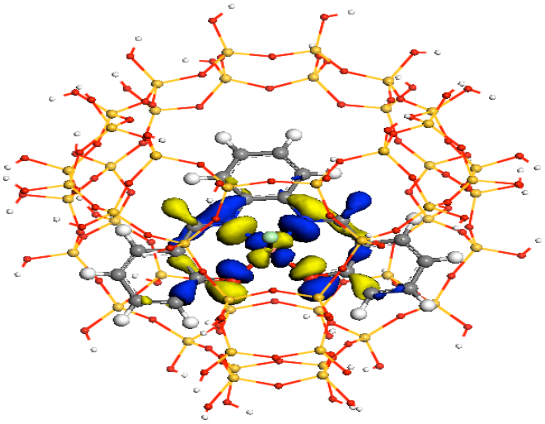

LUMO-Cu-Salophen-Y

Figure 4.27 Schematic representation of the HOMO and LUMO level of the neat and encapsulated Fe(III), Ni(II) and Cu(II) Salophen complexes

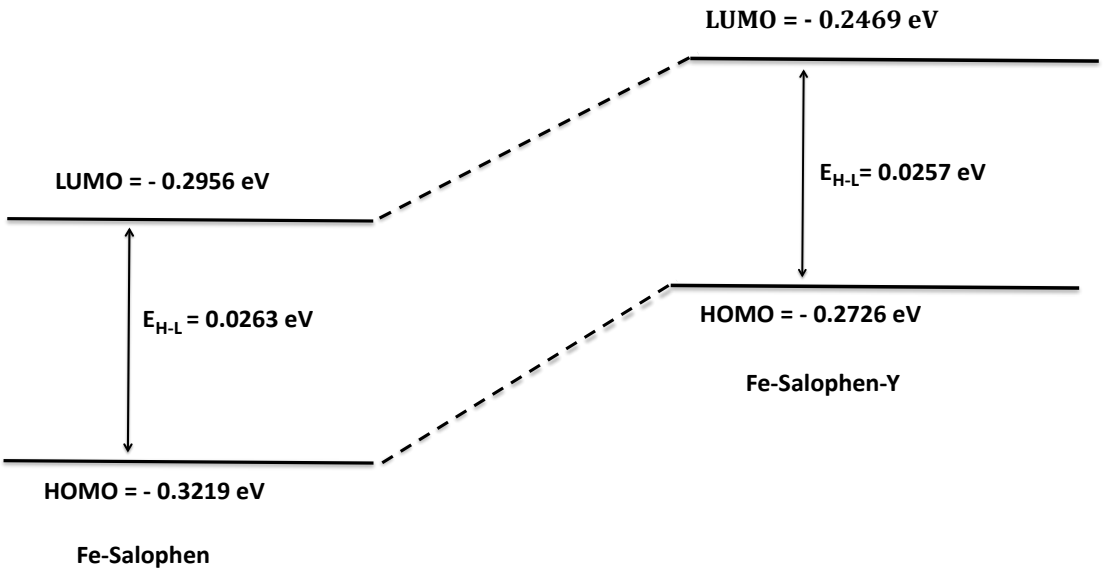

Figure 4.28 Pictorial representation of the change in the HOMO-LUMO gap iron(III) N,N′-disalicylidene-1,2-phenylenediamine complex

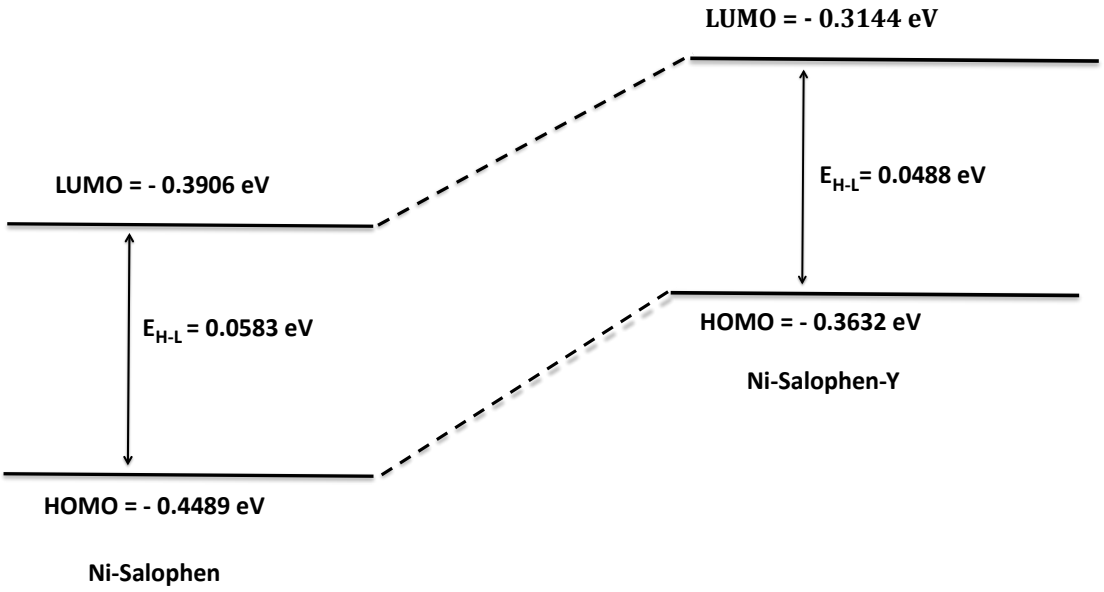

Figure 4.29 Pictorial representation of the change in the HOMO-LUMO gap for nickel(II) N,N′-disalicylidene-1,2-phenylenediamine complex

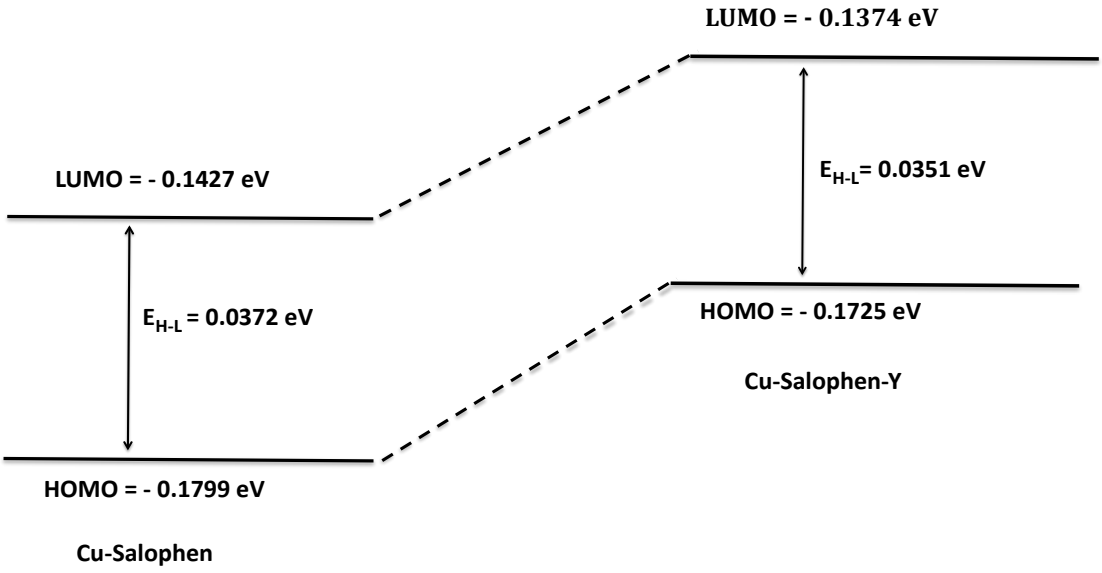

Figure 4.30 Pictorial representation of the change in the HOMO-LUMO gap for copper(II) N,N′-disalicylidene-1,2-phenylenediamine complex

Applying the Koopmans' theorem, global hardness (η) and softness (s) values of the neat and encapsulated complexes were calculated. It can be seen from Table 4.13 that the global hardness values of Fe(III), Ni(II) and Cu(II) Salophen complexes decrease upon encapsulation into the zeolite cavities. On the other hand, the softness values of the metal complexes increase on encapsulation. Hence, it is clear that the complexes Fe(III), Ni(II) and Cu(II) Salophen were destabilized and become more reactive on encapsulation compared to neat metal complexes.

4.3.3. Application of Synthesized Catalyst for Degradation of 4-Chloro-3-Methyl Phenol (PCMC)

Zeolite being a porous material has an ability to adsorb organic pollutants from aqueous solutions. Thus, in the present study, the contribution of adsorption property of zeolite in the overall Fenton like heterogeneous AOPs for the removal of pollutants from aqueous solutions was investigated. As a first step, zeolite encapsulated metal Salophen complexes were tested for their adsorption ability under the applied experimental conditions without adding hydrogen peroxide. The result obtained did not indicate any significant reduction in the pollutant's concentration. Hence, it can be inferred that the contribution of adsorption property of zeolite based catalyst for removing the model pollutants was insignificant.

The efficiency of zeolite based heterogeneous Fenton like AOPs and its corresponding homogeneous Fenton processes were investigated by taking the same amount of active metal complexes under similar experimental conditions. The results are depicted in Figure 4.31. It can be observed from the curves that all three metal catalysts in the heterogeneous phase have better overall catalytic efficiency than their homogenous counter parts. This can be due to the fact that steric and electrostatic constraints imposed by the walls of the zeolite framework can influence the geometry of metal complexes and hence the redox properties of the encapsulated metal complexes, making them catalytically more activity than the neat metal complexes [31, 33, 178]. However, the rate of removal of pollutants in the heterogeneous phase is lower than that observed in the homogeneous phase. This can be attributed to the reduced accessibility of H_2O_2 to the catalyst active site, as the complex is residing in the zeolite supercage.

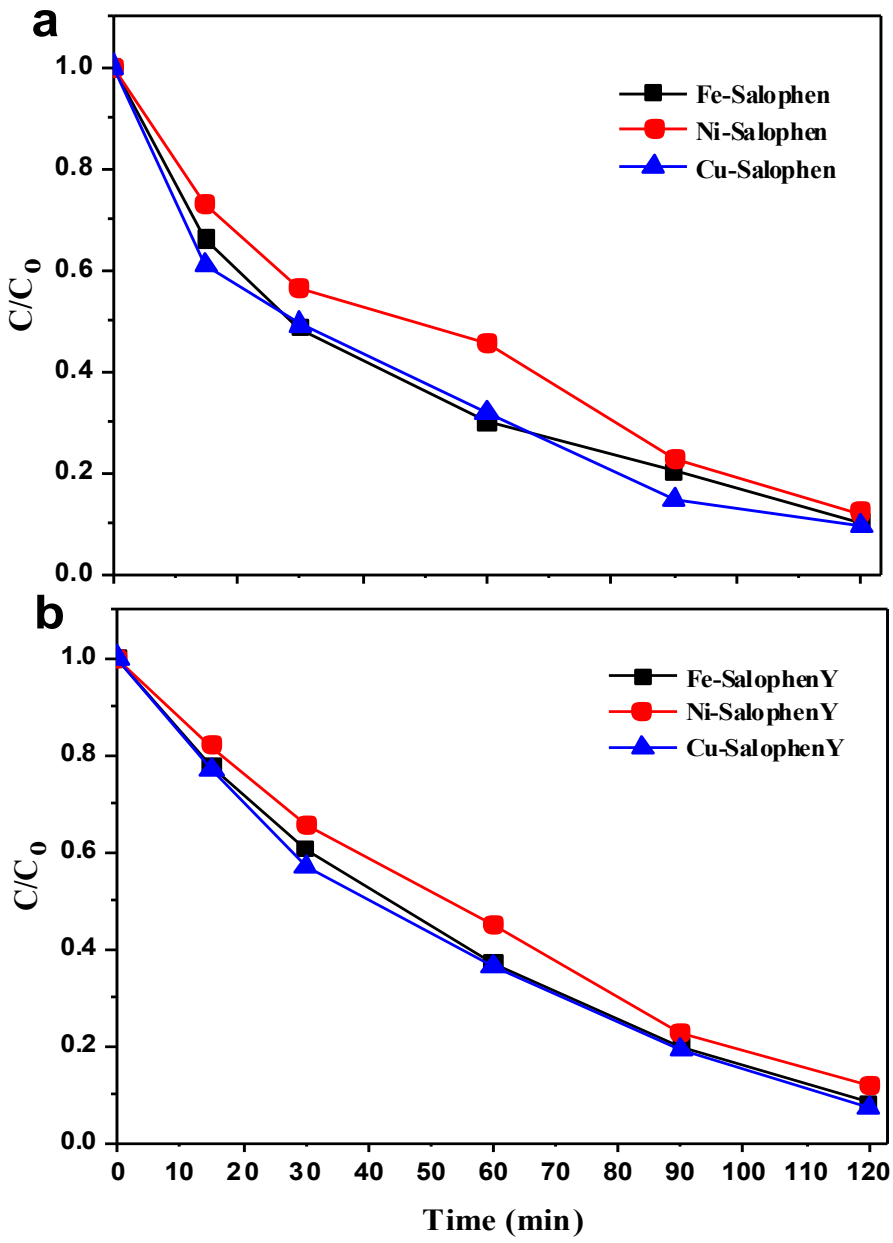

Figure 4.31 The catalytic efficiency of the synthesized metal-Salophen complex for oxidation of PCMC in **a**) homogeneous and **b**) heterogeneous Fenton like oxidation process

4.3.3.1. Effect of Hydrogen Peroxide Concentration and Catalyst Amount

Experiments to determine the effect of H_2O_2 concentration on degradation of PCMC were carried out at varying H_2O_2 concentration (25, 50, 75 and 100 mM), catalyst dosages of 0.10 g, pH of 5.3 and temperature at 29±2 °C. The initial PCMC concentration was maintained at 0.35 mM and the experiment was carried out for 120 min. The results can be found in Figure 4.32. It can be observed from the figure that the oxidative degradation of PCMC is enhanced from 79.26 to 95.89%, 64.18 to 93.12% and 75.36 to 96.86% when H_2O_2 concentrations increased from 25 mM to 100 mM for iron(III), nickel(II) and copper(II) based catalyst, respectively. This is because the generation of hydroxyl radicals in the reaction increased as the concentration of H_2O_2 was increasing, leading to fast oxidative degradation of PCMC. However, when the H_2O_2 concentration increased from 75 mM to 100 mM, degradation of PCMC was found to be constant. This observation was made during the use of all three catalysts. This can be due to the scavenging effect of hydrogen peroxide and also the generation of less reactive radicals (•OOH) as shown in the equations 4.2 and 4.3. Similar, observations have been reported, namely where higher H_2O_2 concentrations suppressed the degradation rate and efficiency of the catalyst [179- 181].

$$H_2O_2 + \bullet OH \rightarrow \bullet OOH + H_2O \quad (4.2)$$

$$HO_2\bullet + \bullet OH \rightarrow H_2O + O_2 \quad (4.3)$$

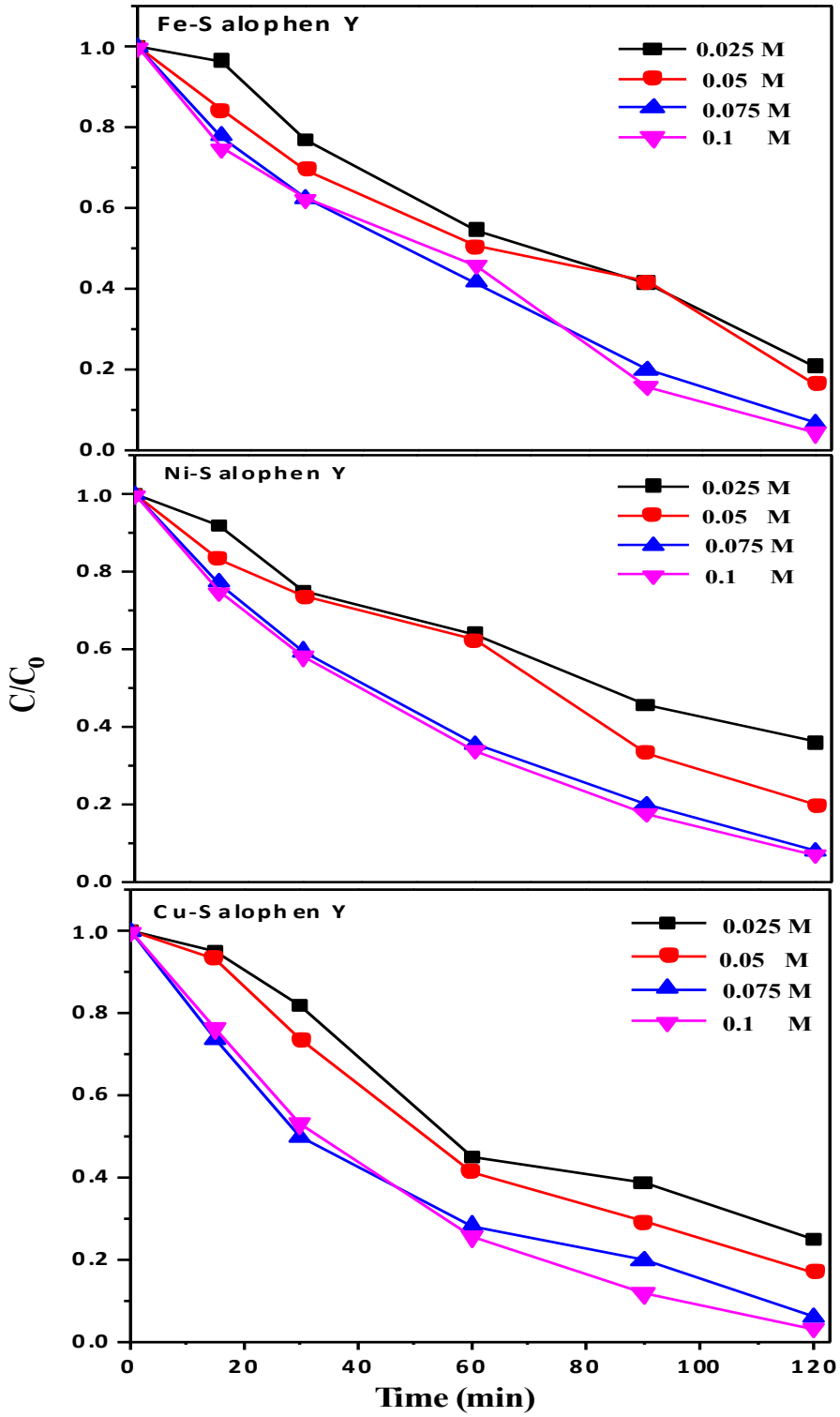

Figure 4.32 Effect of H_2O_2 concentration on degradation of PCMC **a**) iron catalyst **b**) nickel catalyst and **c**) copper catalyst: [PCMC] = 0.35 mM, [catalyst] = 0.1 g; temperature = 29±2 °C; pH = 5.3; period = 120 min

The effect of the amount of catalyst on the oxidative degradation of PCMC was investigated and the results are provided in Figure 4.33. The degradation of PCMC increased from 71.04 to 92.08%, 55.28 to 87.49% and 72.00 to 90.83% as the amount of catalyst used increased from 0.05 to 0.10 g for iron(III), nickel(II) and copper(II) based catalyst, respectively. The proportional increase in the percentage of degradation with increasing catalyst dosage was mainly due to the increasing accessibility of active sites, which leads to decomposition of more H_2O_2, resulting in increased hydroxyl radical (•OH) production. However, with further increase in catalyst to 0.125 g, the degradation of PCMC increased only marginally. Such behaviour is due to agglomeration of the catalyst leading to reduction in the surface active sites available for the reaction [182].

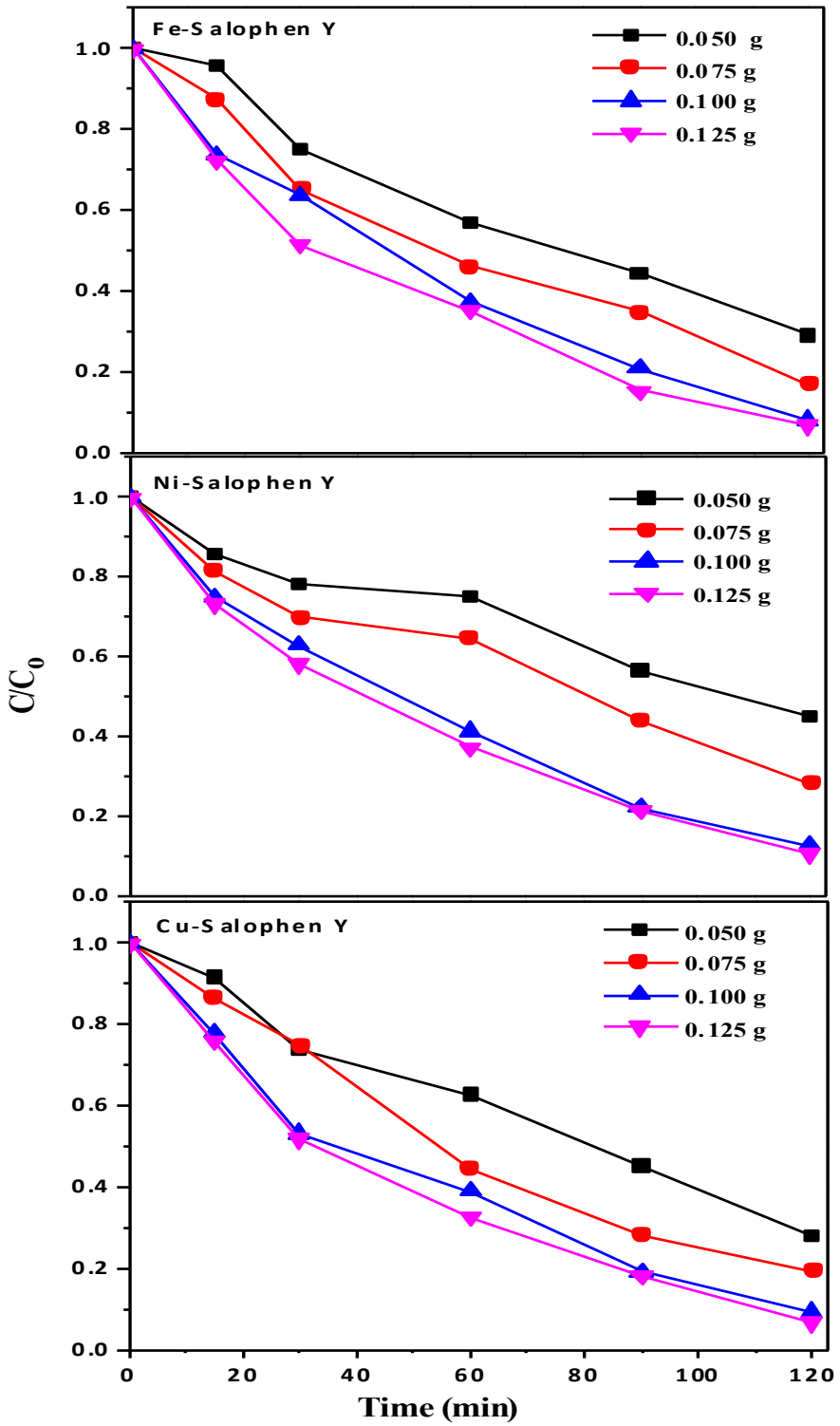

Figure 4.33 Effect of catalyst concentration on degradation of PCMC **a**) iron catalyst **b**) nickel catalyst and **c**) copper catalyst: [PCMC] = 0.35 mM, [H_2O_2] = 75 mM; temperature = 29±2 °C; pH = 5.3; period = 120 min

4.3.3.2. Effect of pH and Temperature

The effect of solution pH on the degradation of model pollutant was investigated by varying the pH of the solution (3.0, 5.0, 7.0 and 9.0). The pH was adjusted using either 0.1 N NaOH or 0.1 N H_2SO_4. The results are provided in Table 4.14. It can be observed from the Table that the pH significantly influences the degradation rate and efficiency of the catalyst. It can be seen that the degradation of PCMC increases with a decrease in the solution pH from 9.0 to 3.0. The decrease in the percentage degradation of the PCMC at higher pH could be due to rapid decomposition of H_2O_2 into molecular oxygen and H_2O and consequently the reduced generation of hydroxyl radicals. At lower pH, hydrogen peroxide and transition metal ions are more stable. Moreover, the oxidation potential of hydroxyl radicals decreases with increasing pH; 2.65-2.80 eV at pH 3.0 and 1.90 eV at pH 7.0 [183]. Hence, it can be inferred that at pH 3.0, the developed catalysts show better degradation efficiency.

To verify the effect of temperature on the oxidative degradation of PCMC, experiments were carried out at varying temperatures (25, 30, 40 and 50 °C). The results are tabulated in Table 4.14. It can be seen from the Table that increasing the temperature had a positive impact on the oxidation of PCMC by the developed catalyst. The degradation efficiency for 120 min reaction time increased as the temperature increased from 25 to 50 °C. At the higher temperature, the rate for generation of hydroxyl radical was increased, resulting in increased degradation efficiency. In addition, a higher temperature can provide more energy for the reactant molecules to overcome reaction activation energy [184].

Table 4.14 The effect of pH and temperature variation in reduction of dye concentration

pH	Percentage of reduction			Temperature (°C)	Percentage of reduction		
	Fe-Catalyst	Ni-Catalyst	Cu-Catalyst		Fe-Catalyst	Ni-Catalyst	Cu-Catalyst
3	96.65	95.99	98.17	25	79.25	66.70	79.24
5	90.56	90.08	93.46	30	92.10	89.75	92.63
7	87.07	75.35	79.54	40	97.11	93.09	94.40
9	74.36	62.34	59.61	50	98.16	98.82	98.95

4.3.3.3. Recycling and Stability of the Catalyst

The solid catalysts after completion of the experiment were filtered and the possibility of reusing the same catalyst for next batch of degradation experiments was studied. The catalysts, after filtration, were thoroughly washed with acetonitrile and ethanol solvents and then kept in an oven at 150 °C for 1 h. The dried samples were used for carrying out the next batch of degradation experiments. Reuse experiments were carried out for ten successive cycles and the results are tabulated in Table 4.15. It can be seen from the table that after three successive cycles the recovered catalysts showed only a slight reduction in the percentage degradation of PCMC. The reduction in degradation of PCMC was found to be 4.8, 5.3 and 3.7% for iron(III), nickel(II) and copper(II) based catalyst, respectively. However, when the catalysts were reused more than three times, reduction in the catalytic efficiency was observed. After 10 recycles, the decrease in degradation efficiency is found to be 14, 25 and 21 % for iron(III), nickel(II) and copper(II) based catalyst, respectively. Though reduction of catalytic activity was

observed, the heterogeneous behaviour of the catalyst was not lost as the zeolite framework obstructed the leaching of metal-Salophen complexes.

These results indicate that these catalysts can be reused at least 3-5 times without significant loss of activity. For Fe(III) and Cu(II) catalysts even after 10 cycles they retained 80% of the activity, which is significant for their possible use. Moreover, since there was no leaching of the metal complex with repeated reuses, the Fe(III) and Cu(II) complexes have the potential of finding commercial applications.

Table 4.15 Reusability of the catalyst

Sample type	Number of recycled used										
	Fresh	1st	2nd	3rd	4th	5th	6th	7th	8th	9th	10th
	Percentage of reduction (%)										
Fe-SalophenY	92.1	91.9	89.2	87.7	84.9	82.6	81.8	80.6	78.7	75.4	74.5
Ni-SalophenY	87.5	86.5	85.2	82.9	81.4	79.7	77.5	76.2	74.1	70.6	67.9
Cu-SalophenY	90.8	90.2	88.7	87.4	86.2	85.3	84.4	82.7	81.5	80.4	79.0

4.3.3.4. Deactivation Mechanism of the Catalyst

The catalysts lose some of their activity with repeated use. This loss of catalytic activity or deactivation has chemical and physical components and occurs simultaneously with the main reaction. The understanding of the phenomena of catalyst deactivation is difficult because of the diversity and complexity of the cause of deactivation. Also, the effects need to be studied under conditions close to those of the reaction process. However, reports state that the drop of catalytic activity as a function of recycling may occur due to various factors, such as leaching of metal ligand complex, site-blockage,

impurity poisoning, etc. [185, 186].

In the present investigation experiments were carried out to analyse the phenomena of catalyst deactivation during reusability studies. Various parameters including metal content in the filtrate left after treatment and BET surface area of recovered catalyst were investigated. The metal content in the collected filtrate was determined to be around 0.02 and 0.08 mg L^{-1} in the case of iron(III) and nickel(II) catalysts, respectively. In case of copper(II) based catalyst, the concentration of the metal was below the detectable limit of the instrument. In comparison to fresh catalyst, after ten successive reuse of the catalyst, the BET surface area decreased from 437 to 425 m^2 g^{-1}, 447 to 434 m^2 g^{-1} and 420 to 408 m^2 g^{-1} for iron(III), nickel(II) and copper(II) catalyst, respectively. It can be observed that the leaching of the metal ion from the catalyst during repeated use was negligible. Hence, it could be inferred that the metal leaching from the catalyst, did not bring about catalytic deactivation.

However, the BET surface area of catalyst on the other hand was found to change after successive reuse of the catalyst. Hence, the most probable reason for the deactivation of the catalyst observed was the reduction of the surface area of the catalyst due to masking or pore blockage, caused by the physical deposition of substances on active site surface part of catalyst in the zeolite cage. In literature, similar results are reported in the studies on degradation of orange II with Fe-saponite catalyst [187].

4.3.3.5. Identification of Intermediates Oxidation Products and TOC Removal

To investigate the main intermediate products in the catalytic oxidation of PCMC for each catalyst, HPLC-MS analysis of samples at different oxidation reaction time are performed. After 30 min of oxidation time, a species with m/z 124 is detected for all

catalyst, which is assigned to formation of methyl hydroquinone (Figure 7.8 in appendices). Likewise after 60 min a species with m/z 122 is observed, which can be attributed to formation of methyl-p-benzoquinone (Figure 7.9 in appendices). Formation of these species can be rationalized by assuming that initially PCMC molecule is attacked using hydroxyl radicals and giving methyl hydroquinone with loss of chloride ion and as the reaction time increases methyl-p-benzoquinone is formed. Finally the methyl-p-benzoquinone undergoes benzenic ring opening followed by oxidative degradation, leading to formation of smaller organic acids. Presence of these smaller organic acids in solution after 120 min oxidation time is confirmed by pH of the solution and TOC analysis. The pH value of the filtrate residue is below 4.0 for all catalyst and residual TOC value is 19%, 28% and 21% for the filtrate residues obtained using iron(III), nickel(II) and copper(II) catalyst, respectively. These values confirm that some smaller organic acids remained in solution after a reaction time of 120 min.

4.3.3.6. Kinetic Studies for Degradation of PCMC

Kinetic study is important for any catalytic reaction and helps in identifying the reaction pathway and rate dependence on reaction systems. In the present study, Pseudo first order model is used to describe the catalytic degradation of PCMC by the developed catalysts. This treatment is subjected to the assumption that, the rate-determining step is generation of hydroxyl radicals and this is directly related to degradation of organic pollutants. The first order reaction model could be expressed as follows (equation 4.4 & 4.5);

$$-\frac{d\left[PCMC\right]_o}{dt} = k_{obs}\left[PCMC\right] \qquad (4.4)$$

$$\ln\left(\frac{[PCMC]}{[PCMC]_o}\right) = -k_{obs}t \qquad (4.5)$$

Where [PCMC] is pollutant concentration at time t (min), and $[PCMC]_0$ is initial concentration of pollutant at time $t = 0$, k_{obs} the first order reaction rate constant and t is time. In first order reaction model, the plot of $\ln([PCMC]/[PCMC]_0)$ against t should give a linear relationship from which the constants k_{obs} can be determined. The pseudo first order rate constant, k_{obs} and linear regression coefficient (R^2) with different initial PCMC concentrations are depicted in Figure 4.34. From the graph it can be seen that the reaction rate proceeds according to pseudo first order kinetics and the rate constant (k_{obs}) decreases with increase in initial concentration of pollutants because as the initial concentration of pollutants increases the molecules aggregate on the surface of the catalyst.

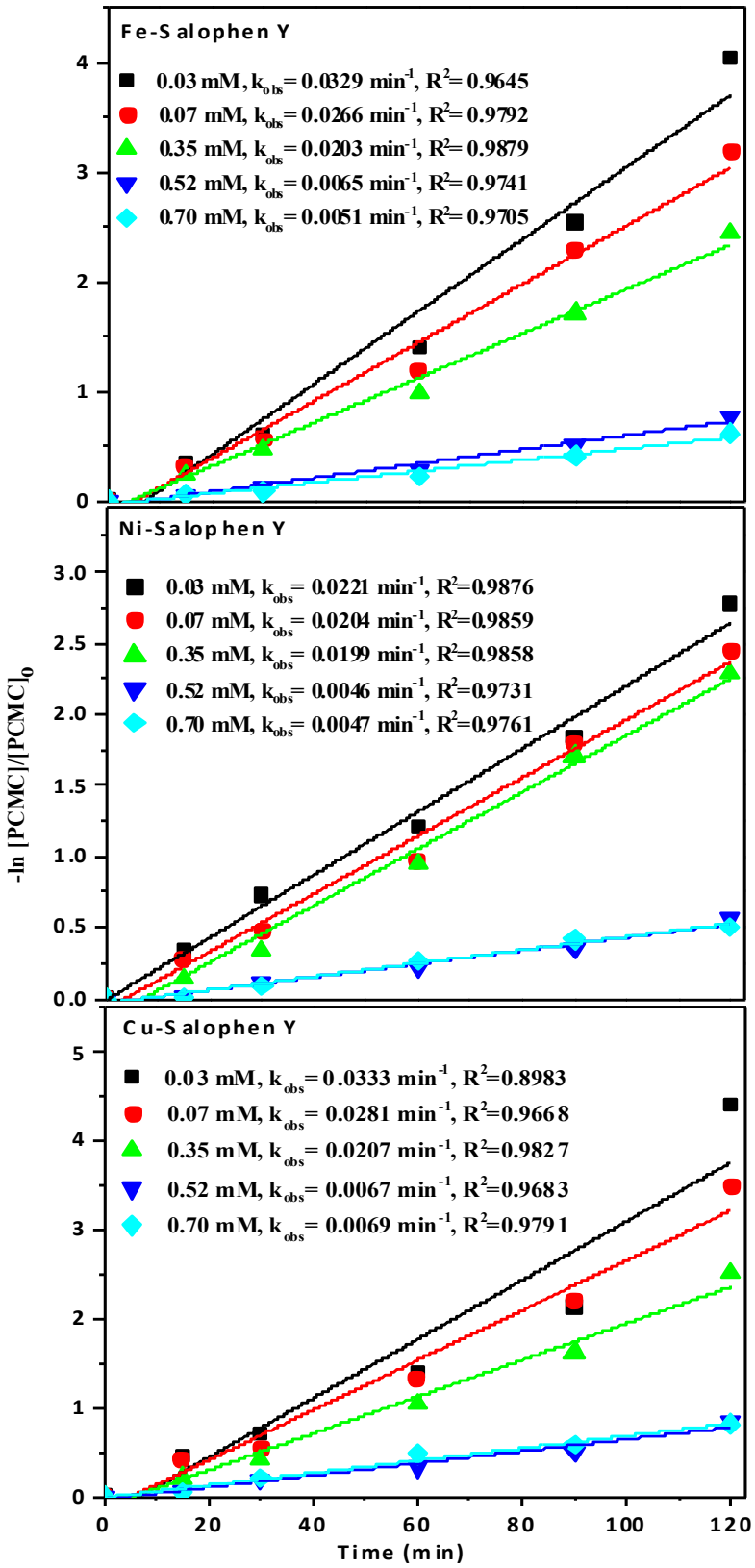

Figure 4.34 The plot of pseudo first order kinetic for degradation of PCMC using **a**) iron **b**) nickel and **c**) copper catalyst

Figure 4.34 shows that PCMC degradation using Fe(III), Ni(II) and Cu(II) catalyst is represented by the pseudo first order kinetics. This can be validated from the linear regression coefficient (R^2) values, which are 0.9752, 0.9817 and 0.9590 for Fe(III), Ni(II) and Cu(II) catalyst respectively. The rate constant (k_{obs}) for the oxidation of PCMC with Cu(II) catalyst of 0.0191 min^{-1} is higher than that observed with Fe(III) catalyst (0.0183 min^{-1}) and Ni(II) based catalyst (0.0143 min^{-1}) , which means the Cu(II) catalyst is able to degrade PCMC more rapidly. The results reveal that heterogeneous Fenton like process for degradation of PCMC follow pseudo first order pattern.

4.4. Adsorption of Acid Blue Dye and Chromium(VI) onto Cationic Surfactant Modified Zeolite

4.4.1. Characterization of Surfactant Modified Zeolite

4.4.1.1. Background

The total cation exchange capacity (TCEC) and the external cation exchange capacity (ECEC) of neat zeolite Y was measured using adsorption of ammonium acetate and TBA-Br (tetrabutyl ammonium bromide) solutions, respectively. The external surface was used to load TBA-Br because the pore size of zeolite is too small to host the cationic surfactant into the zeolite supercage. The ECEC was obtained about 0.12 g of TBA-Br g^{-1} zeolite, which accounts for 10.93% of total cation exchange capacity (TCEC) (i.e. 1.02 g of TBA-Br g^{-1} zeolite).

4.4.1.2. Structural, Morphological and Textural Properties of Materials

Figure 4.35 shows the XRD patterns of the neat zeolite, CSMZ-100 and CSMZ-200. The XRD patterns obtained for surfactant-modified zeolite are in agreement with the characteristic diffraction patterns of neat zeolites, in terms of peak positions and their relative intensities. The relative intensity of X-ray peaks for neat zeolite and modified zeolites are presented in Table 4.16. The structural parameters of the HDTMA-Br modified zeolites are comparable to that of corresponding neat zeolites, which indicate that the crystalline nature of the zeolites retained after surface modification. In contrast, a significant change in relative intensities of the peaks at 2θ are observed (Table 4.16), revealing that cation exchange reactions take place in the external surface of the zeolite via ion exchange process [184-186]. The surfactant does not only modify the surface charge zeolite but also makes the surface hydrophobic, since the hydrophilic part of

surfactant molecules is attached to the surface of the zeolite. Similar XRD results have been reported before [184].

Table 4.16 Typical X-ray peaks of neat zeolite and HDMTA-Br modified zeolites

2θ (degree)	Neat zeolite		CSMZ-100%		CSMZ-200%	
	d(Å)	I/I_{max} (%)	*d* (Å)	I/I_{max} (%)	*d*(Å)	I/I_{max} (%)
6.19	14.23	100	14.29	100	14.34	100
10.08	8.70	24	8.74	35	8.76	20
11.87	7.43	19	7.45	26	7.47	31
15.56	5.65	56	5.67	55	5.67	25
18.59	4.74	30	4.75	26	4.76	50
20.38	4.35	43	4.36	39	4.37	24
23.51	3.76	65	3.77	68	3.77	53
26.98	3.29	47	3.30	51	3.46	40
29.53	3.01	22	3.02	29	3.02	22

d: interplanar spacing and I/I_{max}: relative intensity

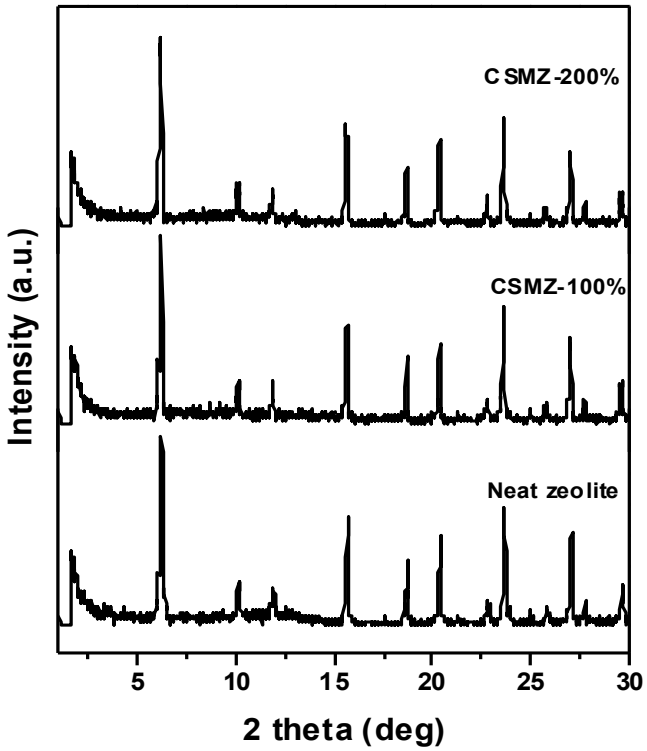

Figure 4.35 X-ray powder diffraction patterns of neat zeolite and surfactant modified zeolite

Surface morphology of neat zeolite and surfactant-modified zeolite images are obtained using high resolution scanning electron microscopy (HR-SEM). As Figure 3.36 presents, the neat zeolite exhibits well-defined shape with thin platy crystals. When the zeolite is modified with the surfactant, the platy crystals are still present; the crystal endings are however less sharp, indicating that the surfactant molecules provide a smooth surface to the zeolite crystals. Otherwise, there is no remarkable difference between CSMZ-100 and CSMZ-200 samples, since approximately same amount of surfactant efficiently is anchored to the surface of the crystals.

The surface area and pore volume of an adsorbent are significant parameters in determining its adsorption capacity as well as its adsorption performance. BET surface area of the surfactant modified zeolite dropped down from 567 $m^2 g^{-1}$, for neat zeolite, to 391 $m^2 g^{-1}$ and 221 $m^2 g^{-1}$ for CSMZ-100% and CSMZ-200%, respectively. Likewise, the pore volume is decreased from 0.32 $cm^3 g^{-2}$ (neat zeolite) to 0.26 and 0.21 $cm^3 g^{-2}$ for CSMZ-100% and CSMZ-200%, respectively. From the obtained results, it is clear that modified zeolites have lower BET surface area and pore volume than the unmodified zeolite. The decrease in the surface area and pore volume is due to the obstruction of the main channels of the zeolite by the surfactant molecules that exist at the external surface and around the pore openings (supercages) of the zeolite.

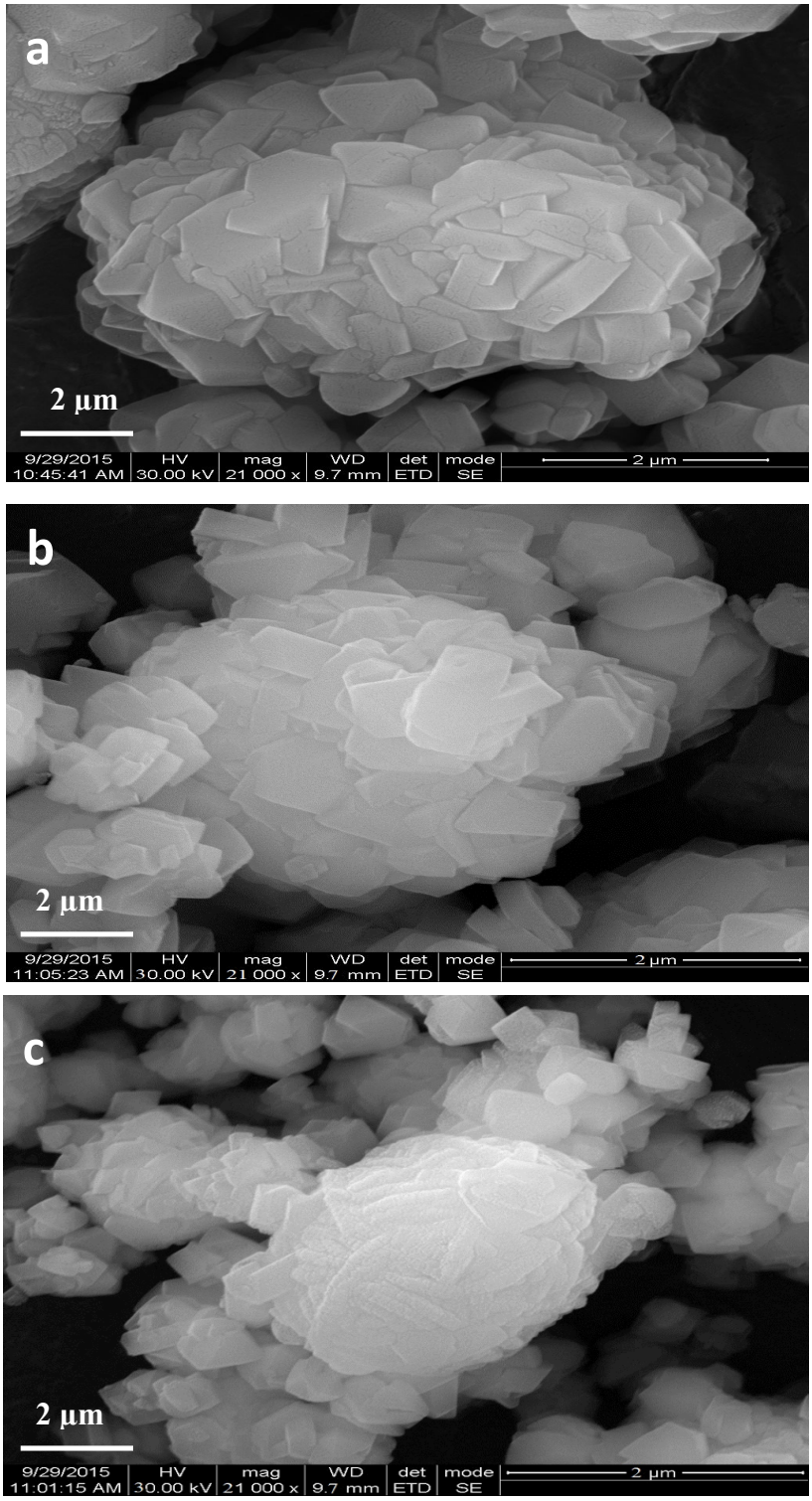

Figure 4.36 SEM morphology of **a**) neat zeolite **b**) CSMZ-100 and **c**) CSMZ-200

4.4.1.3. Spectroscopic Characterization of Surfactant Modified Zeolite

The FT-IR spectra of neat zeolite, pure HDTMA-Br, CSMZ-100% and CSMZ-200% are shown in Figure 4.37. The neat zeolite is characterized by the broad -O-H stretching and bending as well as -Si-O and -Al-O stretching and bending bands, whereby the bands peaked at 3447-3624 cm^{-1} are ascribed to O-H stretching vibration while -O-H bending vibration band occurs at 1638 cm^{-1} [191]. -Si-O stretching vibration band is observed at 1040 cm^{-1} while bands in the 400-600 cm^{-1} region are attributed to -Si-O and -Al-O bending vibration [107,177,192,193].

Major IR spectral bands of neat zeolite are also retained in the spectrum of cationic surfactant modified zeolite, which implies that there is no significant change in the zeolite framework upon modification process. The FT-IR spectrum of pure HDTMA-Br surfactant has two strong characteristic IR bands which are associated with methylene tails and alkylammonium head groups. The band around 3015 cm^{-1} is assigned to the symmetric stretching mode of the trimethylammonium head groups of CH_3-N whereas the bands around 2800-2900 cm^{-1} are ascribed to the asymmetric and symmetric stretching of methylene tail group of HDTMA-Br.

In IR spectrum of surfactant modified zeolite, besides the zeolite IR characteristic bands, additional intense absorption bands at around 2915 and 2850 cm^{-1} are observed resulting from the asymmetric and symmetric stretching vibration modes of methylene groups of the surfactant attached to the zeolite surface.

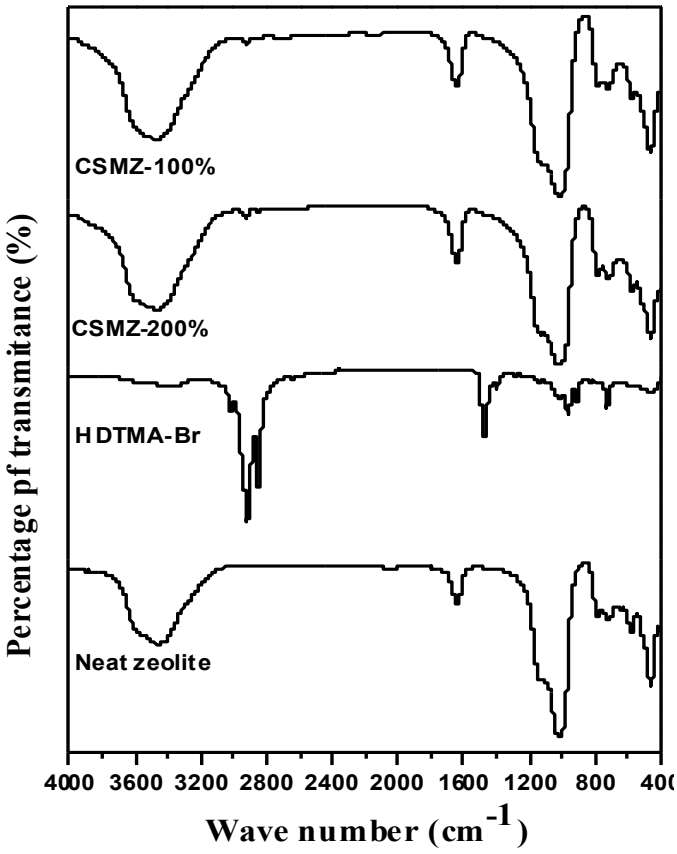

Figure 4.37 FT-IR spectrum of neat zeolite and surfactant modified zeolite

4.4.1.4. Zeta Potential Measurement

The variation of zeta potential of neat zeolite, CSMZ-100% and CSMZ-200% as a function of pH can found in Figure 4.38. As shown in the figure, neat zeolite had a negative surface charge in the pH range of 4-10. As the pH of the solution increased the surface of the zeolite became more negative, which may be attributed the deprotonation of aluminol Al-OH and silanol Si-OH groups of the neat zeolite.

The modified zeolite with 100% ECEC (CSMZ-100%) had an isoelectric point charge (IEP) at pH of 4, which, when extends to pH 6 revealed that the negative surface charge of zeolite was neutralized by HDMTA-Br surfactant with a formation of a mono layer.

For 200% ECEC (CSMZ-200%), the zeta potential value stayed positive in a wide pH range. The reversal in surface charge from neutral to positive in the vicinity of pH of 6, as compared to the neat zeolite and CSMZ-100%, appeared to be responsible for the formation of a bilayer on the external surface of the zeolite [107,177]. As the pH further increased from 8 to 10 the value of the zeta potential gradually became negative due to desorption of cationic surfactant from the zeolite surface [188].

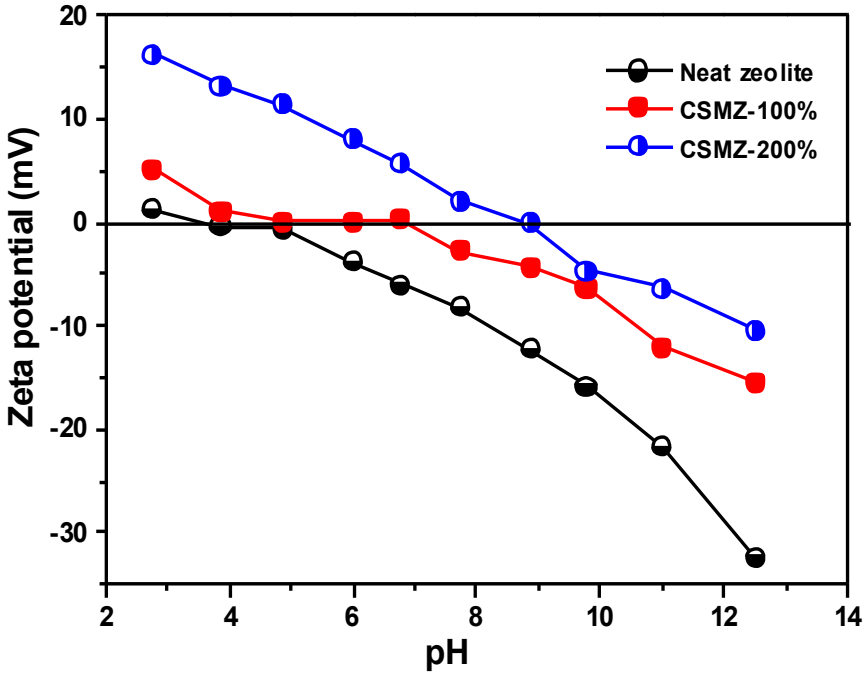

Figure 4.38 Zeta potential vs pH graph of neat zeolite and surfactant modified zeolite

4.4.1.5. Elemental Analysis

The thermogravimetric analysis curves for the neat zeolite and surfactant-modified zeolite are shown in Figure 4.39. From the figure, it can be observed that the surfactant-modified zeolite had different TGA/DTG patterns compared to that of neat zeolite. The

neat zeolite had one weight loss peak at around 120 °C, which was attributed to the loss of free water (physically adsorbed water and water between particles) from the zeolite cage. Unlike the neat zeolite Y, the surfactant modified zeolite had two weight losses: the first one, centred at c.a. 120 °C corresponding to desorption of physically adsorbed and occluded water molecules from the zeolite and the second weight loss at around 430 °C due to the decomposition of the organic surfactant adsorbed on the zeolite surface. The total mass-loss was about 4% and 7% for CSMZ-100% and CSMZ-200%, respectively. This result further corroborates the presence of the surfactant strongly attached on the zeolite surface.

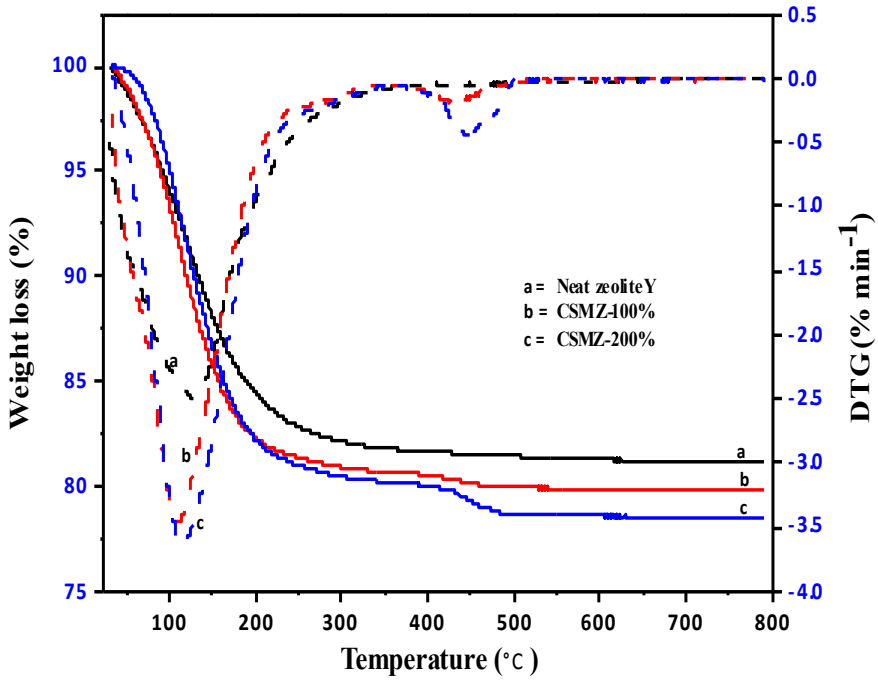

Figure 4.39 TGA profiles of neat zeolite and surfactant modified zeolite

4.3.1.6. Hydrophobicity

The hydrophobicity of the neat zeolite and surfactant-modified zeolite is tabulated in Table 4.17. As can be seen, the neat zeolite had less hydrophobicity owing to strong

interaction between zeolite and water molecules, which excluded the organic solvents. On the contrary, the monolayer surfactant modified zeolite (CSMZ-100%) had the highest hydrophobicity due to the hydrophobic alkyl groups of the surfactant covering the surface of the zeolite. The lower hydrophobicity value for the bilayer (CSMZ-200%) rather than a monolayer surfactant modified zeolite is attributed to presence of hydrophilic trimethyl ammonium head groups on the external surface of the zeolite.

Table 4.17 Percentage of hydrophobicity of neat zeolite and surfactant modified zeolite

Sample	Hydrophobicity (% weight)
Neat zeolite Y	12
CSMZ-100%	94
CSMZ-200%	89

4.4.2. Application of Surfactant Modified Zeolite for Adsorption of Azo Dyes and Chromium(VI)

4.4.2.1. Effect of Contact Time

Acquiring the optimum contact time is very important for determining the maximum possible adsorbate removal in an adsorption process. To determine the optimum contact time, 100 mL of synthetic wastewater containing 100 mg L^{-1} acid blue dye and 25 mg L^{-1} Cr(VI) were added to a 250 mL Erlenmeyer flask and equilibrated with 1.0 g of the adsorbent (CSMZ-200). The percent removal of the dye was measured as a function of time. The obtained data indicated that the removal capacity increased with an increase in contact time. A 13% removal of acid blue dye was obtained within 0.5 h and it increased to 87.3% in 6 h. In the case of Cr(VI), 5% removal was achieved in 0.5 h and that increased to 76.6% in 6 h of adsorption time. Further increase in contact

time to 24 h resulted in 91.8% and 83.8% removal of acid blue dye and Cr(VI), respectively. Further increase in adsorption time did not increase the percentage removal for both pollutants significantly. Hence, 6 h and 24 h were selected as the optimum contact time for acid blue dye and Cr(VI), respectively in further adsorption studies.

4.4.2.2. Effect of Pollutant Concentration

The rate and efficiency of adsorption is a function of the initial concentration of adsorbate, and thus it is an important parameter in studying adsorption processes. The effect of initial concentration of adsorbate was investigated while keeping other parameters constant. The concentration was varied from 25 to 150 mg L^{-1} for acid blue dye and 10 to 30 mg L^{-1} for Cr(VI). As can be observed from Figure 4.40, the percentage removal of pollutants decreased from 96.56% to 71.27% and 92.04% to 72.95% for acid blue dye and Cr(VI), respectively with increasing initial concentration. The decrease in percentage removal can be explained by the fact that adsorbents generally have limited number of active sites, which eventually become occupied (saturated) above a certain concentration of adsorbate. Likewise, the adsorption capacity of the adsorbent increased from 2.41 to 10.69 mg g^{-1} for acid blue dye and 0.92 to 2.18 mg g^{-1} for Cr(VI) with increasing initial concentration of adsorbate. The increase in the adsorption capacity of the adsorbent with increase in pollutant concentration is attributed to the higher adsorption rate and utilization of all active sites available for adsorption at higher concentration [194-196].

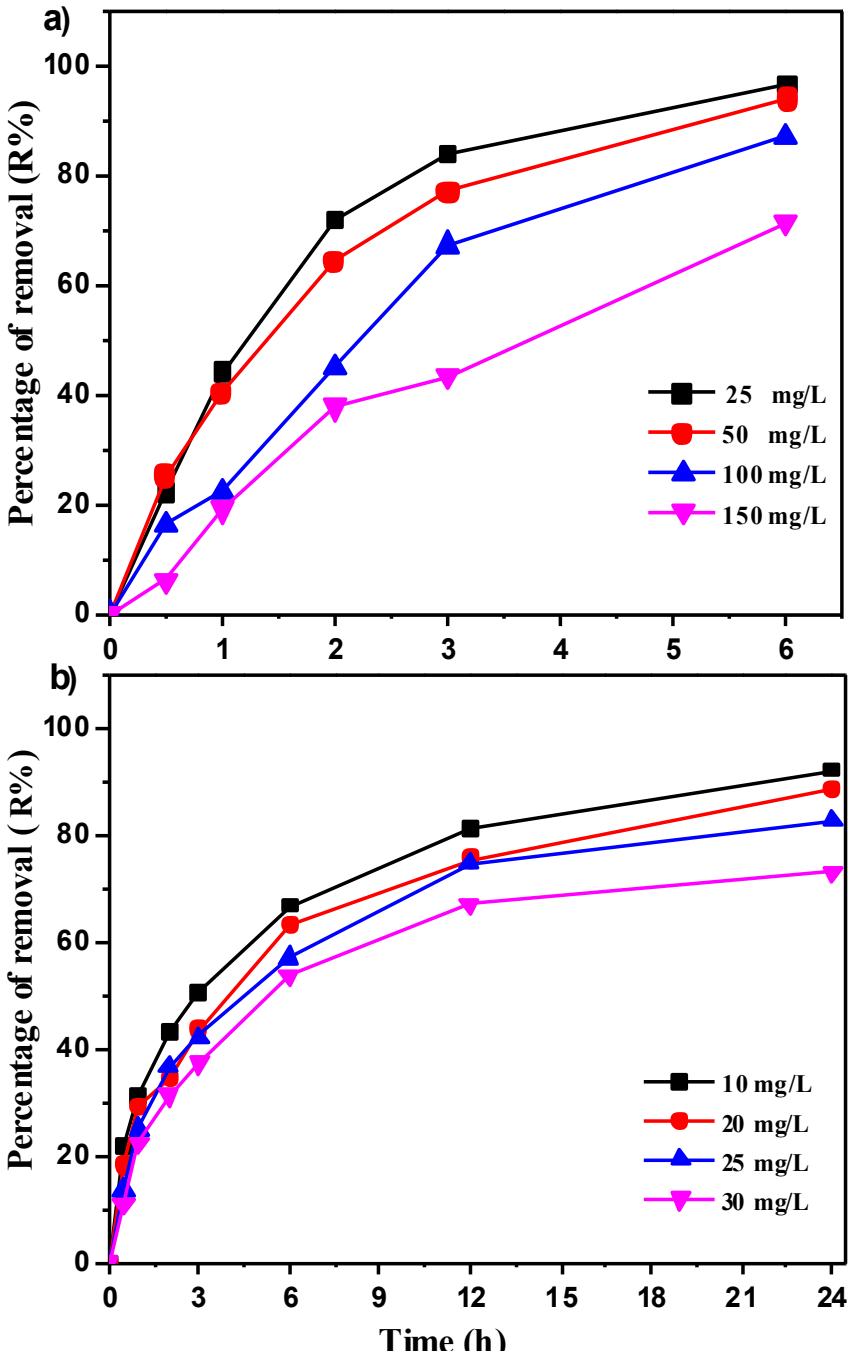

Figure 4.40 Effect of pollutant concentration for **a**) acid blue dye **b**) Cr(VI)

4.4.2.3. Effect of Adsorbent Dosage

Adsorption of acid blue dye and Cr(VI) occurs at the surface of the cationic surfactant modified zeolite, and therefore it is evident that the efficiency of adsorption depends on the quantity of adsorbent used in the adsorption process. For that purpose, the effect of surfactant modified zeolite dosage in the range of 0.25-1.5 g was investigated on the adsorption of pollutants under optimised conditions. As can be extracted from Figure 4.41, the efficiency of acid blue dye and Cr(VI) removal increased from 41.2% to 89.8% and 58.76% to 87.46%, respectively as the adsorbent increased from 0.25 to 1.5 g. The improvement of pollutant adsorption with increasing adsorbent dosage may be attributed to the increased total surface area of adsorbent and availability of more active sites for adsorption. It is important to mention that an increase in adsorbent dosage from 1.0 to 1.5 g did not lead to significant increase in the adsorption of the dye and Cr(VI); i.e. the adsorption only increase from 85.48% to 89.8% for acid blue dye and 82.26 to 87.46% for Cr(VI). This is due to an increase in adsorbent dosage exceeding a given amount may lead to adsorbent aggregation, resulting in a decrease in the total surface area of active adsorbent sites [197-199].

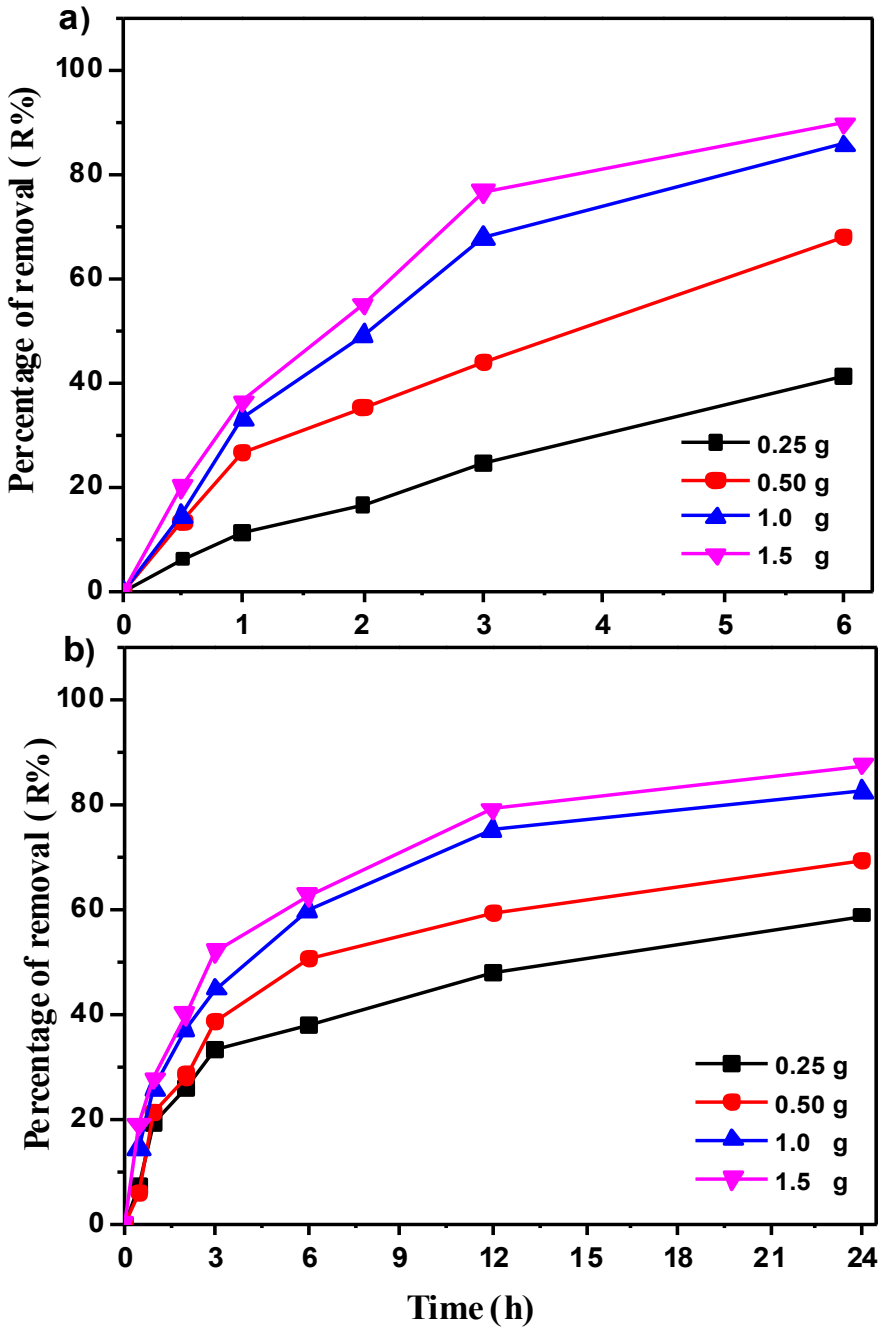

Figure 4.41 Effect of adsorbent dosage for **a**) acid blue dye **b**) Cr(VI)

4.4.2.4. Effect of Solution pH and Temperature

The removal of acid blue dye and Cr(VI) from synthetic wastewater by modified zeolite was highly dependent on the pH of the solution. As can be observed from the data in Table 4.18, the maximum removal capacities were found at acidic pH for both the pollutants. The strong dependence of the obtained removal capacity may be attributed to the electrostatic interactions between the cationic form of CSMZ surface and anionic Cr(VI) species present in the wastewater [189,199]. According to the Cr(VI) speciation diagram, the predominant Cr(VI) species in a aqueous solution are $HCrO_4^-$, $Cr_2O_7^{2-}$ and CrO_4^{2-} anions depending on the solution pH. Within the pH range of 2-7, $HCrO_4^-$ and $Cr_2O_7^{2-}$ are the predominant species, whereas at pH higher than 7, CrO_4^{2-} is the dominant species [199,200]. The improved removal of Cr(VI) at lower pH values suggests that Cr(VI) was adsorbed on the surfactant modified zeolite as either the $HCrO_4^-$ or the $Cr_2O_7^{2-}$ species. As shown in the zeta potential versus pH graph (Figure 4.38), the surface of the surfactant-modified zeolite was more positive at lower pH and negative at higher pH. Thus, anionic Cr(VI) species due to their charge are repelled by the CSMZ surface at higher solution pH. Since the CSMZ surface is positively charged at lower pH value, the anionic Cr(VI) species in wastewater was attracted to the CSMZ surface. Therefore, the obtained maximum Cr(VI) percentage removal (89.99%) and adsorption capacity (2.25 mg g^{-1}) at pH of 5 were justified. Similar adsorption trends have been reported for the removal of Cr(VI) by activated carbon [201] and organo-modified zeolite [202].

The effect of pH on the adsorption of acid blue dye was investigated and the results are tabulated in Table 4.18. Alterations in pH can lead to changes in the external surface

charge of the surfactant-modified zeolite as well as affect the degree of dissociation of the dye. At solution pH = 3, the maximum removal (94.83%) and higher adsorption capacity (9.48 mg g^{-1}) were obtained for acid blue dye. In aqueous solutions of lower pH (ca. pH = 3), the dye was in the dissociated anionic form. Consequently, there existed a strong electrostatic force of attraction exists between the positively charged adsorbent surface of the modified zeolite and the anionic dye, hence enhancing the dye uptake. However, with increase in pH, the positively charged sites of the adsorbent gradually decreased and ultimately the surface became negatively charged. Moreover, at high pH, the negatively charged hydroxyl ions (OH^-) competed with dissociated anionic dye ions, causing a decrease in adsorption of the dye from aqueous solutions.

Table 4.18 The effect of pH and temperature on percentage adsorption of acid blue dye and Cr(VI)

pH	Percentage of adsorption (%)		Temperature (°C)	Percentage of adsorption (%)	
	Acid blue dye	Cr(VI)		Acid blue dye	Cr(VI)
3	94.83	81.47	25	71.88	67.59
5	86.50	89.99	30	85.28	86.79
7	79.60	73.74	35	88.13	88.52
9	56.86	61.56	40	92.19	91.41

- The pH variation experiments were conducted at 29±2 °C and the temperature variation experiments were conducted at a pH of 5.6

The effect of temperature on acid blue dye and Cr(VI) removal efficiency was investigated by varying the temperature from 25 to 50 °C. The result is presented in Table 4.18. As it can be seen from the Table, considerable increase in percentage

removal of both pollutants was observed with increasing temperature (71.88 to 92.19% for acid blue dye and from 67.59 to 91.41% for Cr(VI)). In terms of adsorption capacities the increases were from 7.19 to 9.23 mg g^{-1} and 1.69 to 2.28 mg g^{-1} for acid blue dye and Cr(VI), respectively.

4.4.2.5. Adsorption Isotherms

Adsorption isotherms are the representation of adsorbed amount as a function of concentration at constant temperature, and hence they are useful to describe the interaction between the adsorbate and the adsorbent. Different models are available, for the purpose of obtaining important parameters that assist in interpreting the isotherm data. The parameters obtained from the adsorption isotherm models provide important information for the adsorption mechanisms, the surface properties and affinities of the adsorbent. From the several models available, the Langmuir and Freundlich isotherms were selected and used. In this study the effects of adsorption of acid blue dye and Cr(VI) at different concentrations, ranging from 20 to 50 ppm and 50 to 150 ppm respectively, were studied. The Langmuir and Freundlich adsorption isotherm are given in Equations 4.6 and 4.7, respectively:

$$\frac{C_e}{q_e} = \frac{C_e}{q_{\max}} + \frac{1}{k_a q_{\max}} \qquad (4.6)$$

$$\log q_e = \log K_f + \frac{1}{n}\log C_e \qquad (4.7)$$

where q_e (mg g^{-1}) is the amount of pollutant adsorbed per unit mass of adsorbent and C_e (mg L^{-1}) is the adsorbate concentration at equilibrium. k_a (L mg^{-1}) and K_f (L mg^{-1}) are constants of the Langmuir and Freundlich models, respectively. q_{max} (mg g^{-1}) is the

maximum amount pollutant adsorbed in the Langmuir model and $1/n$ is the heterogeneity factor in Freundlich models.

The Langmuir constants k_a and q_{max} can be determined from the linear plot of C_e/q_e versus C_e, and the Freundlich constants K_f and $1/n$ were determined from the linear plot of $\log q_e$ versus $\log C_e$.

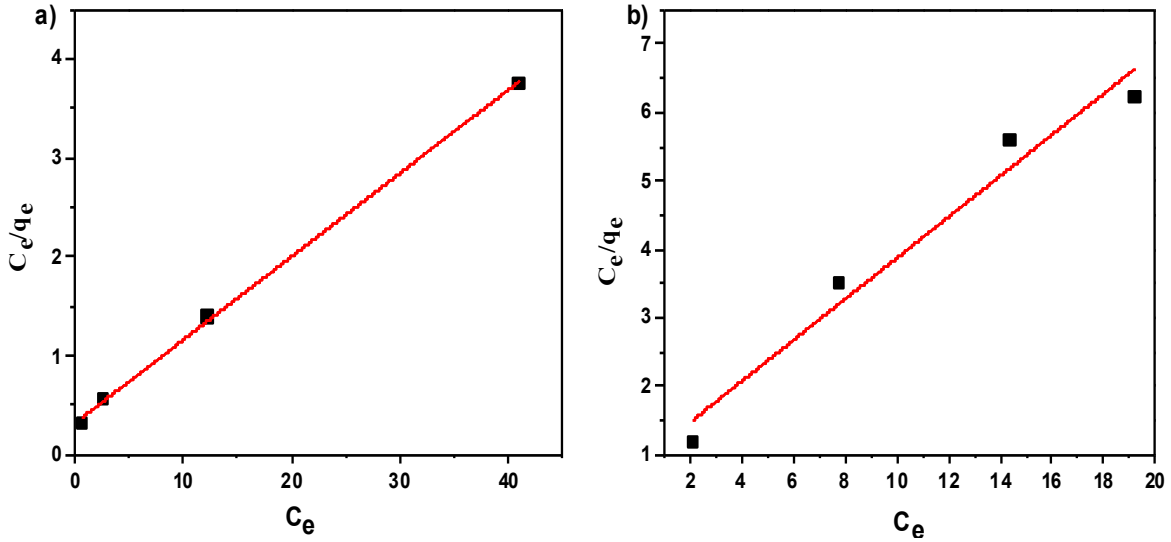

Figure 4.42 Langmuir isotherm plot for adsorption of **a**) acid blue dye **b**) Cr(VI)

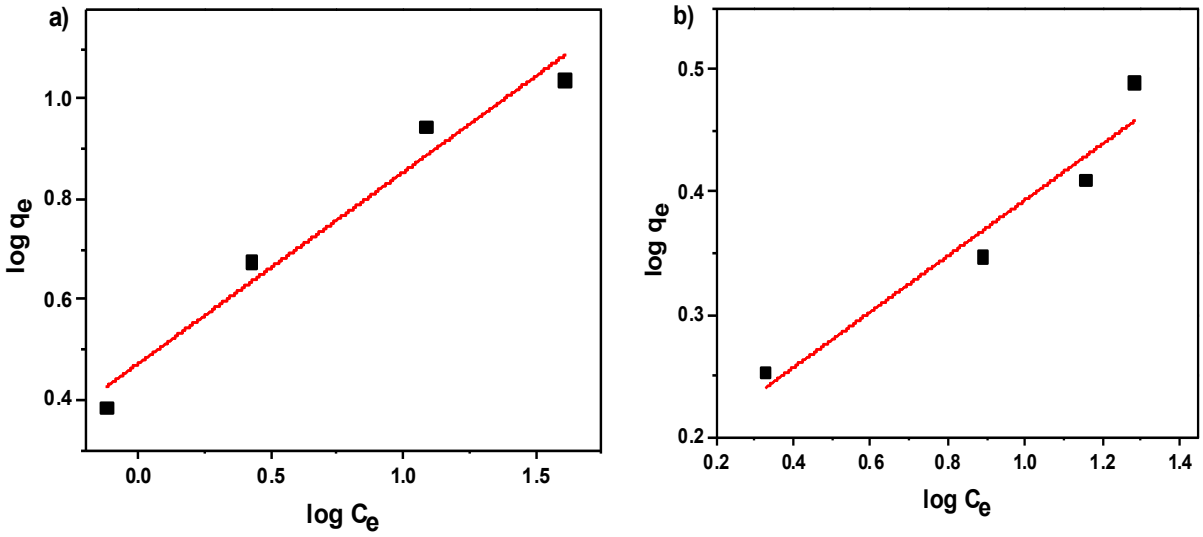

Figure 4.43 Freundlich isotherm plot for adsorption of **a**) acid blue dye **b**) Cr(VI)

Table 4.19 Isotherm constants for adsorption of acid blue dye and chromium(VI) onto surfactant modified zeolites

Adsorbant	Langmuir isotherm				Freundlich isotherm			
	K_a (Lmg^{-1})	q_{max} ($mg\ g^{-1}$)	R_1^2	SD_1 (%)	K_F ($L\ mg^{-1}$)	*1/n*	R_2^2	SD_2 (%)
Acid blue dye	0.27	11.83	0.9993	8.95	2.41	0.47	0.8967	18.6
Cr(VI)	0.34	3.33	0.9687	12.47	1.69	0.16	0.9902	7.44

Values of Langmuir and Freundlich constants were calculated from the plots in Figure 4.42 and 4.43, respectively and the results tabulated in Table 4.19. The correlation coefficient R^2 values, and the standard deviation SD show that Langmuir and Freundlich isotherm models can sufficiently describe the adsorption data for acid blue dye and Cr(VI), respectively.

Moreover, the fundamental characteristics of the Langmuir isotherm can be expressed in terms of a dimensionless constant known as the separation factor R_L [203, 204].

$$R_L = \frac{1}{(1 + C_o k_a)} \qquad (4.8)$$

where C_0 represent the highest initial concentration of adsorbate ($mg\ L^{-1}$). R_L can take values between 1 and zero. The value of R_L indicates the situation of the isotherm to be either linear ($R_L = 1$), favourable ($0 < R_L < 1$), or irreversible ($R_L = 0$). In this study the value of R_L was found to be close to zero ($R_L = 0.024$) indicating that the adsorption of acid blue dye onto the surfactant modified zeolite was exceedingly favourable.

Since adsorption of Cr(VI) is described better with the Freundlich isotherm model, the heterogeneity parameters (1/n) were calculated from the linear plot. The value of 1/n

smaller than 1 or lies between one and ten, then the adsorption is considered as a favourable adsorption process [205, 206]. The value of 1/n for Cr(VI) adsorption was 0.1659 (n = 6.02), indicating that adsorption of Cr(VI) onto the surfactant modified zeolite was a favourable adsorption process.

4.4.2.6. Kinetic Modelling Studies

In order to design a treatment plant, it is important to be able to predict the rate at which pollutants are removed from the wastewater. In this regard, adsorption kinetics of acid blue dye and Cr(VI) onto CSMZ were investigated, and pseudo first order as well as pseudo-second order models were used to fit the experimental data. The kinetic model equations 4.9 and 4.10 [207] were used to evaluate the kinetic parameters. The obtained kinetic parameters for acid blue dye and Cr(VI) adsorption onto surfactant-modified zeolite are presented in Table 4.20.

$$\log(q_e - q_e) = \log q_e - \frac{k_1}{2.303}t \qquad (4.9)$$

$$\frac{t}{q_t} = \frac{1}{k_2 q_e^2} + \frac{1}{q_e}t \qquad (4.10)$$

Where q_e (mg g^{-1}) is the amount of dye adsorbed at equilibrium, q_t (mg g^{-1}) the amount of dye adsorbed at time t. k_1 (min^{-1}) and k_2 (g mg^{-1} min^{-1}) represent the pseudo first order and pseudo second order rate constants, respectively. The values of k_1 and q_e are obtained from the slope and intercept from the plot of $\log(q_e - q_t)$ versus t, considering pseudo first order model, respectively. Similarly, the values of q_e and k_2 were respectively determined from the slope and intercept of a plot of t/q_t versus t, for the pseudo second order kinetic model.

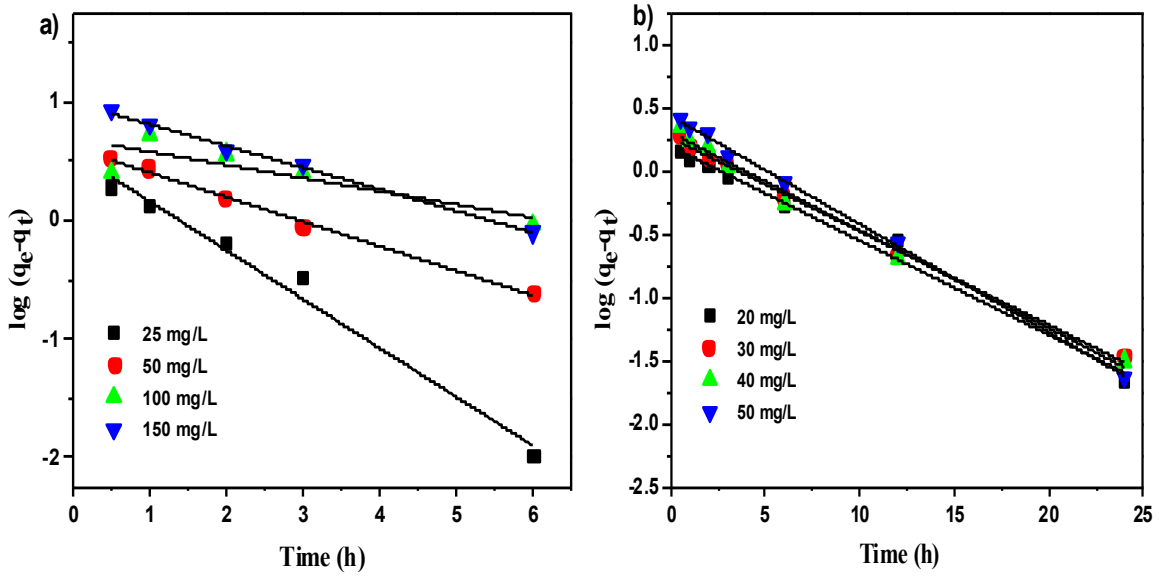

Figure 4.44 Pseudo first order kinetic plot for adsorption of **a**) acid blue dye **b**) Cr(VI)

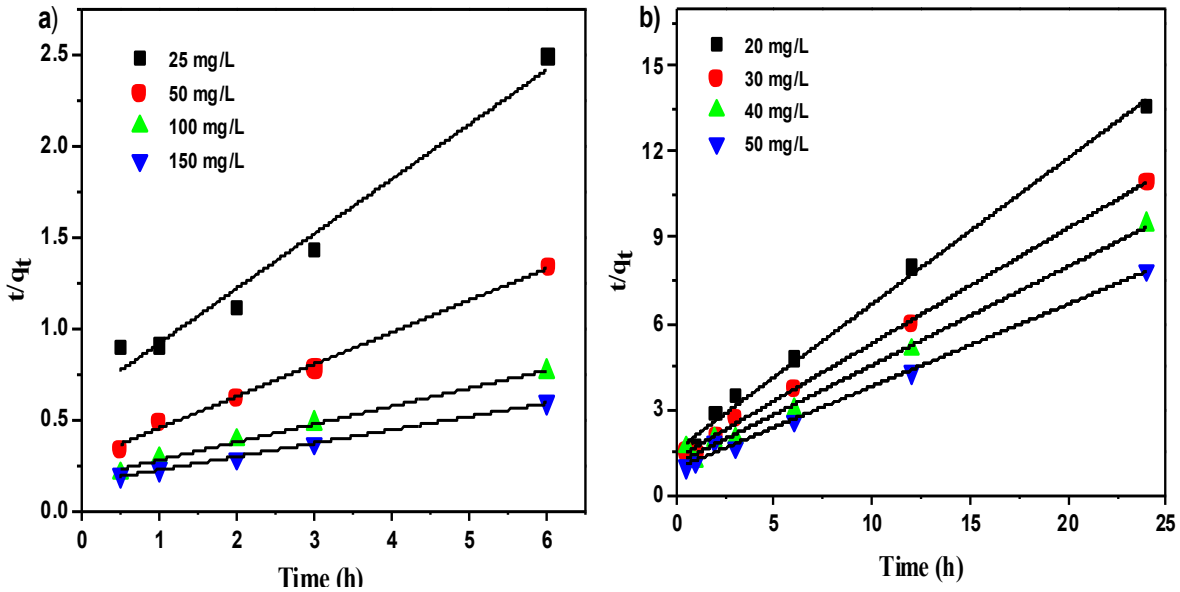

Figure 4.45 Pseudo second order kinetic plot for adsorption of **a**) acid blue dye **b**) Cr(VI)

Table 4.20 Kinetic parameters for adsorption of acid blue dye and Cr(VI) onto surfactant-modified zeolites

		Acid blue dye					
		Pseudo first order			Pseudo second order		
Co (mgL^{-1})	$q_{e1,exp}$ ($mg\ g^{-1}$)	k_1 (min^{-1})	$q_{e2,cal}$ ($mg\ g^{-1}$)	R_1^2	k_2 ($g\ m\ g^{-1}\ min^{-1}$)	$q_{e1,cal}$ ($mg\ g^{-1}$)	R_2^2
25	2.42	0.9508	3.75	0.9787	0.0555	3.33	0.9691
50	4.73	0.4779	4.08	0.9946	0.0085	5.70	0.9933
100	8.77	0.2570	4.92	0.8370	0.0017	10.15	0.9929
150	10.90	0.4215	9.84	0.9946	0.0008	13.65	0.9961
Cr(VI)							
Co (mgL^{-1})	$q_{e2,exp}$ ($mg\ g^{-1}$)	k_1 (min^{-1})	$q_{e2,cal}$ ($mg\ g^{-1}$)	R_1^2	k_2 ($g\ m\ g^{-1}\ min^{-1}$)	$q_{e2,cal}$ ($mg\ g^{-1}$)	R_2^2
20	1.78	0.4477	1.56	0.9869	0.4093	1.96	0.9929
30	2.22	0.6025	1.82	0.9961	0.2071	2.49	0.9983
40	2.56	0.6974	2.01	0.9879	0.1303	2.91	0.9911
50	3.08	0.9993	2.72	0.9974	0.0768	3.49	0.9947

The pseudo first order and second order kinetic parameters, including k_1, k_2, q_{e1}, q_{e2} and the correlation coefficients for the fit (R_1^2 and R_2^2) of acid blue dye and Cr(VI) were obtained from the plots (Figures 4.44 and 4.45). The data are summarised in Table 4.20. It can be seen from the table that the experimental q_e values are in good agreement with the calculated ones for both pollutants using the pseudo second order kinetic model. Moreover, the correlation coefficients (R^2) for the pseudo second order kinetic model is closer to unity for acid blue and Cr(VI) pollutants than the correlation coefficients for the pseudo first order kinetic model. It is therefore concluded that kinetics of adsorption of acid blue dye as well as Cr(VI) on to the modified zeolite obey the pseudo second order kinetic model.

4.5. Application of Synthesized Catalysts and Surfactant Modified Zeolite for Tannery Wastewater Application

Environmental pollution due to different types of industrial activities is one of the vital problems presently faced globally. The increasing awareness of people towards conservation of the environment leads to stringent environmental legislations. In the present scenario, there are many types of industrial activities and they produce their own particular combination of pollutants. The industrial wastewater often contains highly toxic compounds like phenol and its derivatives, azo dyes and heavy metals. Leather processing industries are the main source of those types of environmental pollutants. Hence, treatment and disposal of industrial wastewater containing toxic phenolic pollutants have become a serious concern [5-7]. These hazardous compounds cause severe damage to the ecosystem and humans due to their carcinogenic and mutagenic properties. In this regard, advanced oxidation processes (AOPs) are reported as an efficient treatment technique to remove resistant, toxic and poorly biodegradable pollutants from wastewater [70-72].

The prepared catalysts were tested for their catalytic efficiency for oxidation of real wastewater. Owing to effluent water from tanning industries often being very complex, it is almost impossible to characterize all types of constituents present in the effluent. Therefore, in this study the efficiency of the catalyst with regard to the total organic pollutants chemical oxygen demand (COD) and total organic carbon (TOC) parameters were monitored.

As observed from Table 4.21, oxidation of wastewater using iron(III), nickel(II) and

copper(II) salen catalyst yielded 73%, 62% and 68% reduction in the COD of effluent water and 82%, 69% and 76% TOC removal, respectively. The iron(III) and nickel(II) (2,2-bipyridine) (1,10-phenanthroline) catalyst better catalytic efficiency than salen based catalyst for the oxidation of tannery wastewater. The COD reduction obtained for iron(III) and nickel(II) catalyst was about 69% and 61%, respectively whereas the TOC reduction was 72% for iron(III) and 66% for nickel(II) (bipy)(phen) complex based catalyst.

The highest pollutant removal efficiency was observed for the N,N′-disalicylidene-1,2-phenylenediamine or Salophen ligand based catalysts. The COD reduction observed for iron(III), nickel(II) and copper(II) Salophen complex was about 81%, 70% and 76%, respectively. Likewise, the percentage of TOC removal was about 88%, 74% and 84% for iron(III), nickel(II) and copper(II) Salophen catalyst, respectively.

Among all the catalysts investigated, catalysts based on zeolite encapsulated Fe(III) salen complex, Fe(III)(bipy)(phen) complex and Fe(III) Salophen complex, yielded high catalytic efficiency in reducing COD and TOC of the tannery wastewater. This result is in good agreement with the results obtained during optimization studies for each of the Fe(III), Ni(II) and Cu(II) salen, (bipy)(phen) and Salophen ligand complex based catalysts. Nevertheless, these catalysts exhibited lower catalytic efficiency for oxidation of tannery wastewater when compared to synthetic wastewater. The reason for this may be the possible blockage of the active sites on the surface of the catalyst through suspended solids generated from the various chemicals employed throughout for the tanning process.

Table 4.21 Oxidation of tannery wastewater using catalyst based on Fe(III), Ni(II) and Cu(II) complexes of salen, (bipy)(phen) and Salophen ligand, encapsulated into zeolite Y supercage

Catalyst type	Type of analysis	
	Chemical oxygen demand (COD) in mg L^{-1}	Total organic carbon (TOC) in mg L^{-1}
Fresh wastewater	21512	641.2
Fe(III) salen	5808	115.4
Ni(II) salen	8175	198.8
Cu(II) salen	6884	153.9
Fe(III) (bipy) (phen)	6669	179.5
Ni(II) (bipy) (phen)	8390	218.0
Fe(III) Salophen	4088	76.9
Ni(II) Salophen	6454	166.7
Cu(II) Salophen	5163	102.6

A catalyst based on Salophen metal complexes exhibited a higher catalytic efficiency than salen and the mixed ligand (bipy and phen) based complexes. This is attributed to the stabilizing effect of the complex through the electrophilic benzene ring, which is attached to the two nitrogen atoms in the N,N′-disalicylidene-1,2-phenylenediamine (Salophen) ligands. In addition, the attachment of two different elements (i.e. nitrogen and oxygen) to the central metal ion may be another factor for the observed enhanced reactivity of catalysts based on N,N′-disalicylidene-1,2-phenylenediamine (Salophen) ligand metal complexes than N,N′-ethylenebis (salicylimine) based complexes and

iron(III) and nickel(II) (2,2-bipyridine) (1,10-phenanthroline) complexes.

Further, the surfactant-modified zeolite (SMZ) was investigated for adsorption properties on tannery wastewater and the results obtained are presented in Table 4.22. As shown in Table 4.22, adsorption of pollutants onto cationic surfactant modified zeolite (CSMZ) resulted in 64% and 78% COD and TOC removal, respectively. With regards to Cr(VI) adsorption, 78% of Cr(VI) was adsorbed by the surfactant-modified zeolite. Similarly, the efficiency of removal of organic matter and Cr(VI) from the tannery wastewater was less than that observed for synthetic wastewater containing only dye and Cr(VI), which was attributed to the presence of suspended solid in the wastewater.

In summary, the presence of suspended solid is assumed to be the main reason for the decrease in efficiency of surfactant-modified zeolite for adsorption of organic and Cr(VI) pollutants from tannery wastewater.

Table 4.22 Adsorption of tannery wastewater onto cationic surfactant modified zeolite (CSMZ)

Adsorbent material	Type of analysis		
	Chemical oxygen demand (COD) in mg L^{-1}	Total organic carbon (TOC) in mg L^{-1}	Cr(VI) in mg L^{-1}
Fresh wastewater	21512	641.2	1.37
CSMZ-200%	7744	141.1	0.31

5. Conclusions

The heterogeneous catalysts based on iron(III), nickel(II) and copper(II) complexes with three different ligands such as N,N′-ethylenebis(salicylimine), mixed ligand of 2,2′-bipyridine and 1,10-phenanthroline and N,N′-disalicylidene-1,2-phenylenediamine were prepared in this study employing ship-in-a-bottle method. The effectiveness of the method for encapsulation of the metal complex in the supercages of zeolite Y is confirmed using X-ray powder diffraction, BET surface area and pore volume, FT-IR spectroscopy, thermo-gravimetric, elemental and electron paramagnetic resonance analysis.

In addition, computational studies on neat metal complexes and zeolite encapsulated iron(III) and nickel(II) mixed ligand complexes of 2,2'-bipyridine and 1,10-phenanthroline and iron(III), nickel(II) and copper(II) complexes of N,N-disalicylidene-1,2-phenylenediamine or Salophen ligand also corroborated the experimental observed results, i.e. the successful encapsulation of the metal complexes in the zeolite cage.

Furthermore, the synthesized catalyst based on iron(III), nickel(II) and copper(II) N,N′-ethylenebis (salicylimine) or salen complex was applied to the oxidation of synthetic wastewater containing acid blue 113 dyes. Maximum colour removal efficiency was achieved by using iron(III), nickel(II) and copper(II) catalyst with 0.1 M H_2O_2, 0.15 g catalyst dosage, pH of 2 and 50 ºC. Moreover, it was shown that zeolite encapsulated iron(III) salen, nickel(II) salen and copper(II) salen complexes can be reused more than ten times without any significant loss in their catalytic activity.

In addition, NaY zeolite encapsulated iron(III) and nickel(II) mixed ligand complexes

of 2,2'-bipyridine and 1,10-phenanthroline were found to be active catalysts for the decomposition of hydrogen peroxide and consequently can be used for the efficient oxidation of OPP.

The heterogeneous catalysts based on iron(III), nickel(II) and copper(II) N,N′-disalicylidene-1,2-phenylenediamine or Salophen complexes were applied for the oxidation of a model pollutant of 4-chloro-3-methyl phenol (PCMC). Maximum removal efficiencies of 99, 87 and 96% were achieved by using iron(III), nickel(II) and copper(II) catalyst with 0.1 M H_2O_2, 0.15 g catalyst dosage, pH of 2 and 50 °C. These synthesized catalysts efficiently oxidized 4-chloro-3-methyl phenol (PCMC) with the generation of methyl hydroquinone and methyl-p-benzoquinone as intermediate oxidation products. With regard to kinetics, a pseudo first order kinetic model was found to be the most suitable for describing the degradation of PCMC using a heterogeneous Fenton like advanced oxidation process.

Finally, modifying the surface of zeolite with HDMTA-Br cationic surfactant revealed that the hydrophilic nature and anionic charge of the neat zeolite was altered. The characterization results obtained from X-ray powder diffractograms (XRD), Fourier transform infrared spectroscopy (FT-IR), high resolution scanning electron microscopy (HR-SEM), BET surface area and pore volume, thermos-gravimetric analysis (TGA), zeta potential and hydrophobicity, verified the successful formation of an alkyl chain bilayer on the surface of the surfactant modified zeolite. This study indicates that HDMTA-Br modified zeolite with bilayer coverage is a potentially effective adsorbent for acid blue dye and Cr(VI). The adsorption experimental results showed that using the cationic surfactant modified zeolite as an adsorbent material both anionic inorganic

(i.e. Cr(VI)) and organic pollutants (i.e. acid blue dye) could be removed from the composite synthetic wastewater. Moreover, the adsorption isotherms for adsorption of acid blue dye and Cr(VI) onto surfactants modified zeolite are in good agreement with the Langmuir isotherm and Freundlich isotherm models respectively. The kinetics of adsorption was found to follow the pseudo second order kinetic model.

6. References

1. J.J.Berzelius, Årsberättelsen om framsteg i fysik och kemi, Royal Swedish Aca. of Sci.**1835**
2. B.Lindstrom, L.pettersson, CATTECH. **2003**, 7, 130
3. E.V.Kuznetsova, L.A.Sarinov, L.A.Vostrikova, V.N. Parmon, Appl. Catal. B-Environ. **2004**, 51, 165
4. M.I.Pariente,F.MartInez,J.A.Melero,J.A.Botas,T.Velegraki,N.P.Xekoukoulotakis, D.Mantzavinos, Appl. Catal. B: Environ. **2008**, 85, 24
5. A. Asfaw, M. Sime, F. Itanna: Int. J. Sci. and Res. Publications. **2012**, 2, 1
6. D. Rameshraja and S.Suresh, Int.J.Environ.Res. **2011**, 5(2), 349
7. H. Ozgunay, S.Colak, M.M. Mutlu, F.Akyuz. Polish J. of Environ. Stud. **2007**, 16 (6), 867
8. J.Smidt, W.Hafner, R.Jira, J.Sedlmeier, R.Ruttinger, H.Kojer, Angew. Chem. Int. Ed. **1959**, 71, 176
9. J. Smidt, W. Hafner, R. Jira, J. Sedlmeier, A. Sabel, Angew. Chem. Int. Ed. **1962**, 1, 80
10. E. Krimura, A.Sakonaka, R. Machida, J. Am.Chem. Soc. **1984**, 104
11. H.C. Sutton, C.C.Winterbourn, Free Rad. Bio. Med. **1989,** 6, 53
12. M.H. Robbins, R.S. Drago, J. Catal. **1997**, 170, 295
13. T. Watanabe, K. Koller, K. Messner, J. Biotechnol. **1998**, 62, 221
14. A.H. Gemeay, I.A. Mansour, R.G. El-Sharkawy, A.B. Zaki, J. Mol. Cata. **2003**, 193, 109

15. V.Shah, P.Verma, P.Stopka, J.Gabriel, P.Baldrian, F. Nerud, Appl. Catal. B-Environ. **2003**, 46, 287

16. S.H. Bossmann, E. Oliveros, S. Gob, M. Kantor, A. Goppert, L. lei, P.L. Yue, A.M. Braun, J. Water Sci. Technol. **2001**, 44, 257

17. M.R. Dhananjeyan, E. Mielzcarski, K.R. Thampi, P. Buffat, M. Bensimon, A. Kulik, J. Mielcarski, J. Kiwi, J. Phys. Chem. B. **2001**, 105, 12046

18. A. Bozz, T. Yuranova, E. Mielzcarski, J. Mielzcarski, J. Mielzcarsi, P.A. Buffat, P. Latis, J. Kiwi, Appl. Catal. B: Environ. **2003**, 42, 289

19. R.Arora, I. Bhati, P. B. Punjabi, V.K. Sharma, J. Chem. Pharm. Res. **2010**, 2, 1

20. Z. Yaping and H. Jiangyong, Appl. Catal.B: Enviro. **2008**, 78, 250

21. F. A. Carey and R. J. Sundberg, Advanced Organic Chemistry, Part A: Structure and Mechanisms, Springer Science, New York, 5th edition, **2007**, pp. 965-988

22. J. Herney-Ramirez, A. M. Vicente, L. M. Madeira, Appl. Catal. B: Enviro. **2010**, 98, 10

23. G.A.Mansoori, T.R.Bastami, A.Ahmadpour, Z. Eshaghi, Annual Review of Nano Research, **2008,** 2, 1

24. C. A. Ríos and L.Y.Vargas, Earth and Enviro.Sci. **2011**, 363, 45

25. L.F. Liotta, M. Gruttadauria, G. Di Carlo, G. Perrini, V. Librando, J. Haza.Mater. **2009**, 162, 588

26. S. Prasenjit, K.T. Dhermendra, J. Behari, J.World Appl.Sci. **2008**, 3, 417

27. O.Hernandez-Ramirez and S.M. Holmes, J. Mater. Chem. **2008**,18, 2751

28. M.Aleksic, N.Koprivanac, A. Loncaric Bozic, H.Kusic, Chem.Bio chem Eng. **2010**, 24, 309

29. C.J.Winscom and W. Lubitz, Stud. Surf Sci. and Catal. **1982**, 12, 15
30. P. Chen, B. Fan, M. Song, C. Jin, J. Ma, R. Li, Catal. Commun. **2006**, 7, 969
31. M. Salavati-Niasari, J. Mol. Catal. A: Chem. **2006**, 245, 192
32. M.Jafarian, M.Rashvand avei, M. Khakali, F. Gobal, S. Rayati, M.G. Mahjani, J.Phys. Chem. C, **2012**, 116, 18518
33. K.K. Bania, R.C. Deka, J. Phys. Chem. C, **2012**, 116, 14295
34. R.Grommen, P.Manikandan, Y.Gao, T.Shane, J.J.Shane, R.A.Schoonheydt, B.M. Weckhuysen, D. Goldfarb, J. Am. Chem. Soc. **2000**, 122, 11488
35. M.R. Maurya, S.J.J. Titinchi, S. Chand, J. Mol. Catal. A: Chem. **2004**, 214, 257
36. R. Abraham, K.K.M. Yusuff, J. Mol. Catal. A: Chem. **2003**, 198, 175
37. C. Jin, W. Fan, Y. Jia, B. Fan, J. Ma, R. Li, J. Mol. Catal. A: Chem. **2006**, 249, 23
38. S.M. Drechsel, R.C.K. Kaminski, S. Nakagaki, F. Wypych, J. Colloid Interface Sci. **2004**, 27,138
39. A.F. Cronstedt, Akad. Handl. Stockholm, **1756**, 17, 120
40. A. F. Cronstedt. Svenska Vetenskaps Akademiens Handlingen Stockholm, **1756**, 18
41. A. Damour, Ann. Mines, **1840**, 17, 191
42. R. M. Barrer and D. W. Riley. J. Chem. Soc. **1948**, 133, 23
43. A. Dyer. An Introduction to Zeolite Molecular Sieves, John Wiley & Sons Ltd., **1988**
44. D.W. Breck, Zeolite Molecular Sieves, Structure, Chemistry and Use, John Wiley & Sons, Inc. , New York ; reprinted by Krieger, Malabar, Florida, **1984**

45. H. van Bekkum, P.A. Jacobs, E.M. Flanigen, J.C. Jansen, Introduction to Zeolite Science and Practice, Elsevier, Amsterdam, **1991**
46. D.E.W.Vaughan, Chem. Eng. Prog. **1988**, 84, 25
47. C. Baerlocher, W.H. Meier, D.H. Olson, Atlas of Zeolite Framework Types, 6th Edition; Elsevier: Amsterdam, **2007**
48. S.M. Auerbach, K. A. Carrado, P.K. Dutta, Handbook of zeolite science and technology, CRC press, **2003.**
49. Corma, A. Chem. Rev. **1995**, 95, 559
50. M.A. Coutant, T. Le, N. Castagnola, P.K. Dutta, J. Phys. Chem. B, **2000**, 104, 10783
51. G. Sewell, R.J. Forster, T.E. Keyes, J. Phys. Chem. A, **2008**, 112, 880
52. R. A. Rakoczy and Y. Traa, J. Microporous and Mesoporous Mater. **2003**, 60, 69
53. A. Huang and W. Yang, J. Mater. Lett. **2007**, 61, 5129
54. T. Joseph, D.P. Sawant, E.S. Gopinatb, and S.B. Halligudi, J. Mol.Cata1. **2002**, 184, 289
55. S.Hashemian, S.H. Hosseini, H. Salehifar, K.h Salari, Am. J. Anal.Chem. **2013**, 4, 123
56. K. Hedden, J. Weitkamp, Chem. Ing.Tech. **1983,** 55, 907
57. J.H. Lungford, Catal. Rev. Sci.Eng. **1975**, 12, 137
58. R.M.Barrer, Pure Appl. Chem. **1979,** 51, 1091
59. H.Su, H.S. kim, S.M.Seo, S.O.Ko, J. M. Suh, G.H. Kim, W.T. Lim, Bull Korean Chem.Soc. **2012**, 33, 2785
60. N. Herron, J. Inorg. Chem. **1986**, 25, 4714

61. R. Aravindhan, N. N. Fathima, J. R. Rao, B. U.Nair. J. Hazar. Mater. **2006**, 138, 152

62. N. N. Fathima, R.Aravindhan, J. R. Rao, B. U.Nair, Chemosphere. **2008**, 70, 1146

63. J.R. Balkus, I.P. Ferraris, J.Phys.Chem. **1990**, 94, 8019

64. J.P. Ferraris, Jr. K.J. Balkus Jr, A. Schade, J.Incl.Phenom. **1992**, 14, 163

65. E. Polat, M. Karaca, H.Demir,A. N. Onus: J. F. Ornam, Plant Res. Special ed. **2004**, 12, 183

66. K. J. Balkus, S. Kowalak, K. T. Ly, D. C. Hargis, Stud.Surf Sci. Catal. **1991**, 69, 93

67. K. J. Balkus, S. Kowalak, Collect. Czech. Chem. Comm. **1992**, 57, 774

68. V. Yu. Zakharov, O. M. Zakharova, B. V. Romanovsky, R. E. Mardaleishvili, React Kinet Catal Lett. **1977**, 6, 133.

69. Y.W. Chan, R.B. Wislon, ACS Div Fuel Chem. **1988**, 33,453

70. W.H. Laze, J.W.Kang, D.H. Chapin, Sci. & Eng. **1987**, 9, 335

71. J.M.Peralta-Hernandez, C.A.Martinez-Huitle, J. L. Guzman-Mar., J. Environ. Eng. Manage. **2009,** 19, 257

72. P.R.Gogate, A.B.Pandit, Adv. Enviro. Res. **2004**, 8, 501

73. J.J. Pignatello, Environ. Sci. Technol. **1992**, 26, 944

74. Z.Li, G. Jianghai, L. Yangxiao, L. Xiaoying, G. Guitaian, Chinese J. of Chem. Eng. **1999**,7, 110

75. O. Legrini, E. Oliveros, A. M. Braun, Chem. Rev. **1993**, 93, 671

76. J.H. Carey, Water Pollution Res, J. Canadian, **1992**, 27, 1

77. H. Zhou and D.W.Smith, J. Enviro. Eng. Sci. **2002**, 1, 247

78. N. Azbar, K. Kestiolu, T.Yonar, New Research Nova Science Publishers, New York, **2005**, pp. 99-118

79. M. El Haddad, A. Regti, M.R.Laamari, R. Mamouni, N. Saffaj, J. Mater. Environ. Sci. **2014**, 5, 667

80. S. W. Kim, R. Khan, K. Tae-Jeong, K. Wha-Jung, Bull. Korean Chem. Soc. **2008**, 29, 6

81. H.D.Mansilla, M.C.Yeber, J. Freer, J. Rodríguez, J. Baeza, J. Wat. Sci. Technol. **1997**, 35, 273

82. J.H. Baxendale, J.A. Wilson, Trans. Farad. Soc. **1957**, 53, 344

83. H.Zhu, R. Jiang, Y. Fu, Y. Guan, J. Yao, L. Xiao, G. Zeng, Desalination, **2012**, 286, 41

84. Rein Munter., Proc. Estonian Acad. Sci. Chem. **2001**, 50, 59

85. M. Leelakriangsak , S. Borisu., J. Sci. Technol. **2012**, 34, 509

86. M.E.Berezuk, A. Paesano Jr, N.M. Carvalho, A.Horn Jr, P.A Arroyo, Cardozo-Filho, L.Quim. Nova. **2012**, 35, 876

87. M. Dams, L. Drijkoningen, B. Pauwels, G. Van Tendeloo, D.E. De Vos, P.A. Jacobs: J. Catal. **2002**, 209, 225

88. D.S. Tong, C.H. Zhou, Y. Lu, H. Yu, G.F. Zhang, W.H. Yu, Appl. Clay Sci. **2010**, 50, 427

89. B.H. Hameed, J.M. Salman, A.L. Ahmad, J. Haza.Mater. **2009**, 163, 121

90. H. Faghihian and R. S. Bowman, Water Research, **2005**, 39, 1099

91. U.F. Alkaram, A.A. Mukhlis, A.H. Al-Dujaili, J. Haza.Mater. **2009**, 169, 324

92. J. Xie, W. Meng, D. Wu, Z. Zhang, H. Kong., J. Haza.Mater. **2012**, 231, 57

93. C. Covarrubias, R. García, J. Yánez, R. Arriagada., J. Porous Mater. **2008**,15, 491
94. Z.Li, T.Burt, R.S. Bowman, Environ. Sci. Technol. **2000**, 34, 3756
95. Z. Li, R. S. Bowman, Environ. Sci. Technol. **1998**, 32, 2278
96. Z. Li, K. Jones, P. Zhang and R. Bowman, Chemosphere, **2007,** 68, 1861
97. V.A. Nikashina and B.F. Myaosedov, Environmental applications of modified natural zeolites, P. Misaelides, ed., Natural Microporous Materials in Environmental Technology, Kluwer Academic Publisher, Netherlands, **1999**, pp. 335–343.
98. E.J.Sullivan, J.W.Carey, R.S. Bowman, J.Coll. Inter. Sci. **1998**, 206, 369
99. G.M.Haggerty, R.S.Bowman, Enviro. Sci. Techno. 1**994,** 28, 452
100. Y. Xi, H.H. Ding, R.L. Frost, Spectrochimica Acta Part A: Molecular Biomolecular Spectroscopy, **2005**, 61, 515
101. Y.Xi, R.L. Frost, H.He, T. Klopogge, T.Bostrom, Langmuir, **2005**, 21, 8675
102. J. Lemić, D. Kovačević, M. Tomašević-Čanović, D. Kovačević,T. Stanić, R. Pfend, Water Research, **2006,** 40, 1079
103. A. Kuleyin, J.Hazar.Mater. **2007**, 144, 307
104. S. Xu, S.A. Boyd, Enviro. Sci. Techno. **1995** ,29, 3022
105. S. Xu, S.A. Boyd, Langmuir, **1995,** 11, 2508
106. Z.Li, H. K. Jones, R.S. Bowma, R.Helferich, Environ. Sci. Technol. **1999**, 33, 4326
107. G.M. Haggerty, R.S. Bowman, Environ. Sci. Technol. **1994**, 28, 452
108. Z. Li, R.S. Bowman, Environ. Sci. Technol. **1997,** 31, 2407
109. R.T. Silvio and R. Jorge, Miner. Eng. **2010**, 23, 771

110. R. Ganesan, B. Viswanathan, J. Mol. Catal. A: Chem. **2004**, 223, 21

111. K.K. Bania, D. Bharali, B. Viswanathan, R.C. Deka, J. Inorg. Chem. **2012**, 51, 1657

112. T. P. Amaladhas, S. S.Thavamani, Adv. Mat. Lett. **2013**, 4, 213

113. T. P. Amaladhas, S.S. Thavamani, Adv. Mat. Lett. **2013**, 4, 688

114. S. K. Masoudian, S.Sadighi, A. Abbasi, J. Chem. Reac. Eng. & Catal. **2013**, 8, 54

115. J.I. Gersten, F.W. Smith, The physics and chemistry of materials, Wiley, New York, **2001,** pp. 412-415

116. J.Garcia-Martinez, D.Cazorla-Amoros, A.Linares-Solano, Appl. Catal. B: Enviro. **2004**, 47, 203

117. N.A. Seaton, J.P.R.B. Walton, N. Quirke, Carbon, **1989,** 27, 853

118. A. Gil, S.A. Korili, G.Y. Cherkashinin, J. Colloid Interface Sci. **2003**, 262, 603

119. G. Horvath, K. Kawazoe, J. Chem. Eng. Jpn. **1983**, 16, 470

120. L.S. Cheng, R.T. Yang, Chem. Eng. Sci. **1994,** 49, 2599

121. U.S. Rege, R.T. Yang, AIChE J. **2000**, 46, 734

122. A. Saito, H.C. Foley, AIChE J. **1993**, 7, 429

123. T.H.Bennur, D.Srinivas, P. Ratnasamy, Microporous and Mesoporous metar. **2001,** 48, 111

124. B. F.G. Johnson, J. S. McIndoe, Coord. Chem.Reviews, **2000,** 200, 901

125. M.C.R. Symons, Chemical and Biochemical Aspects of Electron-Spin Resonance, Wiley & Sons, New York, **1978**

126. S.Blanchard, F.Neese, E. Bothe, E. Bill, T. Weyhermüller, K. Wieghardt, Inorg. Chem. **2005**, 44, 3636

127. A.Bencini, D.Gatteschi, E.I. Solomon, A.B.P. Lever (Eds.), Inorganic Electronic Structure and Spectroscopy, Wiley, New York, **1999**

128. S. Hashemian,S. Hosseini, H. Salehifar, K. Salari, Am. J. Anal.Chem. **2013**, 4,123

129. M. Thompson, Analytical Methods Committee, Royal Soc. of Chem. **2008,** AMCTB No 29

130. V.P.Fadeeva, V.D. Tikhova, O. N. Nikulicheva, J. Anal. Chem. **2008,** 63, 1094

131. S. Syafalni, S. R. B. Sing, M. H. Zawawi, J.World Appl. Sci. **2014,** 32, 818

132. I. Sondi, J. collol. and inter. Sci. **1996,** 178, 514

133. A. Choudhary, B. Das, S. Ray. J Chem Soc Dalton Trans, **2015**, 44, 3753

134. M. Silva, C. Freire, B. de Castro, J.L. Figueiredo. J Mol Catal A: Chem. **2006**, 258, 327

135. D.W.Ming, J.B. Dixon, Caly clay miner. **1987**, 35, 463

136. L.D.Sánchez, S.F.M.Taxt-Lamolle, E.O.Hole, A. Krivokapic, E. Sagstuen, H.J. Haugen, Appl. Catal. B: Environ. **2013**, 142, 662

137. R. G. Parr, L. V. Szentpaly, S. Liu, J. Am. Chem. Soc.**1999**, 121, 1922

138. J.Bassett, R.C.Denney, G.H.Jeffery, J.Menhdham, Vogel's textbook of quantitative chemical analysis, Longman Scientific and Technical, London, 5th edn., **1989**, pp. 372-373

139. M.Salavati-Niasari, Z. Salimi, M. Bazarganipour, F. Davar, Inorg. Chim. Acta. **2009,** 362, 3715

140. K. Xavier, J. Chacko, Y.K.Mohammed, Appl. Catal. A: General. **2004**, 258, 251

141. M.J. Alcón, A.Corma, M. Iglesias, F.Sánchez, J. Molec. Catal. A: Chemical, **2003**, 194, 137
142. M.R.Maurya, A.K.Chandrakar, S.J.Chand, Mol. Catal. A: Chem. **2007**, 270, 225
143. M.R.Maurya, S.J.J. Titinchi, S.Chand, I.M.Mishra, J. Mol. Catal. A: Chem. **2002**, 180, 201
144. K.Mukhopadhyay, A.B.Mandale, R.V. Chaudhari, Chem. Mater. **2003,** 15, 1766
145. Y.Umemura,Y. Minai, T. Tominaga, J. Phys. Chem. B. **1999**, 103, 647
146. Bennur T.H, Srinivas D, Ratnasamy P, Micropor. Mesopor. Mater. **2001,** 48, 111
147. K.K.Bania, D. Bharali, B.Viswanathan, R.C. Deka, Inorg. Chem. **2012**, 51, 1657
148. K.K.Bania, G.V.Karunakar, K.Goutham, R.C.Deka, Inorg. Chem. **2013**, 52, 8017
149. C.Hadjur, G.Wagnières, F.Ihringer, P.Monnier, H. van den Bergh, J. Photochem. Photobiol. B: Biol. **1997**, 38, 196
150. H.Kušić, N.Koprivanac, I.Selanec, Chemosphere. **2006,** 65, 65
151. Z.Yaping, H. Jiangyong, Appl. Catal. B: Environ. **2008**, 78, 250
152. A.Babuponnusami, K.Muthukumar, J. Environ. Chem. Engg. **2014**, 2, 557
153. H.Kusic, A.Loncaric Bozic, N.Koprivanac, S.Papic, Dyes and Pigments, **2007,** 74, 388
154. M.Aleksic, N.Koprivanac, H.Kusic, D. Leszczynska, A.Loncaric Bozic, Desalination, **2010,** 257, 22
155. M.Neamtu, C.Zaharia, C. Catrinescu, A.Yediler, M.Macoveanu, A.Ket-Trup, Appl. Catal. B: Environ. **2004**, 48, 287
156. A.Chen, X.Ma, H.Sun, J. Hazard. Mater. **2008**, 156, 568

157. M.A. Coutant, T. le, N. Castagnola and P. K. Dutta, J. Phys. Chem. B, **2000**, 104, 10783

158. K.K.Bania and R.C.Deka, J. Phys. Chem. **2012**, 116, 14295

159. K.K.Bania, D.Bharali, B.Viswanathan and R. C. Deka, J. Inorg. Chem. **2012**, 51, 1657

160. K.S.W.Sing,D.H.Everest,R.A.W.Haul,L.Moscou,R.A.Pierotti,J.Rouquerol,T. Siemieniewska, Pure Appl. Chem. **1985**, 57, 603

161. S.Brunauer,L.S.Deming, W E. Deming and E. Teller, J. Am. Chem. Soc. **1940**, 62, 1940

162. M.R.Maurya, S.J.J.Titinchi, S.Chand, I. M. Mishra, J. Mol. Catal. A: Chem. **2002**, 180, 201

163. R. Ganesan and B.Viswanathan, J. Phys. Chem. B, **2004**, 108, 7102

164. T. M. Salama, A.H.Ahmed, Z. M. El-Bahy, Microporous Mesoporous Mater. **2006**, 89, 251

165. M.Salavati-Niasari, Z.Salimi, M.Bazarganipour, F.Davar, Inorg. Chim. Acta. **2009**, 362, 3715

166. K. K. Bania, G. V. Karunakar, K. Goutham, R. C. Deka, J. Inorg. Chem. **2013**, 52, 8017

167. K. Xavier, J. Chacko , K. M. Yusuff, Appl. Catal. A, **2004**, 258, 251

168. S.Wannakao, P.Khongpracha, J. Limtrakul, J. Phys. Chem. A, **2011**, 115, 12486

169. M.R.Maurya, S.J.J.Titinchi, S.Chand, J. Mol. Catal. A: Chem. **2003**, 201, 119

170. W.H.Quayle, J.H. Lunsford. Inorg Chem. **1982**, 21: 97

171. X.Hu, K.Meyer. Inorg Chim Acta, **2002**, 337: 53

172. S.Brunauer, L.S.Deming, E.Teller, J. Am.Chem. Soc. **1940**, 62, 1723

173. K.O. Xavier, J. Chacko, K.K. M. Yusuff, Appl Catal A: General, **2004**, 258, 251

174. Y.Yang, H.Ding, S.Hao, Y. Zhang, Q. Kan, Appl Organometal Chem. **2011**, 25, 262

175. K. M.Chetan, M.T. Parthiv, Adv. Mat. Lett. **2012**, 3, 149

176. B. Dutta, S. Jana, R. Bera, P.K. Saha, S. Koner, Appl. Catal. A:General, **2007**, 318, 89

177. G. R. Reddy, S. Balasubramanian, K. Chennakesavulu, J .Mater. Chem. A, **2014**, 2, 15598

178. K.K. Bania, G.V. Karunakar, K. Goutham, R.C. Deka, Inorg .Chem. **2013**, 52, 8017

179. A. Babuponnusami, K. Muthukumar, J. Enviro.Chem.Eng. **2014**, 2, 557

180. J. Chen, L. Zhu, Catal. Today, **2007**, 126, 463

181. O.B. Ayodele, J.K. Lim, B.H. Hameed, Appl.Catal. A: General, **2012**, 413, 301

182. L. Xu, J. Wang, J. Hazard. Mater. **2011**,186, 256

183. J. Kronholm, S. Huhtala, H. Haario, M.-L. Riekkola, Adv .in Environ. Res. **2002**, 6, 199

184. H.Y. Xu, M. Prasad, Y. Liu, J. Hazard. Mater. **2009**, 165, 1186

185. J. Guo, M. Al-Dahhan, Appl. Catal. A: General, **2006**, 299, 175

186. J.H. Ramirez, C.A. Costa, L.M. Madeira, G. Mata, M.A. Vicente, M.L. Rojas-Cervantes, A.J. López-Peinado, R.M. Martín-Aranda, Appl. Catal. B: Enviro. **2007**, 71, 44

187. J.H. Ramirez, F.M. Duarte, F.G. Martins, C.A. Costa, L.M. Madeira, J.Chem.Eng. **2009**, 148, 394

188. Y. Zhan, Z. Zhu, J. Lin, Y. Qiu, J. Zhao, J. Environ. Sci. **2010**, 22, 1327

189. R. Leyva-Ramos, A. Jacobo-Azuara, P.E. Diaz-Flores, R.M. Guerrero-Coronado, Coll. and Surfa. A: Physicochem. and Eng. **2008,** 330, 35

190. P. Chutia, S. Kato, T. Kojima, S. Satokawa, J. Hazar. Mater. **2009**, 162, 204

191. K. Mukhopadhyay, A.B. Mandale, R.V. Chaudhari, Chem. of Mater. **2003**, 15, 1766

192. M.R. Maurya, S.J.J. Titinchi, S. Chand, I.M. Mishra, J. Mol. Catal. A: Chem. **2002**, 180, 201

193. Y. Umemura, Y. Minai, T. Tominaga, J. Phy. Chem. B, **1999**, 103, 647

194. I.D. Mall, V.C. Srivastava, N.K. Agarwal, Dyes and Pigments, **2006**, 69, 210

195. S.Panumati, K.Chudecha, P.Vankhaew, V.Choolert, L.Chuenchom,W.Innajitara, O.Sirichote, J. Sci. Technol. **2008**, 30, 185

196. B.V. Babu, S. Gupta, Adsorption, **2008**, 14, 85

197. H.B.Senturk, D.Ozdes, A. Gundogdu, C. Duran, M. Soylak, J. Hazar. Mater. **2009**, 172, 353

198. Y. Zhan, J. Lin, Z. Zhu, J. Hazar. Mater. **2011**, 186, 1972

199. R.Leyva-Ramos, A.Jacobo-Azuara, O.L.Torres-Rivera, R.M.Guerrero Coronado, M.S. Berber-Mendoza, P.Alonso-Davila, J. Environ. Eng. Manage. **2008**, 18, 311

200. D. Mohan, J.U. Pittman, J. Hazard. Mater. **2006**, 137, 762

201. K. Selvi, S. Pattabhi, K. Kadirvelu, Bioresource Techno. **2001**, 80, 87

202. B.S. Krishna, D.S.R. Murty, B.S.J. Prakash, Appl. Clay Sci. **2001**, 20, 65

203. A.Mittal, J. Hazard. Mater. **2006**, 133, 196

204. K.R. Hall, L.C. Eagleton, A. Acrivers, T. Vermenlem, Ind. Eng. Chem. Res. **1966**, 5, 212

205. D. Karadag, Y. Koc, M. Turan, B. Armagan, J. Hazard. Mater. B, **2006**, 136, 604

206. K. Saltalı, A. Sari, M. Aydin, J. Hazard. Mater. **2007**, 141, 258

207. H. Zheng, Y. Wang, Y. Zheng, H.i Zhang, S. Liang, M. Long, J. Chem. Eng. **2008**, 143, 117

7. Appendices

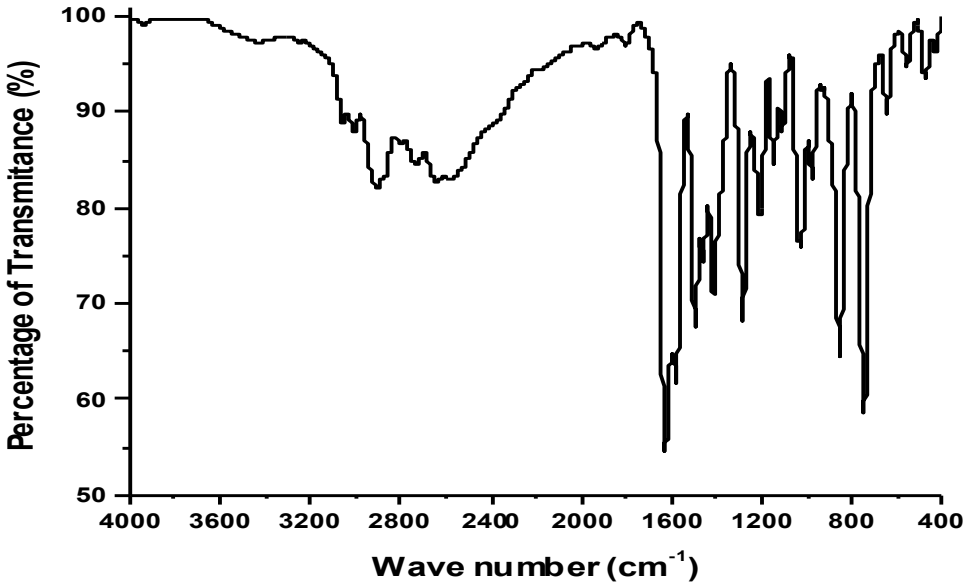

Figure 7.1 FT-IR spectra of N,N′-Ethylenebis(salicylimine) or salen ligand

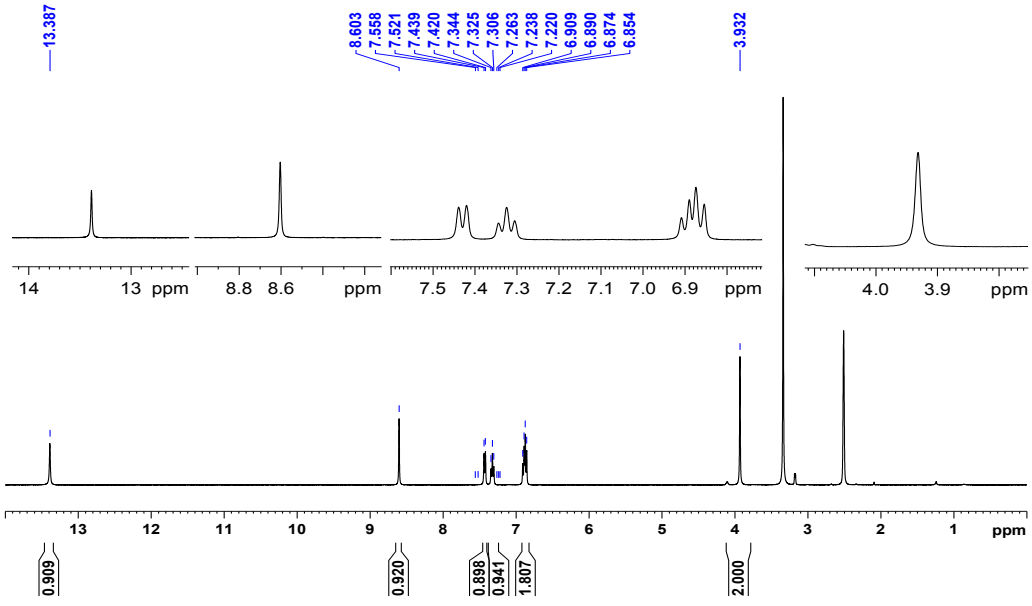

Figure 7.2 ^{1}H NMR spectra of N,N′-Ethylenebis(salicylimine) or salen ligand

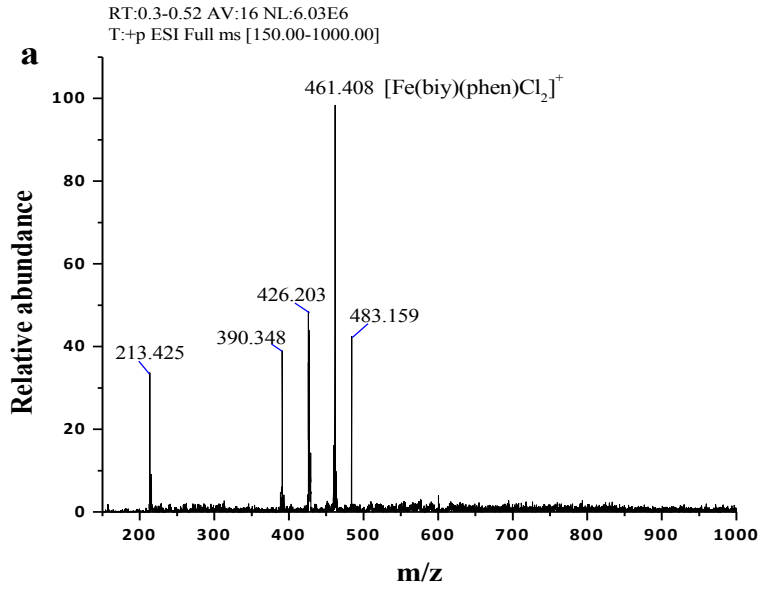

Figure 7.3 ESI-MS for $[Fe(bipy)(phen)Cl_2]^+$

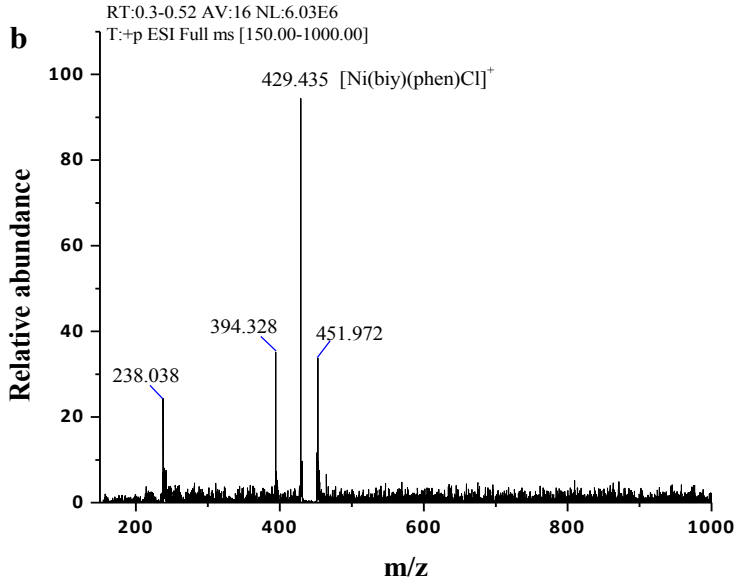

Figure 7.4 ESI-MS for $[Ni(bipy)(phen)Cl]^+$ complex

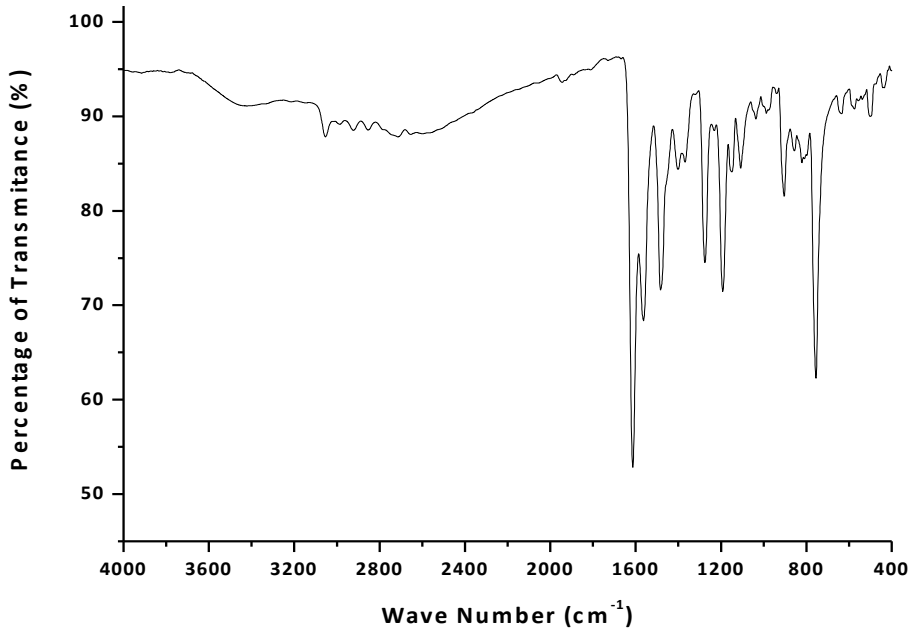

Figure 7.5 FT-IR spectra of N,N′-disalicylidene-1,2-phenylenediamine or Salophen ligand

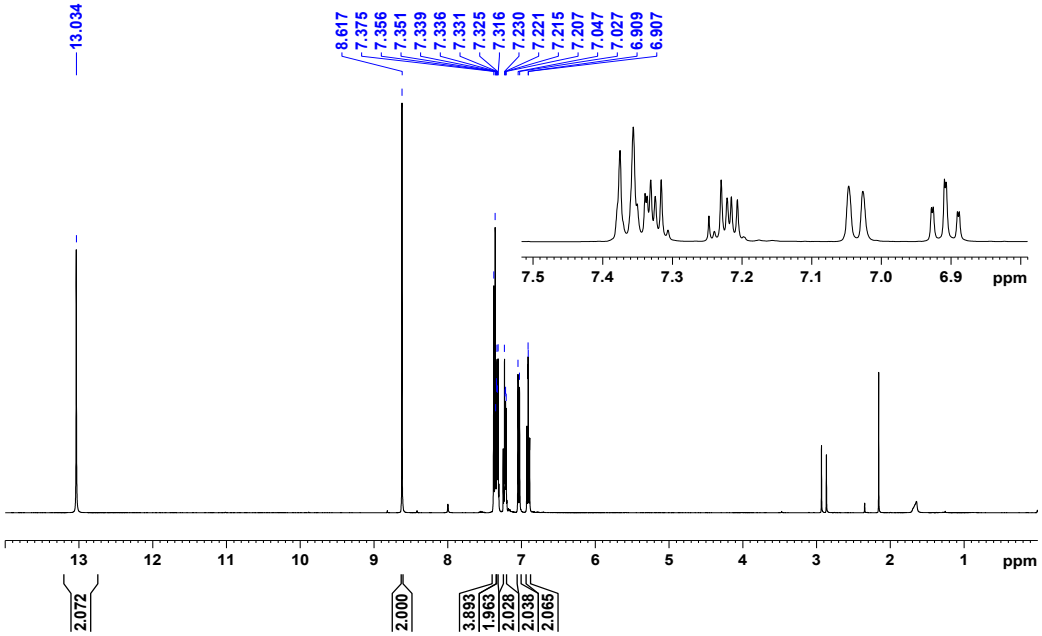

Figure 7.6 ^{1}H NMR spectra of N,N′-disalicylidene-1,2-phenylenediamine or Salophen ligand

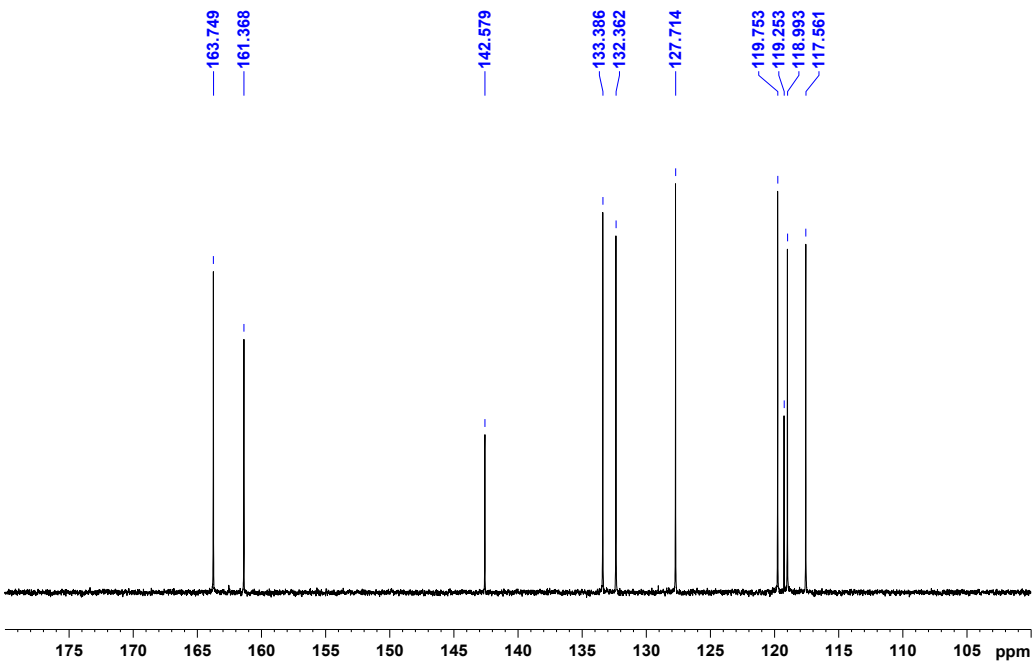

Figure 7.7 ^{13}C NMR spectra of N,N′-disalicylidene-1,2-phenylenediamine or Salophen ligand

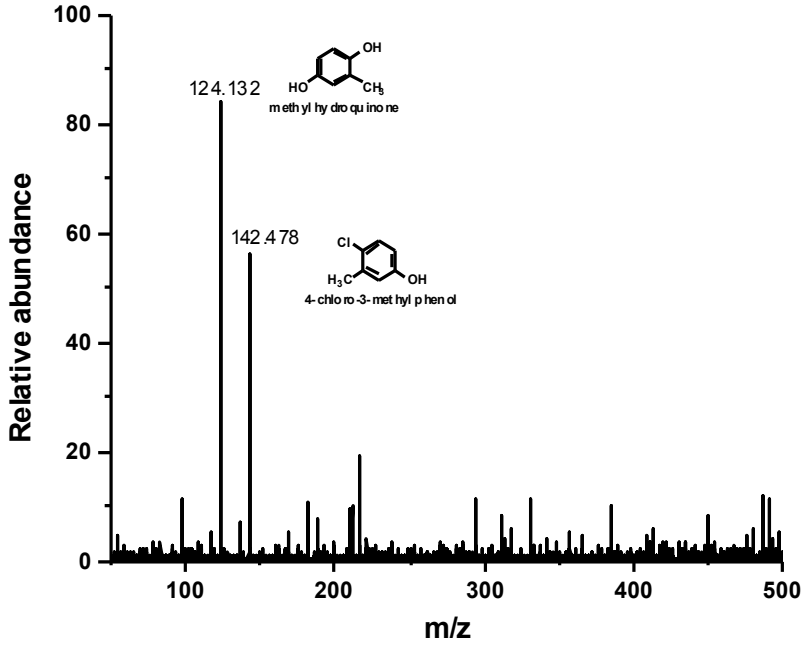

Figure 7.8 ESI-MS for intermidate product of oxidation of 4-chloro-3-methyl phenol after 30 min

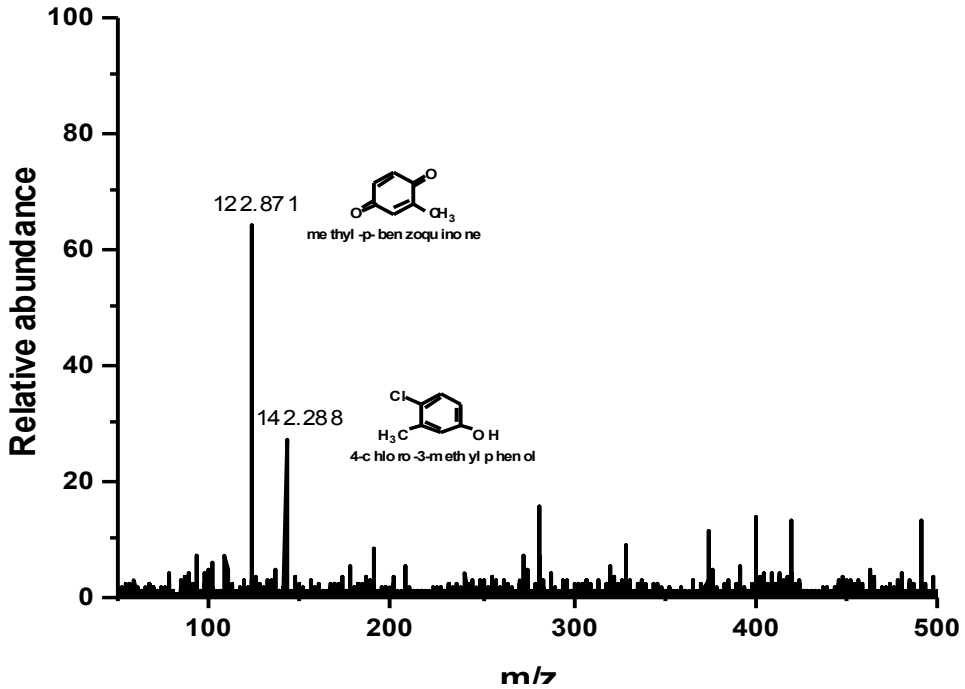

Figure 7.9 ESI-MS for intermidate product of oxidation of 4-chloro-3-methyl phenol after 60 min

Publications

1. **Solomon L. Hailu**, B. Nair, M. Redi-Abshiro, R. Aravindhan, I. Diaz, M. Tessema, Synthesis, characterization and catalytic application of zeolite based heterogeneous catalyst of iron(III), nickel(II) and copper(II) salen complexes for oxidation of organic pollutants, **Journal of Porous Materials**, 2015, 22 : 1363-1373

2. **Solomon L. Hailu**, B.U. Nair, M. Redi-Abshiro, R. Aravindhan, I. Diaz, M. Tessema, Experimental and computational studies on zeolite-Y encapsulated iron(III) and nickel(II) complexes containing mixed-ligands of 2,2′-bipyridine and 1,10-phenanthroline, **RSC Advances**, 2015, 5 : 88636-88645

3. **Solomon L. Hailu**, B.U. Nair, M. Redi-Abshiro, R. Aravindhan, I. Diaz, M. Tessema, Oxidation of 4-chloro-3-methyl-phenol (PCMC) through zeolite Y encapsulated Catalyst of Iron(III), Nickel(II) and Copper(II) N,N′-disalicylidene-1,2-phenylenediamine Complex, **Chinese Journal of Catalysis**, 2016, 37 : 135-145

4. **Solomon L. Hailu**, B.U. Nair, M. Redi-Abshiro, I. Diaz, M. Tessema, Adsorption of acid blue dye and chromium(VI) onto cationic surfactant modified zeolite, **(under riview)**